Adapting Cartesian cut cell methods for flood risk evaluation

Andrew Gordon Morris

August 2012

revised December 2013

A thesis submitted in partial fulfilment of the requirements for the degree of Doctor of Philosophy

Centre for Mathematical Modelling and Flow Analysis
School of Computing, Mathematics and Digital Technology
Manchester Metropolitan University

Contents

List of Figures

List of Tables

Declaration

No portion of the work referred to in this thesis has been submitted in support of an application for any other degree or qualification at this or any other institute of learning.

Apart from those parts of this thesis which contain citations to the work of the others and apart from the assistance mentioned in the acknowledgements, this thesis is my own work.

Andrew Gordon Morris

Abstract

Assessing the risks of flooding, and the effectiveness of mitigation strategies, is an important part of any river management strategy. This is improved greatly by the accurate simulation of surface hydraulics, and moving to two-dimensional simulations that can capture the dynamics of surface processes has clear advantages. Only with the increased availability of accurate topographic data, has this become practical for many cases.

In chapter two the methodologies of river flood modeling are described. A number of concerns peculiar to that field are discussed. These include roughness parameterisation and heterogeneity of features on the domain.

Finite Volume (FV) methods can simulate shallow water flows efficiently. Their shock-capturing ability makes them especially useful for flash-flood events. A particular FV package AMAZON-CC is adapted, which uses an approximate two-shock Riemann solver over a regular orthogonal grid. The Cartesian cut-cell method allows solid regions to be included as local modifications to individual cells.

Wetting and drying causes particular difficulties with FV methods. The Volume to Free-Surface Relationship (VFSR) method provides a framework in which a variety of mitigation strategies can be adopted. A modified form of this was used, adapted to the rectangular grid with a piecewise level interpretation of topography. Several strategies are tested, and the most successful adopted thereafter.

The Cartesian cut-cell method was extended to include large scale but complex

features as vector, or polygon data-sets. The approach here concentrates on the fluxes across boundaries, to represent linear features such as hedgerows and fences. Preliminary results are presented and analysed and compared to classical results for headloss from interaction with structures.

Test cases based on physical expreriments and real-life events are successfully reproduced. These demonstrate the suitability of AMAZON as a tool to model inland flooding.

Acknowledgements

I would like to thank my original supervisor Professor David Ingram, now at Edinburgh University. Thank you also Professor Clive Mingham of Manchester Metropolitan University who took over when he left, and has been very helpful and supportive whenever I gave him the opportunity. I also owe a mention to Professor Derek Causon, and Dr Jon Shiach, who have been very helpful at various times.

My parents deserve a special mention for keeping me housed and fed, and generally putting up with me for the last difficult phase of writing up.

I would also like to thank my colleagues at MMU who have done more than they know to help keep me sane, and the technical staff who's work so often seems to go unacknowledged.

This research was funded by the Environmental and Physical Science Research Council. It was carried out using software developed at the Centre for Mathematical Modelling and Flow Analysis.

Nomenclature

x, y	coordinates in each direction
$\mathbf{n}$	vector normal to the face of a cell
l_F	the length of a face F
h	depth of water
z_s	level of water above datum
z_b	level of bed above datum
u, v	velocity component in each direction
$\mathbf{v}$	velocity vector
g	acceleration due to gravity ($\approx 9.81 ms^{-2}$)
e_i	a (right) eigenvector associated with the eigenvalue λ_i
r	Sweby's dimensionless parameter for the ratio of two gradients
e	total pressure head as used in the Bernoulli equation
$\vec{os}$	vector from cell centre to a reference point

$\mathbf{U}$	vector of conserved variables
$\mathbf{F}, \mathbf{G}$	flux vector in each direction
$\mathbf{S}$	source terms including ..
$\mathbf{S_f}$	friction component
$\mathbf{S_b}$	bed slope component
C_f	friction coefficient
C	bounded region (of a cell)
E	boundary of a region (or cell)
$\mathcal{F}$	face of a cell
$\mathcal{N}, \mathcal{S}, ..$	the four faces of a rectangular cell ..
.. $\mathcal{E}, \mathcal{W}$	.. identified by compass direction
J	Jacobian matrix
F_r	Froude number
R	transformed parameter, used for averaging
$\mathcal{L}, \mathcal{R}$	denote the left and right side of a discontinuity in a Riemann problem
$S_\mathcal{L}, S_\mathcal{R}$	the leftmost and rightmost wavespeeds in the solution to a Riemann problem
$\|V\|$	measure of variance used in TVD schemes
$\mathcal{G}$	gradient
C_a	Cauchy parameter

Greek symbols

Δ	difference operator
ζ	water surface elevation above the bottom datum (m)
τ	arbitrary time from start of Riemann problem
η	level of water above datum
λ_i	i'th eigenvalue of the Jacobian
ε	error term for goodness of fit for gradients
φ	weighting of a gradient used to find error function ε
ν	slope limiter function
ρ	density
Φ	energy potential due to elevation above the bed gh
$\Delta x, \Delta y$	the dimensions of a cell in each direction
Δt	time-step
ψ	porosity of boundary
∂	the partial differential

Chapter 1

Introduction

Flood modelling serves these purposes; to predict an imminent threat, to identify the potential threats to life and property, and to evaluate the effectiveness of remedial measures. Flood warning is dependent on weather forecasting and on whole catchment hydrology. Flood risk evaluation, on the other hand, requires a much more detailed localised assessment. Once a river has breached its banks the flow becomes much more varied and dynamic.

To predict this a new range of modelling tools are being adopted. The value of two dimensional planar models over one dimensional channel models is obvious. The value of fully dynamic simulation is attested to by the change in sensitivity to parameters once momentum is included.

The adoption of these techniques has been delayed for a number of reasons. The added complexity of the models required more computer power than had been available in the past. The calibration of distributed models is a significant problem. This is particularly so for flooding. Flood events are rare and observation could be hazardous. Peak water levels were often surmised from the damage and debris left behind in the absence of gauge readings.

The expansion of remote sensing technology (Fowler, 2000; Bates *et al.*, 1997; Bates, 2012) has had a great impact on this field. It allows the flood extent to

be seen as it changes with time. Even more significantly it allows topography and land use to be mapped in detail. This has made detailed 2D flood modelling practical. There has been a particular interest in using such models to evaluate flood risk in towns and cities.

AMAZON-CC uses a finite volume (FV) discretisation. Finite volume methods conserve mass and momentum, and they can handle discontinuities. Other approaches include finite difference (FD) an finite element (FE) methods.

There are already numerical modelling packages which have been developed for this purpose(Neelz and Pender, 2009). Paquier *et al.* (2001) describes Rubar 20 an early application of FV to river flooding, developed at a time when the computational resources made this harder to justify. Villanueva (2006) develops Trent which applies a 1D FV to channel flow, and either diffusive storage models or 2D FV models to the floodplain, according to need and computational cost. Similarly Horritt (2004) makes cautious use of a FV solver on a primarily diffusive tidal-flood event, placing severe constraints on wetting and drying to avoid instabilities. FV solvers which tackle the complexities of flood flow without hybridisation include BreZo (Begnudelli and Sanders, 2006) and Guinot (Guinot and Soares-Frazao, 2006) among others. Commercial packages using FV include; Hydro2de(Beffa and Connell, 2001; Connell *et al.*, 2001) , Infoworks2D, Telemac2D and TUFLOW-FV. Telemac2D also implements FE methods(Cobby *et al.*, 2003).

1.1 Practicalities of Flood Modelling

The physical modelling of surface waters presents particular challenges. (These are described in greater detail in Chapter 2.)

Parameterisation is of serious concern to hydrologist. Because flood events are rare it is not possible to verify complex models and therefore models can only rely on a small number of parameters. The roughness parameter has in the past stood

in for a number of unrelated factors (eg Werner *et al.* (2005)), and has dominated 1D and 2D implementations of the Kinetic wave equation. It has been shown to be less important when implementing the complete form of the Shallow Water Equations (eg Horritt and Bates (2002)) but is nonetheless significant.

Deciding which features should be included in a model is important. A floodable area will have features which may block or slow down flow locally, but may also divert flow to other areas downstream. Many features such as hedgerows and railway sidings are long and thin and need to be treated as such in simulation. See section 2.3.2 and (Connell *et al.*, 2001).

The numerical techniques require specific expertise to deal with problems. There are well-documented but poorly understood instabilities that can arise with wetting and drying.(Tchamen and Kawahita, 2001) This problem needs to be addressed robustly by the code if it is to be broadly usable.

There are particular features of channel flow which would be difficult to replicate if the channel is not represented at the appropriate scale. It may be necessary to use a coupled channel-floodplain model if the channel width is small relative to the grid size.

Turbulence arising in compound channels has been well studied (Knight and Shiono, 1996). This can also arise from interaction between channel and floodplain flows. If this happens the floodplain will flood more rapidly than might otherwise be expected. Turbulence on these scales has been well studied empirically, and with 3D computer simulation. At most scales, it would be computationally expensive to replicate this effect with a 2D model, compared with a coupled channel, floodplain model.

Smaller scales of model have been applied to flooding of narrow valleys from braided and meandering rivers (Lane and Richards, 2001; Yu and Lane, 2006). Here the width of the floodplain and that of the channel are sufficiently close.

1.2 Aims and Objectives

The aim of this study is to adapt AMAZON-CC, a finite volume simulation package, and to test its applicability to flood risk evaluation. In particular the routines used to include solid obstacles on the domain are a novel feature of this package. These routines are adapted to deal with a broader range of features. The extent to which this can be used to deal with some practical issues of flood modelling is explored. A solution to the wetting and drying problem is implemented and evaluated. Finally, the program is tested against some well-known physical models.

1.3 AMAZON Cartesian cut-cell

The package used was AMAZON Cartesian Cut-Cell (AMAZON-CC)(Mingham and Causon, 1998; Causon *et al.*, 1999; Ingram *et al.*, 2003). This is a numerical modelling software package, developed by CMMFA. It uses a HLL Riemann solution for intercell flux, which is very efficient. It applies a Galerkin two step solution to allow second order accuracy with time. It has a selection of slope limiter functions to allow second order accuracy in space where this does not compromise stability. These apply the surface gradient method, which assumes a level water surface. This ensures a balancing of depth and velocity for subcritical flows over an uneven bed. The cut-cell routines allow any shape of domain to be used with a rectilinear mesh. This includes the placement of solid obstacles within the domain.

1.4 Additions to AMAZON-CC

A text file parser was added, including subroutines to interpret time-variable, vector and raster data.

The choice of boundary conditions was extended to include depth and discharge to be specified at the boundary. Boundary conditions are now implemented, by

specifying ghost values at the cell boundaries instead inside hypothetical ghost-cells. This change is intended to rectify a slight response delay noticed in time variable boundary conditions.

1.4.1 Wetting and Drying

To resolve the wetting and drying problem the Volume to Free-surface Relationship (VFR) approach (Begnudelli and Sanders, 2006) was used. This assumes a level water surface for partially wetted cells. Compromises may also be made with the time step and conservation of momentum for such cells. An alternative bed geometry was tried with this method in order to simplify the calculations. It ensures a level bed at the interface between cells with no step, matching the classical Riemann problem as closely as possible.

1.4.2 Use of cut cells

The cut-cell routines interpret vector lists as lines and polygons on the domain. Cells on the grid are identified as being outside the polygon, inside the polygon or cut by a line. These cut cells are subject to specialised routines for most calculations. The original purpose of this is to represent solid regions, with a reflective external boundary.

These were adopted in the data entry phase to allow initial conditions and domain parameters to be defined on an arbitrary area.

They were also altered to represent boundaries with flow on both sides. The routines were accessed twice in order to create two sets of cut-cells for each polygon. This allows for arbitrarily thin solid walls. Semi-permeable boundary conditions are also possible.

Cut cells complicate the application of slope limiter functions. The gradients in each direction can not be treated separately as they are on an orthogonal grid.

Linear programming routines (Berger *et al.*, 2005) were written to address this.

1.5 Test Cases

1.5.1 Wetting and Drying

The wetting and drying routines are tested against a dam-breach over four irregular conical mounds. The two VFR methods are both tested with permutations of the compromises applied. Results, however bad, are presented wherever this is possible.

1.5.2 Benchmark Cases

Two sets of physical experiments and one historic event are reproduced using the code. All three involve solid obstacles, demonstrating the effectiveness of the cut-cell routines over a range of scales and complexity.

In the first a simulated dam breach is sent past a rectangular block which is placed at an angle to the direction of flow. In the second flash flows over a scale model of the Toce river valley pass a group of square blocks. In the historic case a small urban catchment in Glasgow is flooded.

1.5.3 Permeable Boundaries

A steady channel flow simulation is used to test the semi-permeable boundary routines. This is compared against the head loss expected from a sudden expansion in cross sectional area.

Chapter 2

Motivation

2.1 Current Practice in Flood Risk Evaluation

River flooding is an issue of growing concern in Britain and throughout the world (Pitt, 2008). While with proper management the risks to life can be minimized, property damage and the distress and disruption to the lives of those affected is great. To put in place the appropriate defences a thorough assessment of risks and impacts is necessary. The choice of methodology has always been limited by technology of the time. Recent advances in both remote sensing technology, and in computational power should be exploited to their fullest. At the same time, it must be acknowledged that many of the practical limits to evaluation of past events, and prediction of future events still apply.

2.1.1 Hydrological Modelling

A flooding event involves the interaction of several different systems, operating over differing time scales and observable to differing degrees. In some cases flash floods are caused by intense local rainfall. In others they only occur after a long period of rainfall has saturated the surface soil of a catchment area. Much of the flood warning method relies on a sparse dataset, combining local rainfall gauge

readings and river levels. Unobserved variables, such as ground water or soil saturation, must be surmised from these.

Linear time-series hydrological models which predict observed (gauged) and hidden (ungauged and groundwater) storage variables, can involve a great number of parameters. This makes them difficult to calibrate, particularly for extreme events. Within the United Kingdom the empirical data collected to support these methods has been substantial, notably consolidated in the reference work the Flood Estimators Handbook (reviewed by Kundzewicz and Dobrzynski (2000)). While physically based conceptual models have informed this methodology, the significance of this large hidden component means that an empirical approach remains appropriate at the catchment scale.

2.1.2 Flood Defence and Flood Risk Management

An examination of flood mitigation strategy is presented by Pennington and Tunstall (1996).

Developments on and off the floodplain can both have an adverse impact on flood risk. Developments on floodplains not only require protection, but can reduce the floodplain storage capacity by landfill. Insensitive developments off the floodplain also reduce the local storage of rainfalls increasing the speed and intensity with which floodwater reaches vulnerable areas downstream. Avoiding developments which exacerbate the risks of flooding is of primary importance in any flood alleviation.

" In these respects society and governments are generally attempting to tackle the residue from the mistakes of the past, by designing flood alleviation schemes to protect the considerable amount of unwise development that has already occurred on floodplains. " [*Ibid.* page 496.]

Flood risk management requires a balancing of the costs incurred and the

costs avoided of any mitigation strategy. Costs include the loss of assets which the floodplains and rivers provide. In the United Kingdom, for example, these include the wetlands which are much valued habitat for wildlife.

The risks incurred by flooding are the product of the harm to person and property, and the likelihood of that harm occurring. Conurbations are at greater risk due to the concentration of people and property. Social factors, such as community cohesion and the number of elderly, are important indicators of vulnerability. The depth and speed are the most significant flow characteristics for predicting damage to property. These are better represented with a dynamic 2D model.

The most extreme events can be too unlikely to justify the expense of prevention. In this case flood warning and relief strategies are needed. Rescuers will need to anticipate accessibility. The effects of flooding on transport networks and on electricity supply are important to recovery after the event. Detailed models can also serve to inform emergency planning.

2.2 Relevance of 2D Hydraulic Models

Two major technological advances have led to renewed interest in two dimensional shallow water models (hereon 2D-SWM). First has been the steady, but still rapid, development of computational power and its exploitation. Second was the release of former military digital mapping technology. (See section 2.2.2 below.)

In the UK the shift in policy from flood defence to flood risk management has made detailed urban flood models much more relevant. These are best addressed with high resolution two dimensional models.

2.2.1 Computer Technology

The impact of Moore's law on numerical simulation is easily understood and direct. The level of detail achievable (taken as the number of grid points times the number

of time steps) is proportional to rate at which the data can be processed. This has inspired the development of numerical methods, to exploit this processing power. Much of the theory behind these methods is well established, but practical experience has thrown up unexpected problems, and ingenious solutions. The reliability and accuracy of these methods has improved significantly.

2.2.2 Mapping Technology

Remote sensor data is collected from a plane or a satellite. SAR (Synthetic Aperture Radar) has been mounted on satellites. LiDAR (Light Detection and Ranging) uses a reflected light pulse to determine the altitude of a point, collected from air. SLR uses LASER radar from space.

SAR (Townsend and Walsh, 1998) and (Bates *et al.*, 1997) has been used to record the extent of flooding. This may be determined from the surface reflectivity or by noting double responses from the land and water. It is of particular use in regions which are obscured by vegetation.

LiDAR is used in aerial surveys to map topography and land use. When such data started to be made available for civilian use, the resolution and accuracy was limited. Fowler (2000) used an analysis of composite sources of error to derive a confidence band for height measurements of ± 15 cm. Empirical studies by Hodgeson (2004) found RMS errors of $17 - 19$ cm in the best cases.

A recent review (Bates, 2012) has highlighted the progress since then. In the intervening decade the quality and quantity of LiDAR data has been greatly enhanced. A RMS error of $\pm 5cm$ is more typical. Also LiDAR coverage has extended to cover roughly 70% of the UK. The technology has been developed to gather LiDAR data from vehicles at ground level enabling $10cm$ scale grids of data to be collected (at least of areas visible from the road).

There are still limitations to LiDAR data. There are many details on a terrain

which would be missed if one were to rely solely on remote sensing. There are also limitations on the level of detail that could be used in flood modelling.

The validation and calibration of models still relies on accurate flood data. Images capturing the extent of floods are now more likely to be gathered during an event. Inertial terms are also valuable and more could be done to acquire this data as well.

In summary the amount of LiDAR data available is more than sufficient to support detailed flood simulations of urban areas, yet there is always a need to cross validate this with data from other sources.

2.3 Applying 2D Hydraulic Models

Numerical simulation is a computational technique to find approximate solutions to sets of partial differential equations. There are many different techniques, each with their own strengths and weaknesses. The three main categories are finite difference (FE), finite element (FE) and finite volume (FV) (Mortimer and Mayers, 1994), although this is not exhaustive and schemes may also be hybridised.

Finite difference **FD** schemes describe the values at point on a grid. Between these points the values are not explicitly defined.

Finite element **FE** uses a mesh of triangles or tetrahedra. The values at the vertices are given and points within a cell are linearly interpolated. Other shape functions can be used, though this is uncommon.

Finite volume **FV** methods define the average value in a cell. Values at a specific point is not well defined, although assumption about these are made in order to make calculations.

2.3.1 Parameterisation of Bed Roughness

Bed roughness is a dominant factor in many flow models. In the simplest case the kinematic wave form of momentum conservation is used. This simply equates the bedslope and roughness terms. As a consequence there has been substantial research into the parameterisation of flow resistance. Fully dynamic simulations are also sensitive to this, though not dominated by it in the same way (Horritt and Bates, 2002).

Besides the Manning equation for bed roughness, other terms are used to capture specific aspects of flow resistance. In a few instances these aspects can be dealt with explicitly by more detailed physical models, but most are empirical.

2.3.1.1 Vegetative flow resistance

Flow resistance by emergent river plants varies with the depth of flow. It can be represented by a porosity component and vegetation height (Sellin *et al.*, 2003),(Jain *et al.*, 2004). Several groups including (Musleh and Cruise, 2006) physically modelled this using rods submerged in a shallow flume. This does not fully account for the flexibility of the plants as they can bend in strong currents. It may present a greater surface area to absorb more momentum and may well be flattened during the course of a flood. To represent the former effect (Mason *et al.*, 2003) following (Kouwen, 1988) use a composite parameter MEI representing the vegetative density M, the stems elasticity E and angular inertial I.

The roughness parameter has traditionally been treated as piecewise homogeneous, the patches being segregated by region or observable characteristics of land-use. In channel flow this may produce local anomalies, but gives a reasonable approximation to overall conveyance. In out of bank flows the path of least resistance is less well defined, so variation in ground cover can have a more profound affect on the flow. A simulation of out of bank flow (Morris *et al.*, 2006) showed

how the location of a thin region with high roughness can have a profound impact on out of bank flow.

2.3.1.2 In-bank Floodplain Interactions

The turbulence resulting from flow differentials in compound channels can be a significant momentum sink (Knight and Shiono, 1996). This also applies to floodplain-channel interactions. For example (Morris, 2002) shows a possible effect of this on flood routing. The floodplain filled up quickly during moderate floods, to the point where the channel-floodplain interection started to weaken. This lead to it being given a high roughness. In the extreme flood the same depth was reached before the peak discharge arrived. As a consequence the floodplain could not act as a storage at this point, leading to a more intense peak flow downstream.

The Shiono-Knight method (Knight and Shiono, 1996) uses turbulence terms explicitly, requiring four independent parameters.

2.3.2 Importance of land features

Many features which have notable effects on floodplain flow are best characterised as lines. Connel et. al. (Connell *et al.*, 2001) tested the hydro2de FV package against historic floods in the Waihao River valley, New Zealand. They note that "Obtaining a best fit to the extent of the flooded area showed that the model representation would be considerably improved if above-ground buildings, fences and hedges, and in-water hydraulic structures, could be included in the model detail." Due to accumulated debris, a wire fence produced a difference in depth of 0.1 to 0.3 metres either side.

These features are generally difficult to find from remote sensing data, but are obvious in the land surveys. The question of how to represent complex land features simply and realistically is still open. The usual method is to use mesh re-

finement to focus on hedgerows (Cobby *et al.*, 2003), roadways (Cioffi and Gallerano, 2003), or dykes and embankments (Sauvaget *et al.*, 2000). An alternative proposal, to include such features explicitly as boundary conditions between cells, is presented later in §3.3.5.1.

2.3.3 Urban Flooding

Flooding in urban areas is of great concern due to the greater property values and numbers of people affected. It presents particular difficulties to modellers due to the complexity of the landscape. The layout of the buildings and streets must be accounted for, and this requires a mesh of no more than a 10m scale (Schubert *et al.*, 2008). Simulations on this scale were practical without the detailed topographic data that remote sensing can now provide. Smaller features such as garden fences also abound, which will not be evident from LiDAR data. Underground channels, such as sewers and subways can be significant. This complexity is a challenge to represent adequately and also with regards to calibration and verification of the models used. Buildings and networks of roads need to be represented accurately. Representing solid obstacles presents a particular challenge. Many urban flooding benchmarks (see chapter 4) specifically present this challenge. Anisotropic porosity Guinot and Soares-Frazao (2006); l'Homme *et al.* (2006); Sanders *et al.* (2008) treats large clusters of buildings as a single homogenous region. The density of buildings in this region is represented by a porosity value. The water level in this region, boundary lengths and other such parameters all take this porosity into account. Head loss is calculated for cells as water enters this region and as it flows through this region. A refinement to the anisotropic porosity model is to allow the porosity to vary within a region. (Velickovic *et al.*, 2010) The main object of this refinement is to smooth the transition between regions.

Sub-grid-scale models parameterise objects in a cell both by the flow resistance and by their shape and size.Yu and Lane (2006) The height-density function is used to displace water within the cell according to the volume of the subgrid features submerged.

If an unstructured mesh is used this can be adapted to the shapes of the buildings and used to create a no-flow region within the domain. (Schubert *et al.*, 2008)

A similar method though with a slightly different philosophy is to focus on the mesh shape on the streets. (Paquier *et al.*, 2001) The streets are treated as a network of channels leading to a hybrid of 1D and 2D models.

The Cartesian cut-cell methods presented offer a potential solution to at least some of the issues presented here. They enable buildings to be represented at a sub-grid scale. The potential to represent linear features is also relevant, although this is not pursued in depth here. Underground flow channels have received less attention. Leandro *et al.* (2009) use a 1D sewer model together with a 2D surface flow model. This issue is not explored any further in this study.

2.3.4 Appropriate Scale

The improvements in computer technology have made very detailed mesh refinement possible, but not trivial. In two dimensions with an adaptive time-step the computational expense is multiplied by eight when the cell width is halved.

The quality of survey data must inform the appropriate level of detail. Remote sensing terrain maps are available at a resolution of 10cm, but may contain anomalies if applied directly at that scale. Channel cross sections in the UK are usually available for every 100m to 200m of reach.

The refining the mesh reduces numerical errors, allows more detailed terrain data to be included and mitigates instabilities arising from wetting and drying

on steep bed-slopes. The numerical errors need only be negligible compared with other uncertainties in parameterisation and boundary conditions. The data available is quite detailed, but sets a definite lower limit on grid scale. This must be balanced against the gains to be made by Monte-Carlo simulations, which are necessary for calibration, and useful for examining confidence bounds. Consequently, it is desirable to find ways to obtain a stable solution on a coarse grid. A method to deal with the wetting and drying problem is developed in §3.3.3.

Chapter 3

Method

3.1 Research Challenges

The main goal of this research is to develop AMAZON-CC as a tool for flood impact assesment. This goal is most relevant for urban environments where there is the greatest potential for harm. Hydraulic models of such environments must be sufficiently detailed to capture the dynamics of flows along individual streets.

AMAZON-CC (Section 3.2) is designed with computational efficiency in mind. The Finite Volume is fully explicit, updating the status at each cell locally. Intercell fluxes are found using the 2-shock approximate solution to the Riemann problem, which emphasises computational efficiency. The use of a Cartesian mesh improves runtime efficiency, and also makes parallel processing easier to achieve. This efficiency makes AMAZON-CC well suited for the level of detail required in urban flood modelling.

3.1.1 Wetting and Drying

A common problem encountered with FV solvers for the shallow water equations is wetting and drying. The interaction between bed slope source terms with the fluxes between cells produce instabilities. The Surface Gradient Method (Sec-

tion 3.2.4.3) mitigates these instabilities, but does not seem to help at the wet-dry boundary. The Volume to Free-surface Relationship Method (Section 3.3.3.3) provides a restrictive regime at the wet-dry boundary which prevents the instabilities arising.

3.1.2 Parameterization

Describing flood events requires a large and complex data-set. The need to calibrate hyraulic models for extreme events, poses a difficulty. The number of uncertain parameters should be kept low. This is less of an issue when solving the full SWE compared with more diffusive forms of the equation. The solution is less sensitive to roughness parameters, and depends more on topography (Horritt and Bates, 2002).

Much of the data used is highly detailed and so it is of great benefit if this can be interpreted in its native format. The data to be parsed includes; Digital Elevation Models, vector data of obstacles and regions, time series of depth and discharge boundary conditions. A keyword driven data parser (Section 3.3.1) was written to allow data to be entered simply and flexibly. Functionality also needed to be added to support a wide variety of boundary conditions (Section 3.3.2).

3.1.3 Delineating floodplain features

A floodplain has many features which can affect flow. Not all such features can be represented adequately by topography.

Urban areas contain buildings and other solid features. The Cartesian cut-cell method (Section 3.2.6) provides a useful way to represent these. Areas with different land-use can also be defined using these routines to define regions (Section 3.3.5.1).

The potential value of the cut-cell method has not been fully explored. Much

of the architecture of the program was reimplemented with this potential in mind. Cut cells which permit flow on both sides of the boundary (Section 3.3.5.2) can be defined. A proof of concept is presented in Section 4.5.

A particular challenge introduced by cut-cells is cell reconstruction. The layout of the Cartesian mesh allows the gradients in the two orthogonal directions to be found seperately. The presence of cut-cells negates this. A linear programming method was written to find the gradients in both directions to be found together.

3.2 AMAZON-Cut Cell

AMAZON is the name for a suite of simulation tools being developed by the Centre for Mathematical Modeling and Flow Analysis at Manchester Metropolitan University. At its core is a finite volume method used to solve the shallow water wave equations. This uses a Harten, Lax and van Leer approximate Riemann solution to determine intercell fluxes. It uses a two step Godunov schema to achieve second order accuracy with both the time step and the mesh resolution. This has been shown to be effective in a number of shallow water flow scenarios (Mingham and Causon, 1998; Causon *et al.*, 1999; Ingram *et al.*, 2003).

The research presented here uses AMAZON Cartesian cut-cell (AMAZON-CC). This uses a regular Cartesian grid, with the option to embed impermeable features accurately within this domain. This approach allows for efficient run-time performance and is well-suited to parallel processing.

Most of the code used in this research was extant, but much of it was rewritten to add flexibility and the experimental features below. The features present in the original code are descibed in the current section. Refinements and additions made in the course of this study are described in Section 3.3.

3.2.1 Shallow Water Equations

The shallow water wave equations (SWE) give a planar 2D representation of single fluid free surface flow. The 1D form of these equations is known to hydrologists as the *de Saint Venant* equations. They are derived from the Euler equation for ideal fluids under the assumption that the depth is relatively small ($<\approx 1:20$) in comparison to surface wavelengths. They are given in conservative form by equations 3.1 onwards. $\mathbf{U}$ is the a vector of conserved variables given by 3.2. $\mathbf{F}$ and $\mathbf{G}$ in 3.3 are the fluxes consisting of a transport terms $\mathbf{v} \cdot (\mathbf{x}, \mathbf{y})\mathbf{U}$ plus gravity potential $gh \times g\eta$. The source terms $\mathbf{S_b}$ and $\mathbf{S_f}$ in 3.4 introduce bedslope and

bed roughness terms respectively. The Chezy roughness coefficient C_b is used by default, although where sources have specified a value for the Manning coefficient n this is used instead. Turbulence is not explicitly accounted for in this version of the equation.

$$\mathbf{U_t} + \mathbf{F_x} + \mathbf{G_y} = \mathbf{S} \tag{3.1}$$

$$\mathbf{U} = \begin{pmatrix} \phi \\ \phi u \\ \phi v \end{pmatrix} = \begin{pmatrix} gh \\ ghu \\ ghv \end{pmatrix} \tag{3.2}$$

$$F = \begin{pmatrix} \phi u \\ \phi u^2 + \frac{1}{2}\phi^2 \\ \phi uv \end{pmatrix} \quad \mathbf{G} = \begin{pmatrix} \phi v \\ \phi uv \\ \phi v^2 + \frac{1}{2}\phi^2 \end{pmatrix} \tag{3.3}$$

$$\mathbf{S_b} = \begin{pmatrix} 0 \\ \phi \frac{\partial}{\partial x} z_b \\ \phi \frac{\partial}{\partial y} z_b \end{pmatrix} \quad \mathbf{S_f} = \begin{pmatrix} 0 \\ \frac{u\sqrt{u^2+v^2}}{C_b^2} \\ \frac{v\sqrt{u^2+v^2}}{C_b^2} \end{pmatrix} \tag{3.4}$$

3.2.2 Finite Volume Approximation

Finite volume methods use matrix of discrete straight-edged cells which span the domain. They calculate the mean cell value for each of the conserved quantities using the integral form of the equation. The flux terms when averaged over a cell become dependent on cell edge values due to the divergence theorem,

$$\int_C \nabla \cdot \mathbf{F} = \oint_{\mathbf{E}} \mathbf{F} \cdot \mathbf{n} \tag{3.5}$$

yielding,

$$\int_C \mathbf{U_t} + \oint_{\mathbf{E}} \mathbf{F} \cdot \mathbf{n} = \int_{\mathbf{C}} \mathbf{S_b} + \mathbf{S_f} \tag{3.6}$$

To discretise this the variables and source terms are identified with cell centre values. Each side of the cell forms an interface with either a neighbouring cell or the edge of the domain. The mean flux is found for each edge from the values on either side. This uses a physical submodel (the Riemann problem) to give valid results even where there is a large difference in variables between neighbouring cells.

$$A\left(\bar{\mathbf{U}}(t_1) - \bar{\mathbf{U}}(t_0)\right) + \sum_S l_S(\mathbf{F_S}, \mathbf{G_S}) \cdot \tilde{\mathbf{n}}_\mathbf{S} \mathbf{\Delta t} = \mathbf{A}\bar{\mathbf{S}}_\mathbf{b} \mathbf{\Delta t} + \mathbf{A}\bar{\mathbf{S}}_\mathbf{f} \mathbf{\Delta t} \tag{3.7}$$

For a regular Cartesian mesh with cells of dimensions Δx by Δy, each cell C has area $A = \Delta x \times \Delta y$. There are four sides North, South East and West labelled hereon as $\mathcal{N}, \mathcal{S}, \mathcal{E}, \mathcal{W}$. The discretised fluxes and edge lengths are given in table 3.1.

Table 3.1: Parameters of the flux terms of a rectangular grid cell and their locations relative to the centre (x, y)

	North	South	East	West
$(x_\mathcal{F}, y_\mathcal{F})$	$(x, y + \frac{1}{2}\Delta y)$	$(x, y - \frac{1}{2}\Delta y)$	$(x + \frac{1}{2}\Delta x, y)$	$(x - \frac{1}{2}\Delta x, y)$
$l_\mathcal{F}$	Δx	Δx	Δy	Δy
$(\mathbf{F}_\mathcal{F}, \mathbf{G}_\mathcal{F}) \cdot \mathbf{n}_\mathcal{S}$	$\mathbf{G}_\mathcal{N}$	$-\mathbf{G}_\mathcal{S}$	$\mathbf{F}_\mathcal{E}$	$-\mathbf{F}_\mathcal{W}$

3.2.3 The HLL Riemann Solver

The Harten Lax and Leer (HLL) approximate Riemann solution is used (Harten *et al.*, 1983).

3.2.3.1 Characteristic Waves

If the source terms are ignored the shallow water wave equations can be analysed by finding characteristic lines. The intercell flux is strictly normal to the boundary, so for the purpose of the methods derived here only one dimension needs to be considered. Using the chain rule the simplified form of the SWE

$$\frac{\partial \mathbf{U}}{\partial t} + \frac{\partial \mathbf{F}}{\partial x} = \mathbf{0} \tag{3.8}$$

becomes,

$$\frac{\partial \mathbf{U}}{\partial t} + \frac{\partial \mathbf{F}}{\partial \mathbf{U}} \cdot \frac{\partial \mathbf{U}}{\partial x} = 0 \tag{3.9}$$

If values of $\mathbf{U} = \mathbf{U_c}$ can be found such that $\frac{\partial \mathbf{F}}{\partial \mathbf{U}}$ is a constant c, then any line $x = ct + m$ on which $\mathbf{U}(\mathbf{t_0}, \mathbf{x_0}) = \mathbf{U_c}$ will have a constant value for $\mathbf{U}$. This in itself is useful for specific cases, but it turns out that this property holds for a large family of such values.

The term $\frac{\partial \mathbf{F}}{\partial \mathbf{U}}$ forms a Jacobian matrix J.

$$J = \begin{pmatrix} \frac{\partial}{\partial \phi}\phi u & \frac{\partial}{\partial \phi}\left(\phi u^2 + \frac{1}{2}\phi^2\right) & \frac{\partial}{\partial \phi}\phi uv \\ \frac{\partial}{\partial \phi u}\phi u & \frac{\partial}{\partial \phi u}\left(\phi u^2 + \frac{1}{2}\phi^2\right) & \frac{\partial}{\partial \phi u}\phi uv \\ \frac{\partial}{\partial \phi v}\phi u & \frac{\partial}{\partial \phi v}\left(\phi u^2 + \frac{1}{2}\phi^2\right) & \frac{\partial}{\partial \phi v}\phi uv \end{pmatrix} \tag{3.10}$$

$$J = \begin{pmatrix} 0 & -u^2 + \phi & -uv \\ 1 & 2u & v \\ 0 & 0 & u \end{pmatrix} \tag{3.11}$$

The eigenvectors for this matrix are given in equations 3.12.

$$\lambda_1 = u - \sqrt{\phi} \quad \lambda_2 = u \quad \lambda_3 = u + \sqrt{\phi} \tag{3.12}$$

By finding a linear transformation of the variables which diagonalises the Ja-

cobian matrix, the equation may be split into three independent equations. These may be evaluated using sets of characteristic lines, although the wavespeeds will not necessarily be constant. The Riemann class of solvers manage to produce a stable solution with linear terms by solving a simplified case in which all the characteristic lines are constant. This is the Riemann problem.

3.2.3.2 The Riemann Problem

The family of Riemann problems are applicable over the field of hyperbolic conservation laws, expressed in one spatial dimension. The initial state is a discontinuity. The values on either side are both uniform. Due to the nature of the laws applied a basis can be found which separates the variables into distinct vectors, each of which is constant along its specific linear trajectory. Each such trajectory is called the characteristic wave speed. The solution to the Riemann problem can be analysed according to the relationship between the two sets of characteristics.

The SWE produces three characteristic lines each for $U_{\mathcal{L}}$ and $U_{\mathcal{R}}$. Each pair of corresponding characteristic lines may form a shock wave with a single discontinuity formed somewhere between them or a rarefaction wave.

$$\begin{aligned} \mathbf{U}(\mathbf{x}, \mathbf{0}) &= \mathbf{U}_{\mathcal{L}} \quad \forall x < 0 \\ \mathbf{U}(\mathbf{x}, \mathbf{0}) &= \mathbf{U}_{\mathcal{R}} \quad \forall x \geq 0 \end{aligned} \tag{3.13}$$

3.2.3.3 The Solver

The HLL solution uses the two extreme characteristic wave speeds $V \cdot n \pm \sqrt{\phi}$ to estimated the flux. Finding the nature and parameters of these waves is not trivial. The estimates used here in equations 3.14 - 3.18, are taken from (Toro, 1992). Their derivation assumes that left and right pairs of characteristics form rarefaction waves. This will not always be accurate but will give stable physically meaningful results in all cases (Fraccarollo and Toro, 1995).

The middle characteristic is not used here, but it is worthwhile keeping in mind when comparing this approach with other Riemann solvers. This characteristic line separates the lateral velocity components from each side. If this approach was adapted to include solute or suspended sediment transport it would separate these terms as well.

If both wave speeds are travelling in the same direction then the flow is convective, and the flux is determined entirely by the upstream cell. If not then an approximation is required to the boundary flux. This is done by taking what is known about the flow at the extrema and using the conservation laws to infer the mass and momentum remaining between them.

$$u^* = \frac{u_\mathcal{L} + u_R}{2} + \sqrt{\phi_\mathcal{L}} - \sqrt{\phi_\mathcal{R}} \tag{3.14}$$

$$\sqrt{\phi^*} = \frac{\sqrt{\phi_\mathcal{L}} + \sqrt{\phi_\mathcal{R}}}{2} + \frac{u_\mathcal{L} - u_\mathcal{R}}{4} \tag{3.15}$$

$$S_\mathcal{L} = min\left\{u_\mathcal{L} - \sqrt{\phi_\mathcal{L}}, u^* - \sqrt{\phi^*}\right\} \tag{3.16}$$

$$S_\mathcal{M} = u^* \tag{3.17}$$

$$S_\mathcal{R} = max\left\{u_\mathcal{R} + \sqrt{\phi_\mathcal{R}}, u^* + \sqrt{\phi^*}\right\} \tag{3.18}$$

The four regions separated by these pairs of lines will have a constant value. The leftmost and rightmost regions have the original values. It is possible but computationally expensive to find the state of the intermediate regions using the eigenvalues derived above. This is the basis of the Roe Riemann Solver.

The “star” region is estimated by integrating the SWE over an arbitrary time-

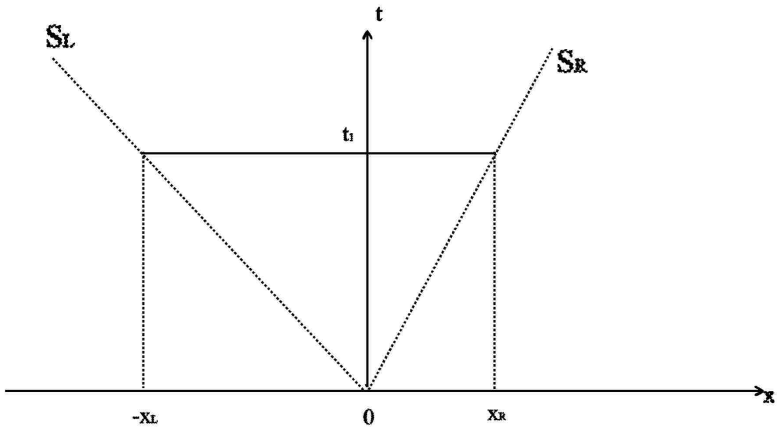

Figure 3.1: A simplified solution to the generalised Riemann problem, giving the left and right characteristic wavespeeds and the integral regions used to derive the HLL Riemann flux terms.

period τ and the regions containing each characteristic. We label the extent of each $x_{\mathcal{L}} = S_{\mathcal{L}}\tau$, $x_{\mathcal{R}} = S_{\mathcal{R}}\tau$. Equations 3.19,3.20 give the relationship between unknowns $\mathbf{U}^*$ and $\mathbf{F}^*$, and it is straightforward to derive each of these as equations 3.21, 3.22.

$$\begin{aligned} 0 &= \int_{t=0}^{\tau}\int_{x=x_{\mathcal{L}}}^{0} \frac{\partial \mathbf{U}}{\partial t} + \frac{\partial \mathbf{F}}{\partial x}\, dxdt \\ &= \int_{x=x_{\mathcal{L}}}^{0} \mathbf{U}(\tau,\mathbf{x}) - \mathbf{U}(\mathbf{0},\mathbf{x})\, dx + \int_{t=0}^{\tau} \mathbf{F}(\mathbf{t},\mathbf{0}) - \mathbf{F}(\mathbf{t},\mathbf{x}_{\mathcal{L}})\, dt \\ &= -x_{\mathcal{L}}\left(\mathbf{U}^* - \mathbf{U}_{\mathcal{L}}\right) + \tau\left(\mathbf{F}^* - \mathbf{F}_{\mathcal{L}}\right) \end{aligned} \tag{3.19}$$

$$\begin{aligned} 0 &= \int_{t=0}^{\tau}\int_{x=0}^{x_{\mathcal{R}}} \frac{\partial \mathbf{U}}{\partial t} + \frac{\partial \mathbf{F}}{\partial x}\, dxdt \\ &= \int_{x=0}^{x_{\mathcal{R}}} \mathbf{U}(\tau,\mathbf{x}) - \mathbf{U}(\mathbf{0},\mathbf{x})\, dx + \int_{t=0}^{\tau} \mathbf{F}(\mathbf{t},\mathbf{x}_{\mathcal{R}}) - \mathbf{F}(\mathbf{t},\mathbf{0})\, dt \\ &= x_R\left(\mathbf{U}^* - \mathbf{U}_{\mathcal{R}}\right) + \tau\left(\mathbf{F}_{\mathcal{R}} - \mathbf{F}^*\right) \end{aligned} \tag{3.20}$$

$$\mathbf{U}^* = \frac{\mathbf{S}_{\mathcal{R}}\mathbf{U}_{\mathcal{R}} - \mathbf{S}_{\mathcal{L}}\mathbf{U}_{\mathcal{L}} - (\mathbf{F}_{\mathcal{R}} - \mathbf{F}_{\mathcal{L}})}{\mathbf{S}_{\mathcal{R}} - \mathbf{S}_{\mathcal{L}}} \tag{3.21}$$

$$F^* = \frac{S_{\mathcal{L}}S_{\mathcal{R}}\left(\mathbf{U}_{\mathcal{R}} - \mathbf{U}_{\mathcal{L}}\right) + S_{\mathcal{R}}\mathbf{F}_{\mathcal{L}} - \mathbf{S}_{\mathcal{L}}\mathbf{F}_{\mathcal{R}}}{S_{\mathcal{R}} - S_{\mathcal{L}}} \tag{3.22}$$

In summary the HLL Riemann solver gives one of three possible fluxes depending on the wavespeeds S_L and S_R (equation 3.23). The conceit of a sharp transition at each cell edge may seem strange, but only if one expects each cell to be a complete physical model in its own right. The resulting calculations have been shown to be accurate globally, and robust locally. The benefits are of reproducing the non-linear features of flow, while conserving mass and momentum at a low computational.

$$\mathbf{F}\left(\mathbf{U}^{*}\right)=\begin{cases}\mathbf{F}_{\mathcal{L}} & if S_{\mathcal{L}}\geq 0\\ \mathbf{F}^{*} & if S_{\mathcal{L}}<0<S_{\mathcal{R}}\\ \mathbf{F}_{\mathcal{R}} & if S_{\mathcal{R}}\leq 0\end{cases} \tag{3.23}$$

Some problems encountered with this method are discussed below 3.3.3 with solutions to this. Indeed this forms a significant portion of this thesis. It should be noted here, however, that these difficulties are also encountered by exact Riemann solvers, and so the approximations used here are not responsible for this.

3.2.4 Cell profile reconstruction

To achieve accuracy in space the values in a cell vary linearly to match as closely as practical the neighbouring cell values. For rectangular cells the North and South vectors, to the respective cell centres, are orthonormal to the West and East vectors. This allows the gradients in each direction to be found independently. Finding gradients on cut cells is more involved and will be dealt with in §3.3.4.

3.2.4.1 Flux Limiters

The best approximation to a local gradient is equal to the gradient between the two neighbours $\mathbf{U_x}\approx\left(\mathbf{U}_{\mathcal{E}}-\mathbf{U}_{\mathcal{W}}\right)/\mathbf{2\Delta x}$. However, if this is used directly instabilities may arise as the dominant error term is prone to positive feedback. Total variance diminishing (TVD) schemes are those which lead to a diminishing net variance $|V|$ in the source terms. This net variance is quantified by some measure (typically ℓ or ℓ^2) of the local gradient integrated over the domain. Preventing the growth of this measure naturally also limits the growth of the oscillations related to the instabilities of 2nd order methods. Flux limiters (Roe, 1986) are one mechanism to impose the TVD condition while achieving close to 2nd order accuracy. It was developed for finite difference methods but bases its calculations on local fluxes. It does rely on the flux splitting of the Roe solver so that the *monotone upwind*

direction of flow can be found explicitly. The monotone upwind and the 2nd order accurate estimates of flux are averaged, with a parameter φ controlling the relative weightings 3.24. The ratio r (3.25) measures the local change in gradient (Sweby, 1984), the reference point k is chosen to centre around the upstream cell. This ratio has been found to be a reliable predictor of instabilities. There are several functions which can used to derive φ. All produce values in the TVD region satisfying equation 3.26, and all must be symmetric as in equation 3.27.

$$\mathbf{F}_{\varphi} = (\mathbf{1} - \varphi)\mathbf{F_{O1}} + \varphi\mathbf{F_{O2}} \tag{3.24}$$

$$r = \frac{u_{k+1} - u_k}{u_{i+1} - u_i} \tag{3.25}$$

$$0 \leq \left(\frac{\varphi(r)}{r}, \varphi(r)\right) \leq 2 \tag{3.26}$$

$$\frac{\varphi(r)}{r} = \varphi(\frac{1}{r}) \tag{3.27}$$

3.2.4.2 Slope Limiters

In finite volume methods 2nd order accuracy is achieved by cell profile reconstruction. Because the flux limiter functions are based on local gradients, they can be readily adapted to produce slope limiter functions. The values at the cell interfaces can be estimated to be either the value in the upstream cell (monotone upwind) the average of the neighbouring cell values (which is 2nd order estimate). Applying a flux limiter on these estimates gives 3.28. Note that the measure used here is Sweby's r as in equation 3.29. This is centred on the cell rather than the cell interface, but possesses similar properties and is used in the same way. The values on opposite faces are found using a slope limiter parameter $\gamma(R)$ as in

(3.30). By assuming that the cell profile is linear, and using (3.27 it is possible to find a relationship between the slope limiter and the flux limiter (3.31). The symmetric property also for slope limiters as in 3.32.

$$\begin{aligned} \mathbf{U_{i+\frac{1}{2}}} &= (\mathbf{1} - \varphi(\mathbf{r}))\,\mathbf{U_i} + \tfrac{\mathbf{1}}{\mathbf{2}}\varphi(\mathbf{r})\,(\mathbf{U_i} + \mathbf{U_{i+1}}) \\ \mathbf{U_{i-\frac{1}{2}}} &= \left(\mathbf{1} - \varphi(\tfrac{\mathbf{1}}{\mathbf{r}})\right)\mathbf{U_i} + \tfrac{\mathbf{1}}{\mathbf{2}}\varphi(\tfrac{\mathbf{1}}{\mathbf{r}})\,(\mathbf{U_{i-1}} + \mathbf{U_i}) \end{aligned} \tag{3.28}$$

$$r \;\; = \tfrac{\mathbf{U_{i+1}} - \mathbf{U_i}}{\mathbf{U_i} - \mathbf{U_{i-1}}} \;\; = \tfrac{\mathbf{G_R}}{\mathbf{G_L}} \tag{3.29}$$

$$\begin{aligned} \mathbf{U_{i+\frac{1}{2}}} &= \mathbf{U_i} + \tfrac{\mathbf{1}}{\mathbf{2}}\gamma(\mathbf{r})\,(\mathbf{U_{i+1}} - \mathbf{U_{i-1}}) \\ \mathbf{U_{i-\frac{1}{2}}} &= \mathbf{U_i} - \tfrac{\mathbf{1}}{\mathbf{2}}\gamma(\tfrac{\mathbf{1}}{\mathbf{r}})\,(\mathbf{U_{i+1}} - \mathbf{U_{i-1}}) \end{aligned} \tag{3.30}$$

$$\varphi(r) = \gamma(r)\left(\frac{r+1}{r}\right) \tag{3.31}$$

$$\gamma(r) = \gamma(\frac{1}{r}) \tag{3.32}$$

Using the above relationships it is possible to derive the slope limiter from the flux limiter in terms of the measure r. Since the estimated gradient $(u_{i+1} - u_{i-1})/\Delta x = \frac{1}{2}\left(\mathcal{G}_{\mathcal{L}} + \mathcal{G}_{\mathcal{R}}\right)$ the limited gradient can also be derived more directly in terms of the left and right gradients. The limiters used are given in tables 3.2,3.3. The min-mod limiter is the most stable limiter. The superbee limiter is at the most accurate.

3.2.4.3 Surface gradient method

This solver uses the surface gradient method, introduced by (Zhou *et al.*, 2001). This treats still water conditions as the basis for the 1st order accurate estimate of depth gradients, i.e. a level surface profile. This is a good approximation for subcritical flow over uneven bathymetry, as the variations in pressure due to

Table 3.2: slope limiters used and their corresponding flux limiters. Note that for all limiters if $r <= 0$ (*i.e.* the left and right gradients have opposite signs) the flux term is monotonic and so the gradient is zero.

	$\varphi(r)$	$\gamma(r)$
min-mod	$\min(1, r)$	$\min\left(\frac{2}{1+r}, \frac{2r}{1+r}\right)$
superbee	$\min(\max[1, r], 2, 2r)$	
Van Albada	$\frac{r^2+r}{r^2+1}$	$\frac{2r}{r^2+1}$
Van Leer	$\frac{2r}{r+1}$	$\frac{4r}{(r+1)^2}$

Table 3.3: The gradient limiters as used in the AMAZON algorithm. Note the condition $r <= 0$ is equivalent to $\mathrm{sgn}(\mathcal{G}_\mathcal{L}) \neq \mathrm{sgn}(\mathcal{G}_\mathcal{R})$ where the gradient is zero. Hence the formulae above use the parameter $s = \mathrm{sgn}(\mathcal{G}_\mathcal{L}) = \mathrm{sgn}(\mathcal{G}_\mathcal{R})$

	$\mathcal{G}(\mathcal{G}_\mathcal{L}, \mathcal{G}_\mathcal{R})$
min-mod	$s \cdot \min(\lvert\mathcal{G}_\mathcal{L}\rvert, \lvert\mathcal{G}_\mathcal{R}\rvert)$
superbee	$s \cdot \max[\min(2\lvert\mathcal{G}_\mathcal{L}\rvert, \lvert\mathcal{G}_\mathcal{R}\rvert), \min(\lvert\mathcal{G}_\mathcal{L}\rvert, 2\lvert\mathcal{G}_\mathcal{R}\rvert)]$
Van Albada	$\frac{\lvert\mathcal{G}_\mathcal{L}\rvert \cdot \mathcal{G}_\mathcal{R} + \mathcal{G}_\mathcal{L} \cdot \lvert\mathcal{G}_\mathcal{R}\rvert}{\lvert\mathcal{G}_\mathcal{L}\rvert + \lvert\mathcal{G}_\mathcal{R}\rvert}$
Van Leer	$\frac{2\mathcal{G}_L\mathcal{G}_R}{\mathcal{G}_L + \mathcal{G}_R}$

depth matches those due to the bathymetry, while the kinetic term is relatively small. Where the flow is supercritical the physical constraints of bathymetry often prevent this method being applied, as a level water profile will often intersect the bed.

Since stability is a precondition for any steady state solution, choosing a gradient which conforms with this might be considered appropriate. An analysis of such gradients can be made from the Bernoulli equation 3.33 and conservation of mass.

$$H = h + z_b + \frac{1}{2}\frac{v^2}{g} \tag{3.33}$$

For low Froude numbers this is dominated by the first two terms. It is possible to find the relationship precisely as 3.34. From this it is apparent that under subcritical flow conditions, the default for stability is a low surface gradient, while for supercritical conditions a small depth gradient is preferred.

$$\begin{aligned} \frac{\partial h}{\partial x} &= \frac{1}{F_r^2 - 1}\frac{\partial z_b}{\partial x} \\ \frac{\partial \eta}{\partial x} &= \frac{F_r^2}{F_r^2 - 1}\frac{\partial z_b}{\partial x} \end{aligned} \tag{3.34}$$

3.2.5 Time step

3.2.5.1 The Godunov Scheme

Second order accuracy in time is achieved through a two phase process. In the prediction phase, an estimate of the variables at the half time-step $t_{predict} = t_{start} + \frac{1}{2}\Delta t$ based on the values and gradients in the cell. In the correction phase the values after the full time-step $t_{correct} = t_{start} + \Delta t$ is calculated based on the estimated state from the prediction step. In order to ensure stability the slope limited gradients are not recalculated.

3.2.5.2 The Cauchy stability condition

To ensure the influence of wave fronts are restricted to one cell alone, a time step is imposed based on the local wave speeds. The Cauchy parameter C_a is used to control the time step 3.35, where $\lambda_{x,y}(i,j)$ is the maximum wavespeed in each direction 3.36.

$$\begin{aligned} \lambda_x(i,j)\delta t <= C_a \delta x \\ \lambda_y(i,j)\delta t <= C_a \delta y \quad \forall i,j \end{aligned} \tag{3.35}$$

$$\begin{aligned} \lambda_x = |u| + \sqrt{\phi} \\ \lambda_y = |v| + \sqrt{\phi} \end{aligned} \tag{3.36}$$

3.2.6 Cartesian cut cells

AMAZON-CC uses a uniform rectangular mesh. This makes it possible to treat the gradients in each direction separately, allowing simple and accurate cell reconstruction. The Cartesian cut-cell (CC) method (Yang *et al.*, 1997),(Ingram *et al.*, 2003) allows objects and boundaries of arbitrary shape to be embedded in this mesh without warping. Instead the rectangular cells are cut to accommodate them as shown in figure 3.2. The methods applied to these cut-cells are largely the same as for any irregular cell. The use described here is the embedding of impermeable obstacles on the mesh. Further uses of the method are explored in 3.3.5.

3.2.6.1 Cell Merging

The time step depends on the size of the smallest element 3.35. In order to avoid arbitrarily small time steps a minimum size is imposed. In this application this is half the area of an uncut cell. The undersized cells are merged with a larger neighbour, and all calculations made as if the composite cell were one cell. The

cell which intersects with the normal to the centre of the cut is chosen as the "parent" cell 3.2. In the case of moving bodies, this merging process occurs prior to both the prediction and correction phases of the time-step, and is logistically quite complex.

3.2.6.2 Gradients

The gradient is found as if the cell were a rectangular cell. In order to account for the solid face, the gradient is also found in each direction as if one side were entirely solid. A weighted average of these gradients is taken in each direction. The weight depends on the degree to which the solid side obstructs flow in the direction of the gradient. Although, it is not derived from the theory of slope limiting functions described in chapter 3.2.4, it has been applied without difficulty in a number of applications.

An alternative to this approach is presented chapter 3.3.4.

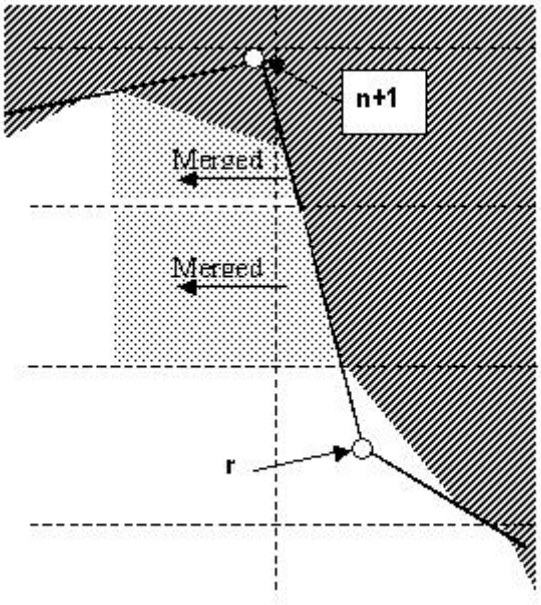

Figure 3.2: Section of a Cartesian mesh with solid areas derived from the intersection points between polygon edges and grid lines. Solid cells and solid areas of cut-cells are shaded. Vertices are listed anti-clockwise around the body. Smaller cells are merged with their neighbour across the longest edge.

3.3 Extensions and Innovations

The methods presented below are specific adaptations coded, and in some cases devised, by the author specifically for this thesis.

- The data parser 3.3.1 was written by the author.
- The boundary conditions 3.3.2 are substantially new. The solid and transitive boundary conditions had already been written, but that is all.
- The VFR methods 3.3.3.3 were developed by Begnudelli and Sanders (2006) and incorporate code written by the authors. The Piecewise Level interpretation of VFR was developed as part of this thesis.
- The linear programming solution for cut cell gradients 3.3.4, was first developed by Berger *et al.* (2005). The code used here was developed and coded independently.
- The routines to outline polygon regions 3.3.5.1 is original, although many of the routines it uses are inherited.
- The SPIn Boundary 3.3.5.2 routines were written by the author, but make use of inherited code. The modifications made are substantial because they anticipate further developments.
- The preprocessing module was largely rewritten.
- Some file output routines are new.

3.3.1 Control File Parser

To add flexibility to the code a keyword driven setup parser was written. The text file "control.dat" is divided into sections each with a separate set of keywords. The first section, "'SYSTEM"', specifies the mandatory parameters and the methods used by the solver. The "'SIMULATION"' section allows the user to input spatial data on any rectangular subsection of the domain. It can read text files and

ASCII DEM files. The "SOLIDS" (cut-cell and polygon) parser reads a list of polygons. Each entry gives the class of polygon, how it is to be implemented and the coordinates of its vertices. The "'BOUNDARY"' (boundary condition) parser, similarly reads time-series data from text files. Sample control files are included in appendix A.

3.3.2 Boundary Conditions

The original version of AMAZON-CC allowed solid and transmissive boundary conditions at the domain edge. The current version of AMAZON-CC has extended this to allow depth and discharge to be specified. These may be included as time-series if required. The use of ghost values at cell boundaries, as opposed to 'ghost cells', is also a novel feature.

Boundary conditions decide how an external cell interfaces with the edge of the domain. The theory behind boundary conditions is based on the differential form of the shallow water equations. In a one dimensional case using one boundary condition for each variable provides ensures a unique solution. This is readily apparent in the steady state case. In a time variable situation, with supercritical inflow from the left and subcritical outflow to the right, even though the initial conditions may involve a smooth transition of velocity from left to right, this state will quickly degenerate. The backflow may propagate toward the left boundary, eventually contradicting the critical inflow condition. The converse case where the outflow evolves to become supercritical, is also feasible. Otherwise a hydraulic jump will emerge. The finite volume method allows for such discontinuities. So it is possible to arrive at a steady state solution to the hydraulic jump, although with no guarantee of uniqueness. Boundary conditions are derived locally, and are subject to the conditions of the cells neighbouring that boundary. Specifically, it is not possible to apply supercritical inflow conditions where the depth of water

contradicts this. As a consequence, especially if discontinuities are likely to emerge, boundary conditions and initial conditions must be considered together. The number of conditions required depends on whether flow normal to the boundary is advective (supercritical) or diffusive (subcritical). For supercritical flow outwards the internal conditions dominate, so there is no boundary condition, and values outside the domain are irrelevant. For supercritical flow inwards one condition is required for each variable. If no alternative is stated then by convention the lateral momentum is assumed to be zero. For subcritical flows one boundary condition is used to determine flux for both mass and outward velocity. Because one condition is not enough to find both ghost values, a further equation is applied to identify the outgoing wave speeds between the ghost values and the internal values,

$$\sqrt{g\tilde{h}} + \tilde{\mathbf{v}} \cdot \mathbf{n} = \sqrt{gh} + \mathbf{v} \cdot \mathbf{n} \tag{3.37}$$

The ghost values are derived from the known boundary condition and an identity between the values on each side of the boundary. Whether transport terms are informed by the boundary condition depends on the net mass flux (or if a contact wave is established through use of a HLLC approach, on the direction of this contact wave).

The use of ghost cells is a common method for implementing boundary conditions. It was noticed in tests by a third party using AMAZON (Yasuda *et al.*, 2011), that ghost-cells can introduce a slight delay to time variable boundary conditions. The current version of AMAZON implements boundary conditions directly at the interface, which seems to be effective in mitigating this effect. This requires three sets of ghost values for each time step, one to find the local gradient, another to for the prediction phase and a third for the correction phase.

3.3.2.1 Solid Boundary

A solid boundary had no mass flux. As a consequence the momentum normal to the boundary is zero. By convention the momentum on the inner side is always taken to be zero, even though cell reconstruction may contradict this. In all but the most transient of cases this is physically realistic. It then follows that the ghost value for depth must match the internal depth.

Table 3.4: Ghost values for a solid boundary in terms of interior values. Note that the presence of a solid boundary does inform the prediction phase.

	gradient	prediction	correction
ϕ	n/a	ϕ	ϕ
ϕu	0	$-\phi u$	$-\phi u$
ϕv	n/a	0	0

3.3.2.2 Transmissive

The transmissive boundary condition was developed for surface wave simulations, where the mean water level does not significantly change. It is intended to allow waves to propagate outward without interference. The ghost values are set to match those inside the boundary.

Because a fully explicit scheme is being used the SWE are effectively being applied to initial value problems even if a steady state solution is required. Assumptions about the correct disposition of boundary conditions that hold for implicit methods, cannot be made for these methods. This is most noticeable when trying to produce supercritical flow into the domain. For initial value problems it would be valid to specify depth and velocity at such a boundary. With the methods used here the depth of water in a cell is determined by conservation of mass. The level will only drop if if the net mass flux is positive. Consequently, and quite true to life, supercritical inflow can be swamped by backflow.

The transmissive boundary conditions are often used where the wetted are extends beyond the domain of interest. This can often cause problems, particularly

where water is flowing out of the domain. This may be remedied by using a more explicit boundary condition to specify the expected behaviour, or by extending the domain beyond the area of interest to a point where the boundary condition no longer influences the results. For steady state problems altering the initial conditions can sometimes work.

Table 3.5: Ghost values for a transmissive boundary in terms of edge values.

	gradient	prediction	correction
ϕ	n/a	n/a	ϕ
ϕu	n/a	n/a	ϕu
ϕv	n/a	n/a	ϕv

3.3.2.3 Free Outflow

The free outflow condition stipulates complete drainage downstream. The ghost value for depth is zero and consequently so are all other values. Since a discontinuity is implied by this condition, there is no affect on the cell gradient.

This boundary condition is a stable alternative to the transmissive boundary condition when the direction of flow is known. It is also helpful in steady flow cases where supercritical outflow is expected.

Table 3.6: Ghost values for a free outflow boundary in terms of edge values.

	gradient	prediction	correction
ϕ	n/a	n/a	0
ϕu	n/a	n/a	0
ϕv	n/a	n/a	0

3.3.2.4 Depth and surface level

The ghost value for h will equal the specified depth. Where this is the only condition at the boundary, equation 3.37 is used to determine the normal momentum.

Table 3.7: Ghost values for a depth boundary in terms of edge values.

	gradient	prediction	correction
ϕ	$g\tilde{h}$	n/a	$g\tilde{h}$
ϕu	n/a	n/a	$\tilde{h}\left(\frac{\phi u}{\phi} + \sqrt{\phi} - \sqrt{g\tilde{h}}\right)$
ϕv	n/a	n/a	ϕv

3.3.2.5 Discharge

The momentum is set as a parameter at the boundary. The depth for subcritical flows is found using equation 3.37. This results in a cubic 3.38 which is solved analytically.

$$g\tilde{h}^3 - \left(\frac{hu}{h} + \sqrt{gh}\right)\tilde{h} - \tilde{hu} = 0 \tag{3.38}$$

Table 3.8: Ghost values for a discharge boundary in terms of edge values. The method for finding the ghost value ϕ is given in the text.

	gradient	prediction	correction
ϕ	n/a	n/a	$\tilde{\phi}_*$
ϕu	$\tilde{Q}/w$	n/a	$\tilde{Q}/w$
ϕv	n/a	n/a	0

3.3.3 Wetting and Drying

Problems arising at the wet-dry boundary have been well documented. (Bates, 2000) (Brufau *et al.*, 2004) (Quecedo and Pastor, 2002) (Tchamen and Kawahita, 2001) (Cea *et al.*, 2007) Accounts of these errors vary depending on the methodology applied. The problem appears to be complex as several assumptions implicit in the numerical methods and the shallow water equations are contravened.

3.3.3.1 Sources of Error

The assumptions behind may be contradicted for a rapidly moving front over a slope. This may be a source of inaccuracy, but is not responsible for the more sig-

nificant errors. The errors are perceived to be more significant when the velocity upslope is small. The Riemann problem assumes uniform initial values on both sides of the discontinuity. A large depth gradient causes this assumption to break down very close to the discontinuity. This has a significant impact on the Cauchy stability criterion. As a result the time step must be reduced. Given the recursive nature of its derivation analysis of the Cauchy criterion at domain boundary encounters specific difficulties. The cell reconstruction finds linear gradients for depth and momentum. Where this reconstruction produces low depths at a cell face, the velocity can be significantly overestimated. This produces an excessive flux through this face. If the downstream cell is empty the resulting values in that cell will reproduce the problem in the following time step. The result of a depth discontinuity is a transport of both mass and momentum. The presence of a bed step mitigates the momentum flux, but not the mass flux. Schema which allow such discontinuities at the cell edge can be Cells at the edge of the waterline may be only partially covered in water. Whether this is the case is contingent on several factors. A cell at the front will have both wet and dry areas. This means that the method for cell reconstruction described in §3.2.4 is insufficient.

In the vicinity of a front, or anywhere where the water level is low and the bed is uneven, the depth of water can vary greatly. In cell reconstruction if the depth at the cell edge is much smaller than the mean cell value then a moderate momentum gradient will produce high velocities. The surface gradient method attempts to produce a straight surface profile between cells, but bed gradient is inflected at the interface between them. Shallow flow over a strongly convex slope will naturally produce this anomaly. The instabilities encountered using this method have, however occurred with a concave bed.

The bedslope has an influence on local wave speeds. This is noticeable where the difference in bed-level across a cell is equal to or greater than the depth of water.

3.3.3.2 Minimum Depth

A common technique to overcome these difficulties is to specify a minimum flow depth h_{min}. If the depth of water in a cell, or at a cell face, is below this threshold it is considered to be zero. This is effective where the bedslope is small or the mesh is sufficiently fine to cope.

Related to this is a momentum depth threshold h_{mom}. If the depth of water falls below this threshold the local velocity is taken to be hu/h_{mom}.

3.3.3.3 Geometric Approach

The VFR was introduced by (Begnudelli and Sanders, 2006), and has been adapted for a rectangular mesh by (Begnudelli and Sanders, 2007). This centres on the formulation of a relationship between mass storage and surface level, assuming a level surface for front cells. The momentum flux is not calculated for front cells. A velocity gradient is used in place of the momentum gradient.

The original method was applied using a triangular mesh. A level-storage relationship has been found for quadrilateral cells has been developed. An alternative approach is developed here which addresses some of the problems with wetting and drying directly.

The approach used here uses a simpler formula, based on a bed form which has the prescribed dimensions, but is shaped to match the assumptions behind the Riemann solver. The cell is divided into four triangular regions, each having one face of the cell as a base and all sharing a vertex at the centre *figure* 3.3. The bed is level is constant for each region, equal to the bed level at the face.

The bed levels are defined at cell vertices. It follows that cell edge values satisfy the equality $z_{b\mathcal{N}}+z_{b\mathcal{S}} = z_{b\mathcal{W}}+z_{b\mathcal{E}}$, so the possibly problematic consideration, where high beds on two sides could be conceived as preventing flow between the two lower beds, does not arise. Also for neighbouring cells the bed level will be equal on

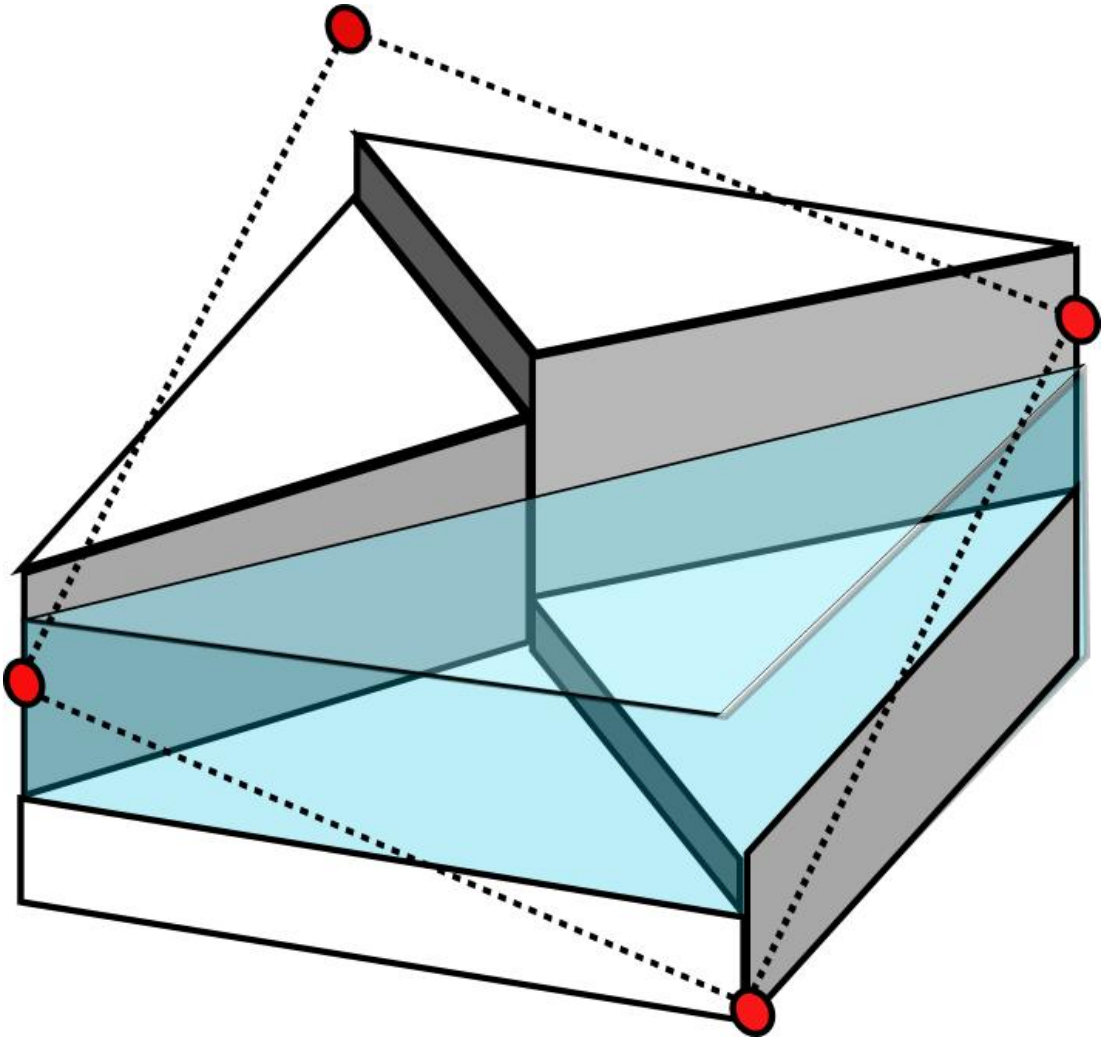

Figure 3.3: Piecewise constant bed reconstruction. Known bed levels at the corners are marked with red circles .

either side of the interface. This is a natural consequence of the original surface gradient method, which this formulation preserves.

Where there is a step change in bed level this adds a pressure source term. There is no other consideration given to how a discontinuous bed profile might affect flow, since the bed form is a property of the method rather than physical reality.

Momentum flux is calculated for partially dry cells. The predictive phase is skipped. Velocity gradient is used instead of momentum gradient.

The additional advantages are:

1. Bed level is not sloped or discontinuous at the points where flux is calculated.
2. The integration of the bedslope source term into the flux calculation is not necessary.
3. The lowest possible water level is equal to the lowest interface bed level, so water will not be left behind when the cell drains.
4. The calculation of surface-level from water volume is simplified considerably.
5. The mean bed level is always equal to the average of the four corner bed levels.

3.3.4 Gradients on Cut Cells

Gradients on cut-cells can not make use of the orthogonality of the axes. There are irregular faces and the cell centroid is displaced. Consequently all faces must be considered irregular and the slopes in both directions must be limited together. Solutions using a scalar limiter reduce gradients in all directions equally. This will produce a stable solution but may be far from optimal.

An analysis of the problem space produces a linear programming problem which can be solved analytically using a simplex algorithm. This approach has been more thoroughly developed by Berger et al.(Berger *et al.*, 2005). The method

here was developed without reference to this work, and so the insight provided can only be applied in retrospect. An important difference in the approaches is in the derivation of the method. The Berger LP limiter is derived analytically from the monotonised central difference, to limit values at the interfaces between cells. This approach is derived by extrapolation from a 1-d min-mod limiter, to limit the observed gradients. The method presented here is slightly more efficient albeit less accurate. The optimum gradient lies outside or on the edge of the region of accepted gradients reducing the problem space.

The method developed here is based, by extrapolation, on the min-mod slope limiter. This does not allow the ordinality of values at the interface to be a reverse of the values at the cell centres. This is achieved by limiting the reconstructed values at the reference point. (Berger *et al.*, 2005) notes that the point at which the flux is calculated is not necessarily in line with the cell centres, and that the limit should be imposed at this point. Although the method presented here ignores this, the strictness of the min-mod limiter ensures instabilities are still avoided.

The inequality imposed by a reference point is given by equation 3.39.

$$\begin{array}{rcccl} U_o & \leq & U_o + \mathcal{G} \cdot \vec{os} & \leq & U_s \quad \textbf{if} \quad U_o < U_s \\ & & \mathcal{G} \cdot \vec{os} & = & 0 \quad \textbf{if} \quad U_o = U_s \\ U_o & \geq & U_o + \mathcal{G} \cdot \vec{os} & \geq & U_s \quad \textbf{if} \quad U_o > U_s \end{array} \tag{3.39}$$

Where the neighbouring value equals the cell value the gradient in that direction is zero. In the case of an inequality this can be simplified. Taking the value at o from all sides and dividing through by the right hand side gives,

$$0 \leq \frac{\mathcal{G} \cdot \vec{os}}{U_s - U_o} \leq 1 \tag{3.40}$$

The measure chosen is a sum of errors, which due to the inequalities are all negative.

$$\begin{aligned} \epsilon &= \sum_s \left| \frac{\mathcal{G}\cdot\vec{os}}{U_s - U_o} - 1 \right| \\ &= N - \mathcal{G} \cdot \sum_s \frac{\vec{os}}{U_s - U_o} \end{aligned} \tag{3.41}$$

A linear programming algorithm was used to find the optimal gradient, which is efficient enough not to dominate computing time.

3.3.5 Other uses of Cartesian cut-cells

Section 2.3.1 states the case for the importance of heterogeneity. The main set of tools available to the AMAZON-CC solver are the cut-cell algorithms. These can be used to define regions or linear features with detail, accuracy and flexibility. The application described here is flow resistance, although there is scope to develop beyond this.

3.3.5.1 outlining a region

Where the domain is divided into subregions to apply distributed parameters or initial values. The cells cut by the outline are still processed as full cells. Instead an averaging process is applied to them to approximate the combined effects of both regions on that particular cell. Note that care must be taken to average the quantity which is directly proportional to its effect on the flow. For example to define a regions Chezy roughness parameter C_b, the cut cell algorithms are used to locate boundaries. On the boundaries the value $R = 1/C_b^2$ is found for the neighbouring regions, since this term is proportionate to the bed shear stress. These values are averaged with weightings equal to the areas of the cell on either side of the boundary $R = \frac{A_1 R_1 + A_2 R_2}{A_c}$, and the Chezy value is found from this $C_b = 1/R^{\frac{1}{2}}$.

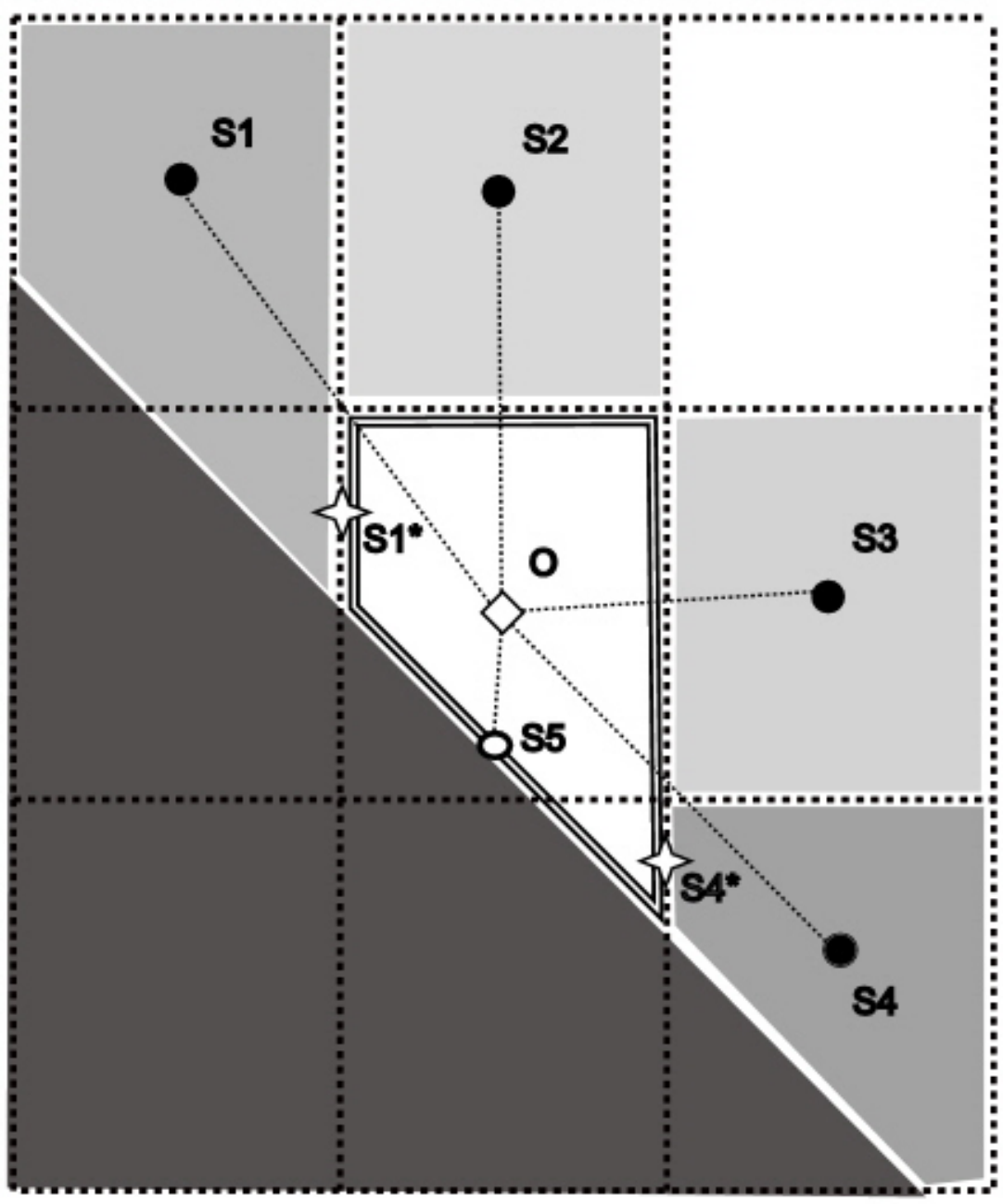

Figure 3.4: Example of a cut cell and the neighbourhood informing its gradient. The cut cell has values at its centre O equal to the mean cell values. The four neighbouring cells similarly have known values at their centres, S1 to S4. The cut face has a normal velocity of zero along its length, considered as a single reference point S5.

3.3.5.2 Semi-Permeable Internal Boundaries

Semi-permeable internal (SPIn) boundaries use the same procedures as the Cartesian cut-cell but define lines rather than regions. They are used to impose solid or partially solid barriers on the domain. In principle the range of boundary conditions that could be applied is very broad, such to introduce a head loss term such as that caused by a bed discontinuity (Zhou *et al.*, 2002), to allow irregularly shaped domain boundaries, or to allow interaction with a 1 dimension submodel. With the discontinuous bed, the momentum balance may be attributed to a lessening in pressure against the side of the step due to flow separation at the top.

The implementation presented here is a mixture of solid and free flow boundaries. The cut side of the cell is treated as two separate faces with the same centre and orientation. The two lengths of these faces sum to the full length of that side, the proportionate length of the free flow face being set by the porosity ψ. A physical interpretation of this would be a set of railings or a latticed wooden fence. This is implemented as a component of urban flood methods some regional porosity models which have been developed to simplify the representation of built up areas (Guinot and Soares-Frazao, 2006; Sanders *et al.*, 2008). In these the boundary porosity is necessary to manage the transition between regions. This is the same as for a solid boundary condition as in chapter 3.3.2.1.

Chapter 4

Results

4.1 Four Mounds

To test the wetting and drying methods described in section 3.3.3 the four mounds test case (Begnudelli and Sanders, 2006) is used. This was run using both VFR formlae with other mitigating measures. All possible combinations were tried, though some failed to produce results.

Figure 4.1 shows the domain and ititial conditions. A rectangular tank 75 metres long by 30 m wide has four cone shaped mounds. The two larger mounds on the centre line of the tank, 3 metres tall with a gradient of 3:10, and their peaks 12.5m and 50m from the left wall. The shorter mounds are 1m tall with a gradient of 1:8, at a distance of 8.75 m either side of the centre line and 30 m from the left wall. A random peturbation of 0 to 0.1 m was added to the bed level at each grid point. Initially the water level is sharply delineated by a line 20m from the left wall. To the left of this the water level is 1.875m, to the right the bed is dry.

The original Quadrilateral Volume - Free surface Relationship (Q-VFR) was tested alongside the piecewise level (PL-VRF) relationship described in section 3.3.3.3. These are compared with a control experiment (C) assuming a uniform

bed slope. Two of the other strategies suggested by Begnudelli and Sanders (2007) were also tested. The first was to base cell reconstruction on velocity gradients (VG) in place of momentum gradients (MG). The second, applied only to the VFR tests. was to sidestep the momentum budget calculation (MF for Momentum Flux) in partially dry cells and instead infer velocity from neighbouring wet cell (IV for inferred velocity).

The assessment of these methods is based on a snapshot of depths and velocities taken 8 seconds after the breach. The results are summarised in Table 4.1.

As a control two experiments were run without using the VFR routines. The former used momentum gradients, while the latter used velocity gradients. The experiment using momentum gradients failed. It produced excessive velocities leading to impractically small time-steps. The experiment using velocity gradients did manage to produced meaningful results (Figure 4.2). In this case there are significant anomalies throughout the right half of the domain. The wetted perimeter appears to have reached the lower right corner of the domain some time before the snapshot was taken.

The results for both VFR bed shapes are very similar. Using VFR with both mitigating strategies (Figures 4.7, 4.6) gives good results with no noticeable anomalies and compare well with the results of (Begnudelli and Sanders, 2006). Avoiding applying momentum flux and source terms, but using momentum gradients (Figure 4.9, 4.8) gives no advantage over the control situation. Calculating momentum source terms and fluxes on the partially dry cells (Figures 4.4, 4.9, 4.8) produces no usable result.

4.1.1 Conclusions

From these results it appears that both of the mitigating methods are required for the VFR approach to be effective. Further tests would be required to confirm this,

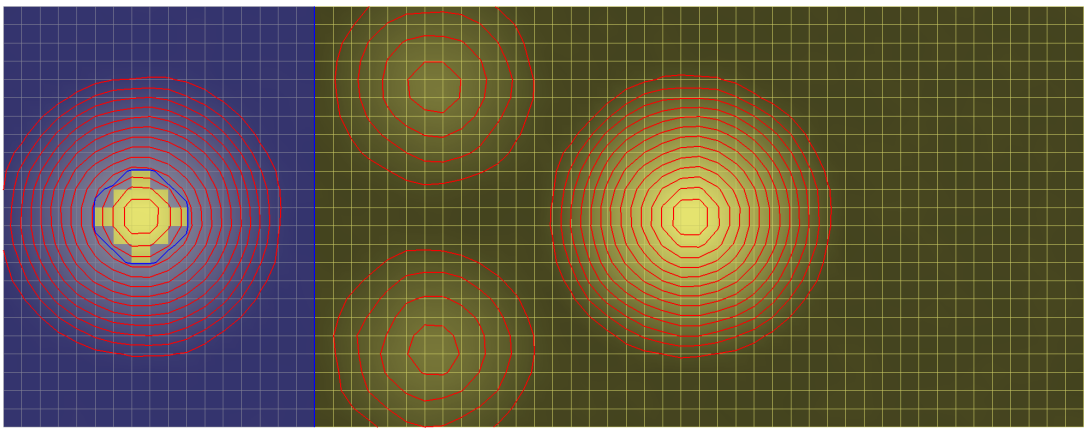

Figure 4.1: The initial state for the four mounds test case. The red contours show bed levels at 0.2 meter intervals. The initially flooded region is shaded and outlined in blue. Discrepancies are due to partially dry cells. The mesh is visible as a pale grid.

but these results are sufficiently clear to justify applying them in the remainder of this study. The piecewise level geometry will be used because it is more runtime efficient, but also as further validation of a new method.

Table 4.1: Summary of results for the four mound test case.

	normal bed	two triangles	piecewise level
momentum gradient	NULL	fig. 4.4	NULL
momentum flux	failed	unusable	failed
momentum gradient	NULL	fig. 4.9	fig. 4.8
inferred velocity	–	distinct artefacts	distinct artefacts
velocity gradient	fig. 4.2	fig. 4.5	fig. 4.3
momentum flux	distinct artefacts	unusable	unusable
velocity gradient	NULL	fig. 4.7	fig. 4.6
inferred velocity	–	realistic	realistic

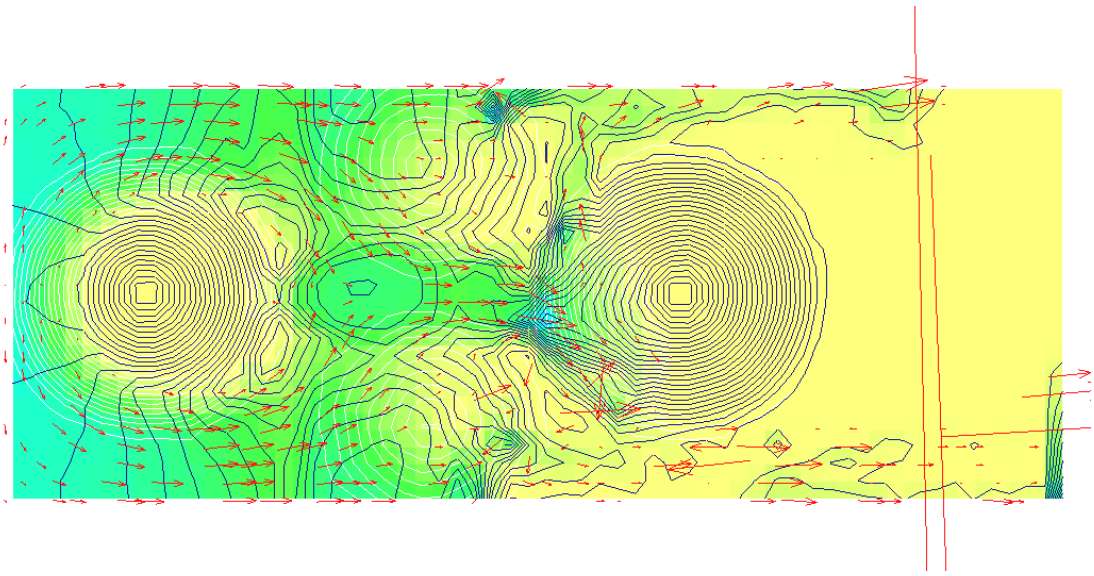

Figure 4.2: Result without special treatment for partially dry cells.
using: C, VG, MF
A minimum depth method is applied in flux calculation. Gradients in cells are found for velocity rather than momentum.

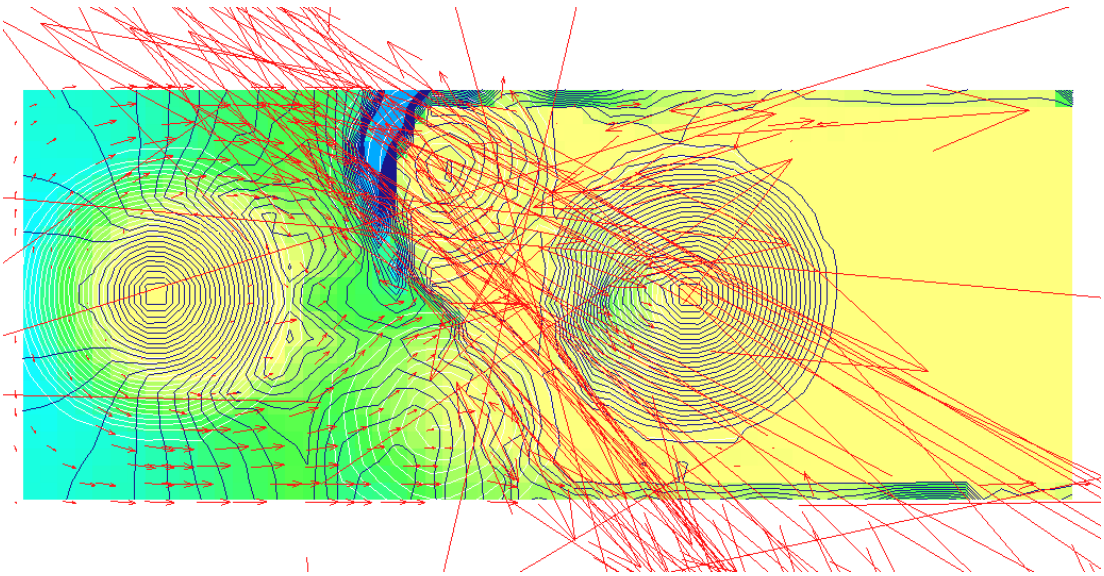

Figure 4.3: The four mound test case. Status after 8 seconds.
using: PL-VFR, VG, MF
Simulation with the piecewise level bed profile. Gradients in cells are found for velocity. Momentum flux and source terms are applied to partially dry cells in each time step.

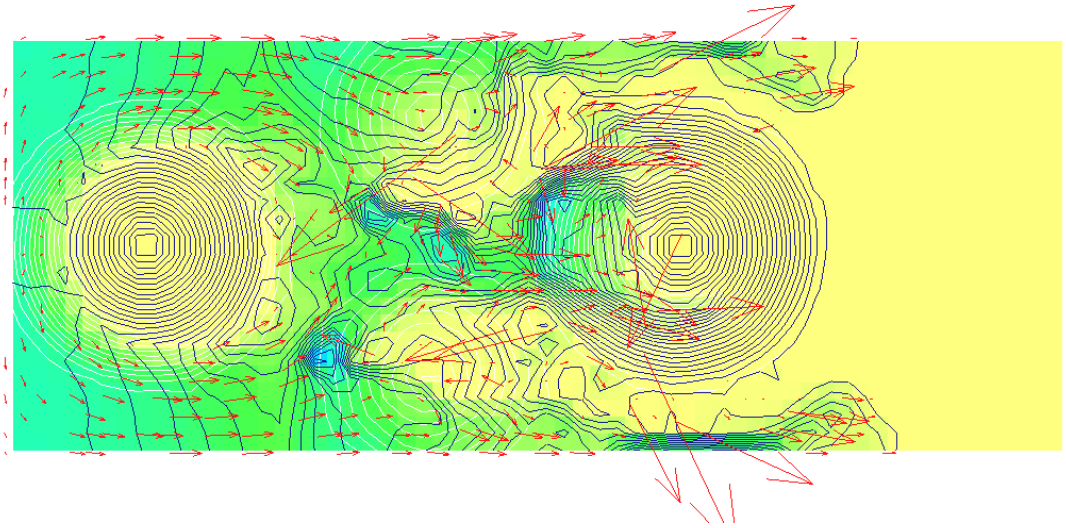

Figure 4.4: The four mound test case. Status after 8 seconds.
using: Q-VFR, MG, MF
Simulation with the double triangle profile. Gradients in cells are found for momentum. Momentum flux and source terms are applied to partially dry cells in each time step.

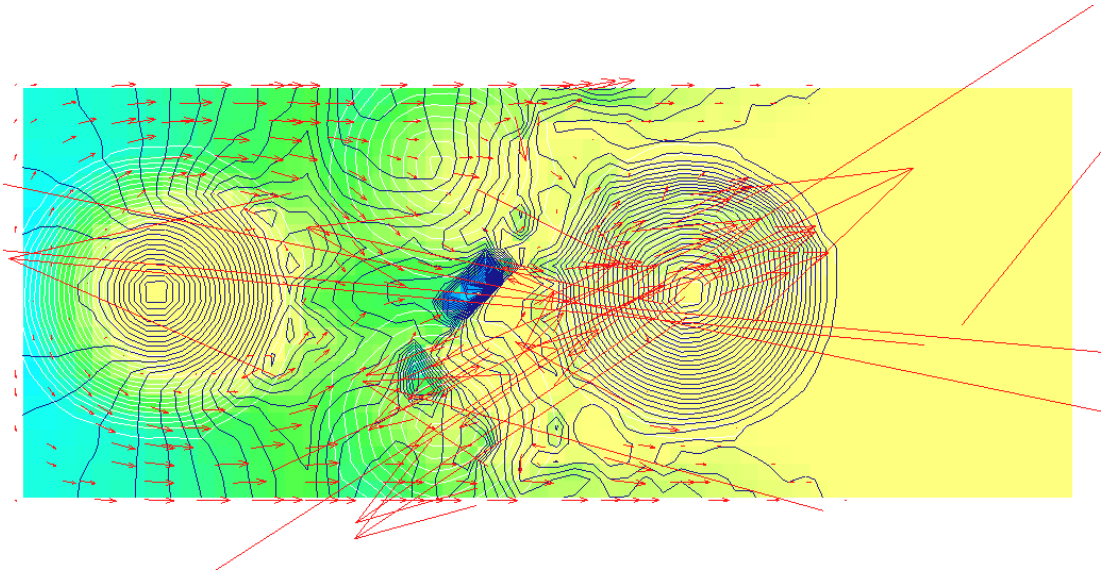

Figure 4.5: The four mound test case. Status after 8 seconds.
using: Q-VFR, VG, MF
Simulation with the double triangle profile. Gradients in cells are found for velocity. Momentum flux and source terms are applied to partially dry cells in each time step.

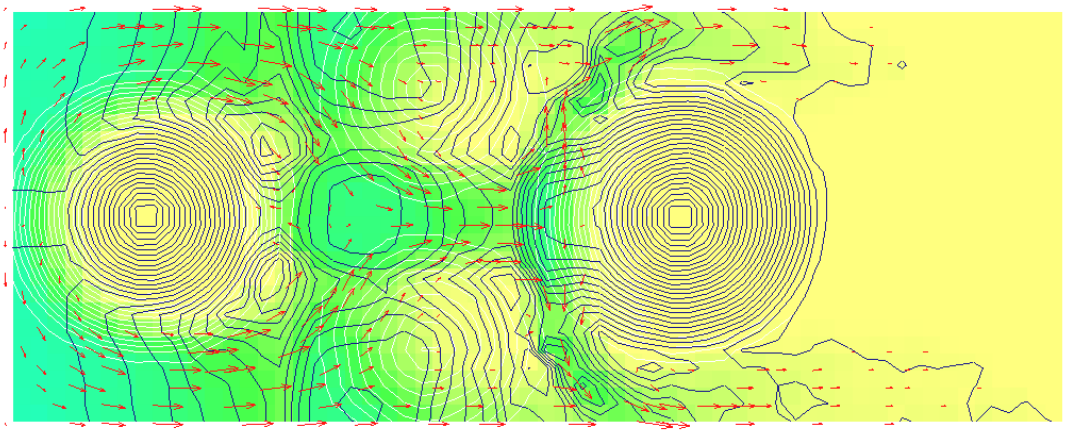

Figure 4.6: The four mound test case. Status after 8 seconds.
using: PL-VFR, VG, IV
Simulation with the piecewise level bed profile. Gradients in cells are found for velocity. Velocity in partially dry cells are interpolated using the values in neighbouring cells.

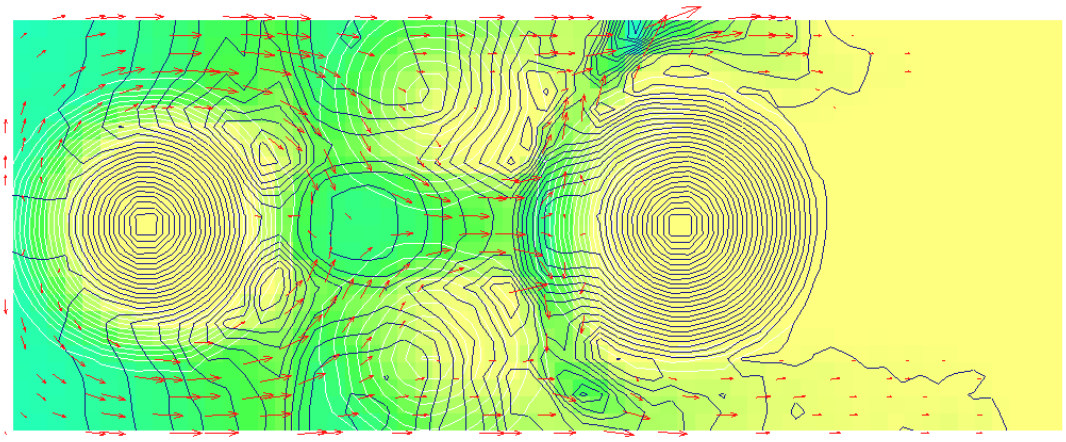

Figure 4.7: The four mound test case. Status after 8 seconds.
using: Q-VFR, VG, IV
Simulation with the double triangle profile. Gradients in cells are found for velocity. Velocity in partially dry cells are interpolated using the values in neighbouring cells.

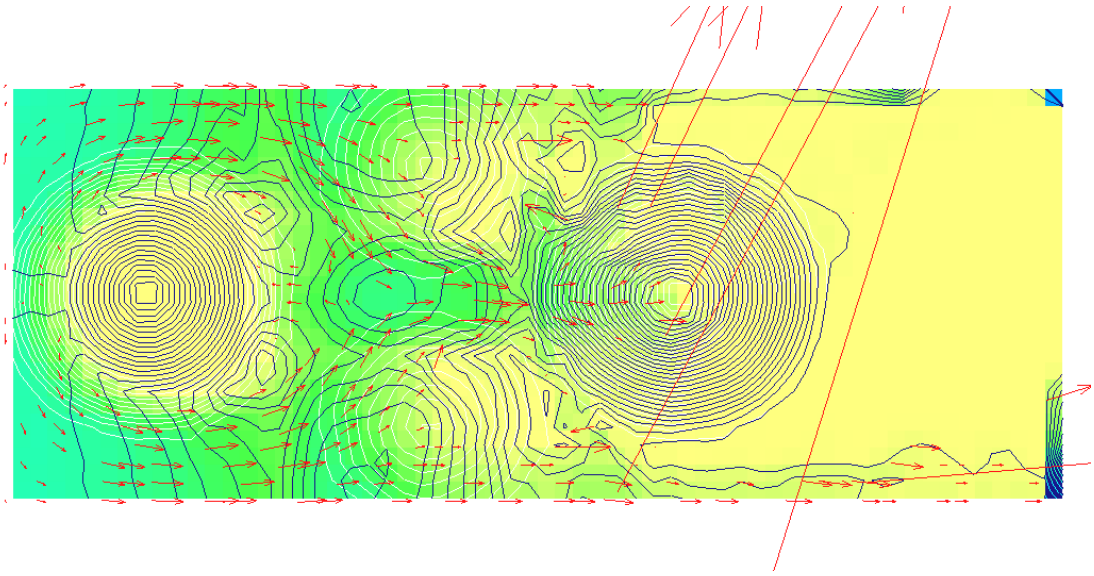

Figure 4.8: The four mound test case. Status after 8 seconds.
using: PL-VFR, MG, IV
Simulation with the piecewise level bed profile. Gradients in cells are found for momentum. Velocity in partially dry cells are interpolated using the values in neighbouring cells.

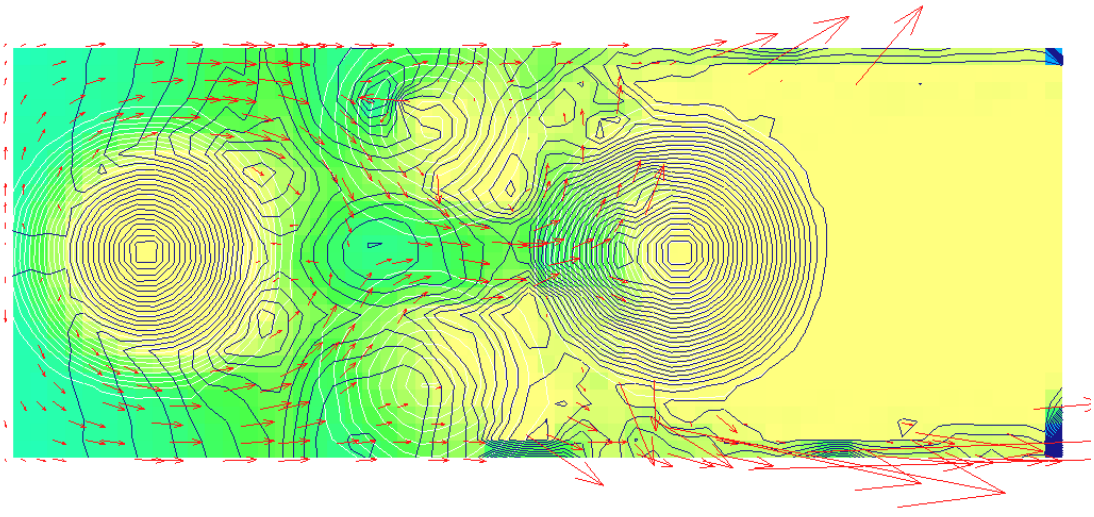

Figure 4.9: The four mound test case. Status after 8 seconds.
using: Q-VFR, MG, IV
Simulation with the double triangle profile. Gradients in cells are found for momentum. Velocity in partially dry cells are interpolated using the values in neighbouring cells.

4.2 Isolated Obstacle

This case attempts to reproduce a physical experiment undertaken at the Civil Engineering Laboratory of the Université catholique de Louvain (Soares-Frazao and Zech, 2007). This was designed as part of the IMPACT (Investigation of Extreme Flood Processes and Uncertainty) workshop as a benchmark test. The participants have since presented their results (Aureli *et al.*, 2003; Capart, 2003; Mignot and Paquier, 2003a; Noel *et al.*, 2003; Petaccia and Savi, 2003). In these the obstacle was either represented as a patch of raised ground or accommodated using a conforming mesh.

A rectangular block 0.4m by 0.8m was placed at an angle in a 3.60m wide channel in water at rest at 0.02m at the deepest. The channel bed was horizontal except for a slope at each margin of the channel up towards the side wall. Upstream was a storage tank 3.60m wide by 6.9m long containing water at 0.40m deep. A channel section 1.0m long by 0.8m wide connects the reservoir to the centre of the channel, initially blocked by a gate. Downstream the channel extended roughly 25m beyond the block which was far enough for backflow not to affect the area of interest. The block was placed, as shown in 4.10, with the nearest corner being 1.75m ahead of the centre of the gate and the longest side at an angle of 64° to the centre line.

Six sets of depth and velocity gauges were placed at the points given in table 4.2. Five of these surrounded the obstacle. The sixth depth gauge was placed within the storage basin. In addition, polystyrene tracer particles were placed in the reservoir, and a digital camera set up, so that analysis of their movement could give an estimate of surface velocities.

In the computer simulation the cells are elongated in the main direction of flow, the dimension which dominates the constraint on the time step. Four meshes are applied; #0 is $2.5cm \times 5cm$, #1 is $5cm \times 10cm$, #2 is $10cm \times 20cm$ and #3 is

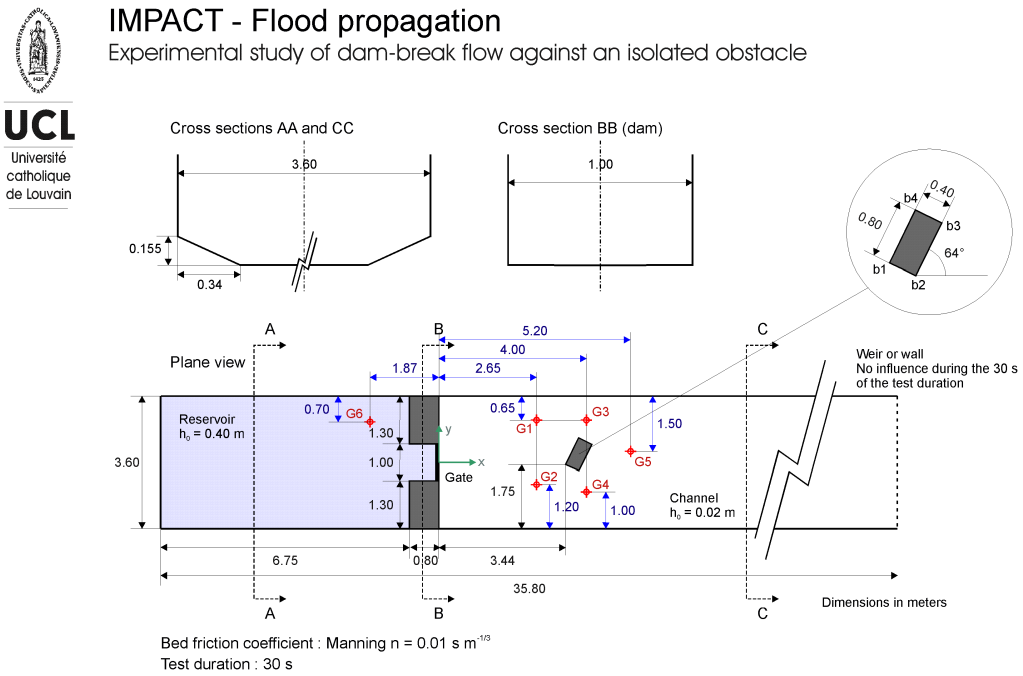

Figure 4.10: Plan of the flood baisin used in the isolated obstacle experiment.

Table 4.2: Isolated obstacle experiment. Location of the gauges.

Gauge	x (m)	y(m)
G1	2.65	1.15
G2	2.65	-0.60
G3	4.00	1.15
G4	4.00	-0.80
G5	5.20	0.30
G6	-1.87	1.10

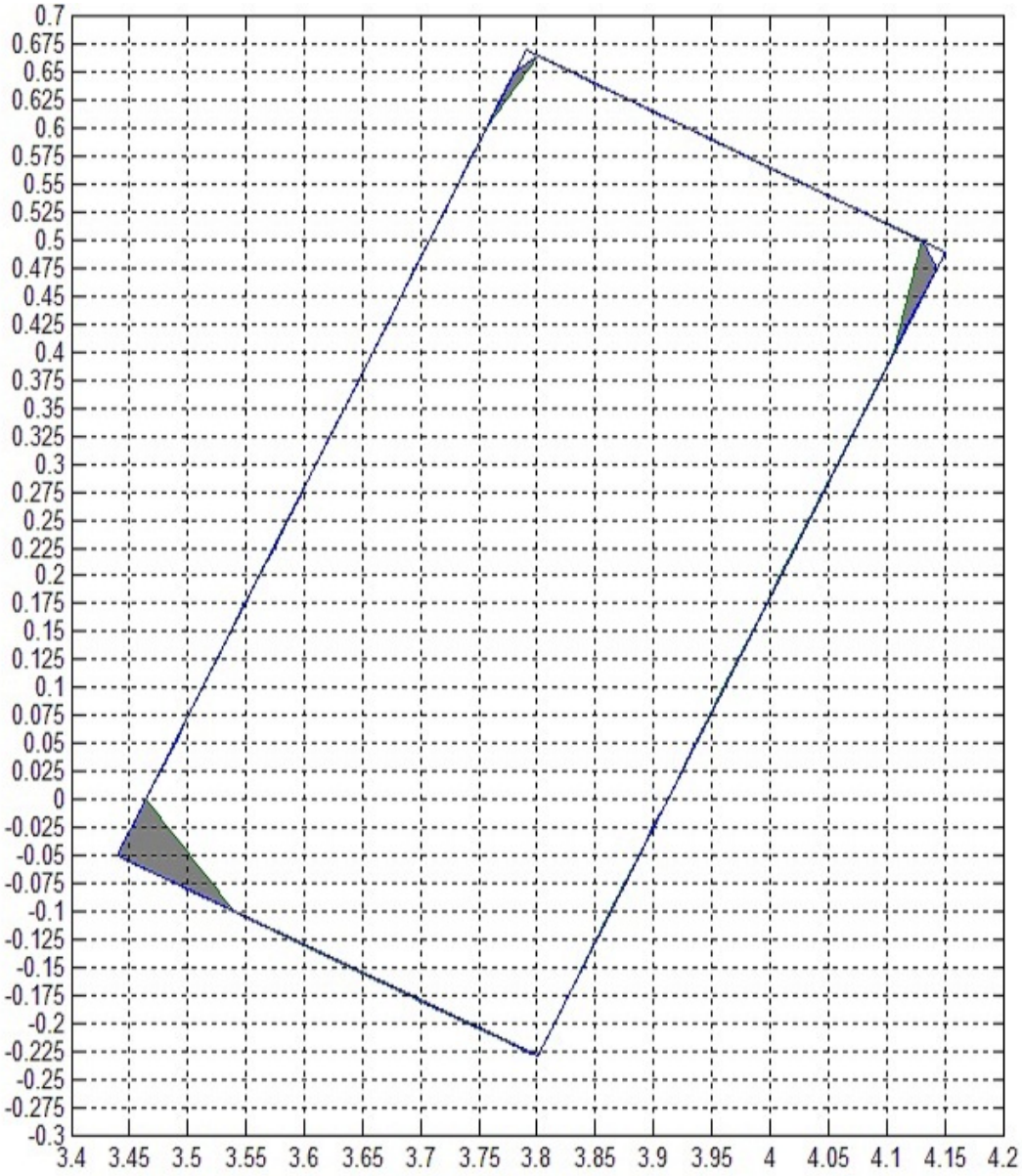

Figure 4.11: Outline of the obstacle relative to the cell grid. The grey region shows the change in outline between the finest and coarsest meshes.

$20cm \times 40cm$. With cut-cells some details of the shape are lost at the corners, particularly on the coarser mesh size *figure* (4.11). The greatest loss of definition is on the facing the oncoming flow. If it had been at either of the outer corners it might have been more significant. The piecewise level VFR profile was used for partially dry cells.

4.2.1 Grid Convergence

Richardson extrapolation (Roache (1997)) was applied in order to evaluate the effect of mesh refinement on the accuracy of the solution. The average depth at each gauge over the duration of the simulation. This is suitable for verification as it avoids selection bias, since it not easy to determine convergence by eye. It also evades problems caused by rounding errors, which are notable due to the way this data set was recorded. The order of accuracy can be estimated from three sequential refinements according to equation 4.1. This is nonstandard in that the errors are normally expected to shrink monotonically with mesh resolution. The norm is necessary here because this does not happen. This gives two estimates for each gauge (Table 4.3).

$$O(\epsilon) = \frac{1}{\ln 2} \ln \left| \frac{f_3 - f_2}{f_2 - f_1} \right| \tag{4.1}$$

The number of negative values indicating divergence matches the number of positive values. Further, for each gauge the two converge measures contradict each other. This clearly shows that the simulation has not yet begun to converge. There are strong characteristics which are still emerging on the most refined grid.

4.2.2 Propagation of the Flood Wave

Figures 4.12,4.13 and 4.14 are taken from the computer simulation. They show the channel 1,3 and 5 seconds after the gate was lifted. The flood reaches the

gauge	scale 3	scale 2	scale 1	scale 0	$\frac{f_3-f_2}{f_2-f_1}$	O_ϵ	$\frac{f_2-f_1}{f_1-f_0}$	O_ϵ
1	0.1037	0.1012	0.1023	0.0988	-2.185	1.128	-0.333	-1.588
2	0.0922	0.0771	0.0735	0.0625	4.194	2.068	0.330	-1.598
3	0.0903	0.0919	0.0940	0.0953	0.721	-0.473	1.727	0.789
4	0.0902	0.0911	0.0905	0.0926	-1.421	0.507	-0.288	-1.795
5	0.0694	0.0674	0.0676	0.0671	-10.067	3.332	-0.425	-1.234
6	0.2755	0.2789	0.2792	0.2915	12.932	3.693	0.021	-5.548

Table 4.3: Time averaged water depths and the derived convergence parameters.

obstacle within 3 seconds. A hydraulic jump has already developed upstream of the obstacle. Backflow from the channel walls is also evident. There is no problem evident from wetting and drying on the side slopes. At 5 seconds the hydraulic jump is more developed. It is more pronounced against the narrower (left hand) gap. Flow from both sides recombine to form a standing wave downstream of the block.

4.2.3 Velocity fields

Figures 4.15(a),4.15(b),4.16(a),4.16(b) show the measured and computed flow fields after 5 and 10 seconds. These seem reasonably close. The propagation of backflow between these two times is evident as the patch of low velocity arrows. Where gauge 5 is located, immediately behind the obstacle is the confluence of two streams seperated by the obstacle.

4.2.4 Shock Wave

Gauges 1 (figures 4.17,4.18) and 2 (figures 4.19,4.20) are located upstream of the obstacle and consequently subject to backflow. The hydraulic jump is particularly noticeable at gauge 2 as this is propagated through this point roughly halfway through the experiment. The calculations all reproduce this, though naturally the time of transition is too sensitive to capture precisely.

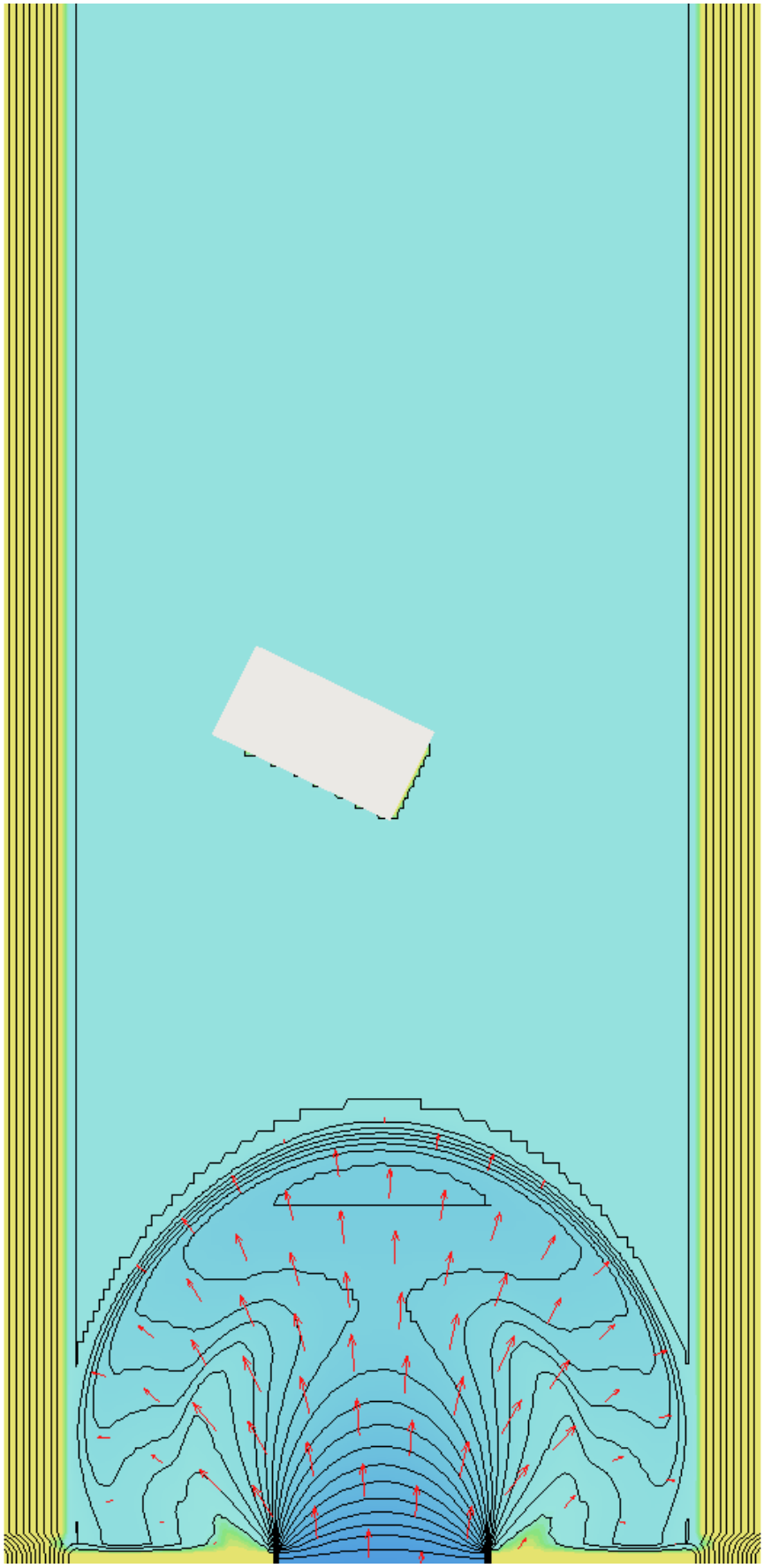

Figure 4.12: Region around the obstacle after 1 second. Wetted areas are blue deepening with depth. Dry areas are yellow. Contours show surface level at 0.01 meter intervals. Velocity vectors (in red) are to scale.

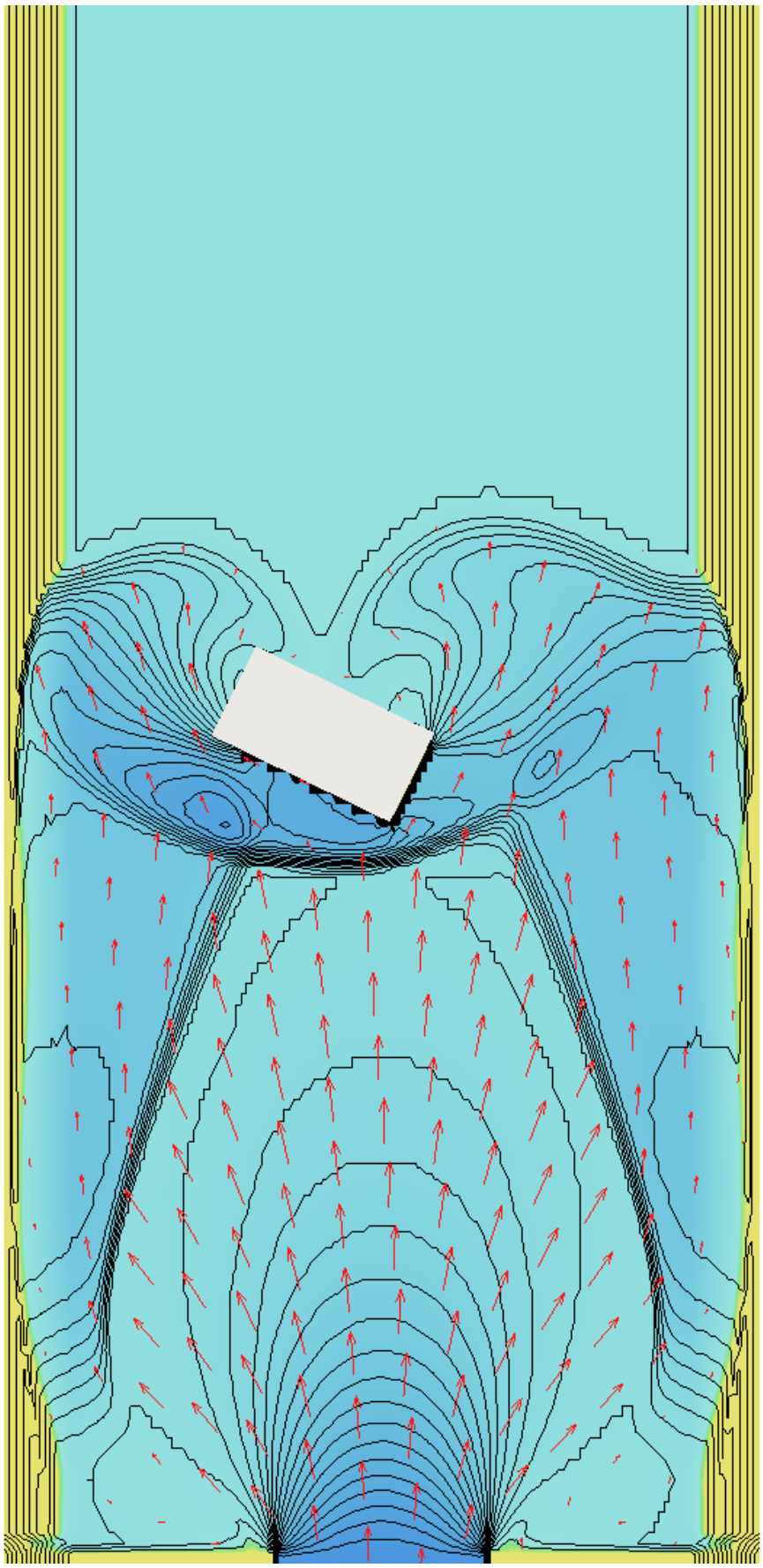

Figure 4.13: Region around the obstacle after 3 seconds. Wetted areas are blue deepening with depth. Dry areas are yellow. Contours show surface level at 0.01 meter intervals. Velocity vectors (in red) are to scale.

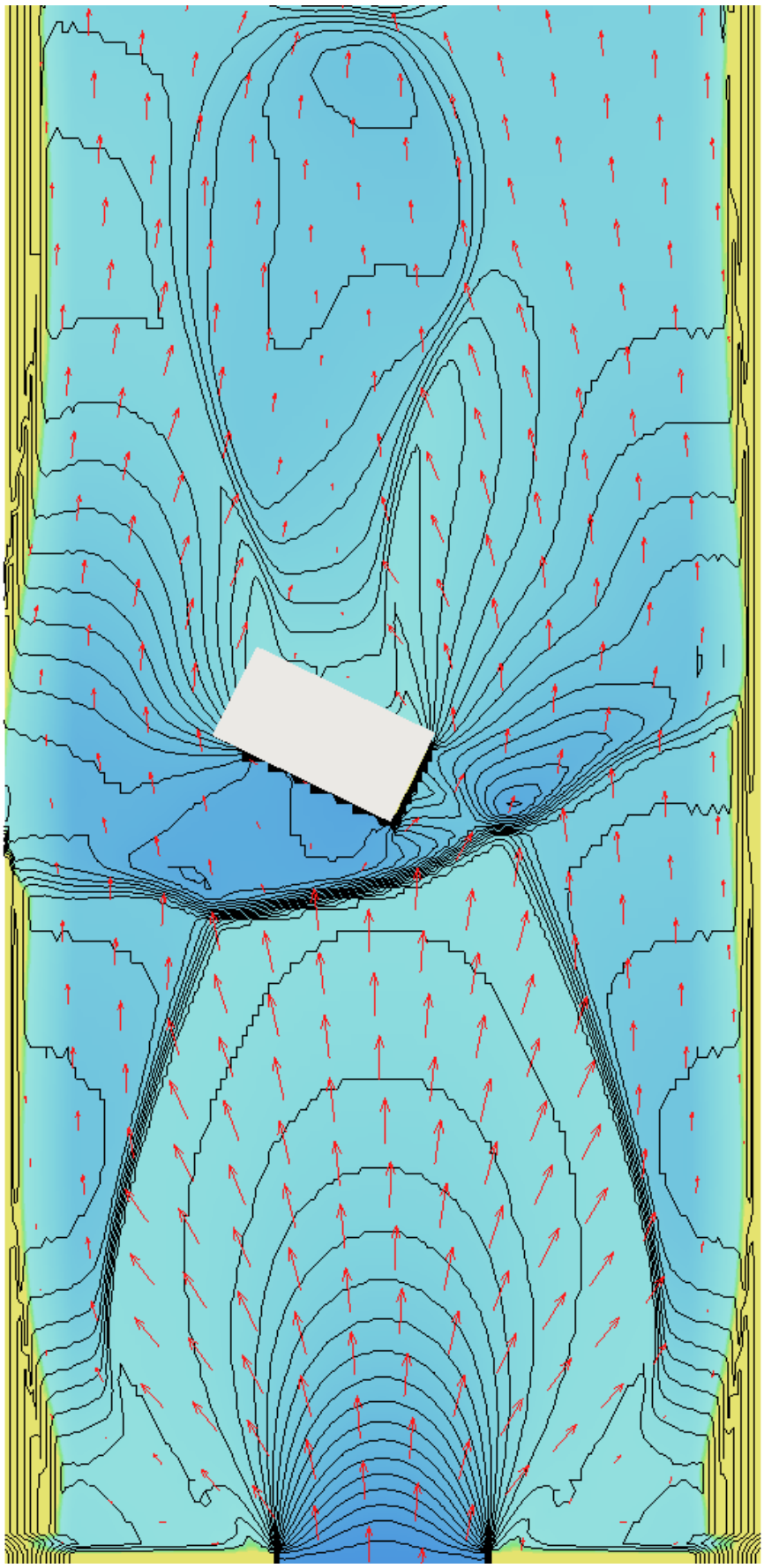

Figure 4.14: Region around the obstacle after 5 seconds. Wetted areas are blue deepening with depth. Dry areas are yellow. Contours show surface level at 0.01 meter intervals. Velocity vectors (in red) are to scale.

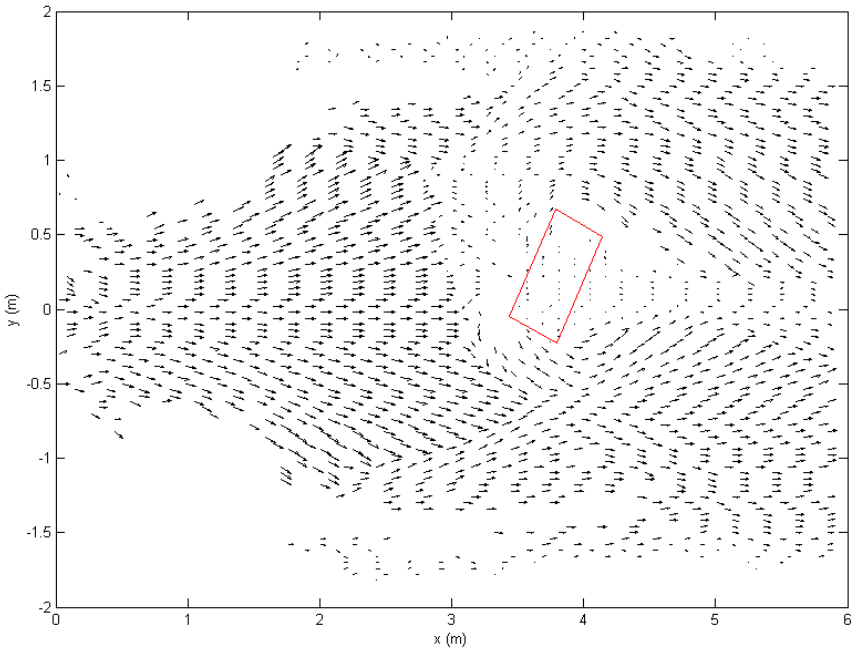

(a) physical model

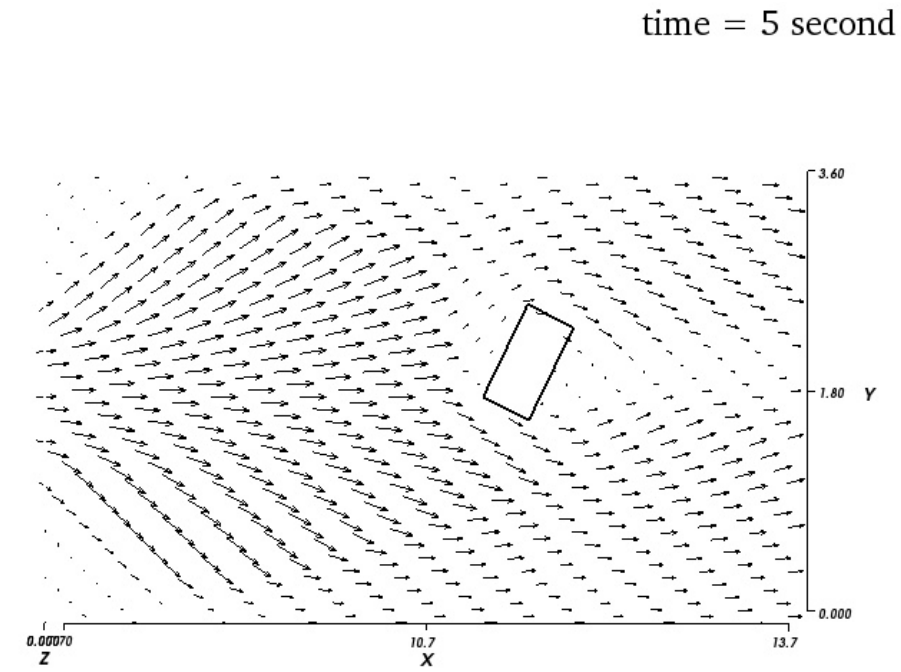

(b) computer model

Figure 4.15: Isolated obstacle experiment. Measured velocity field at t = 5 seconds.

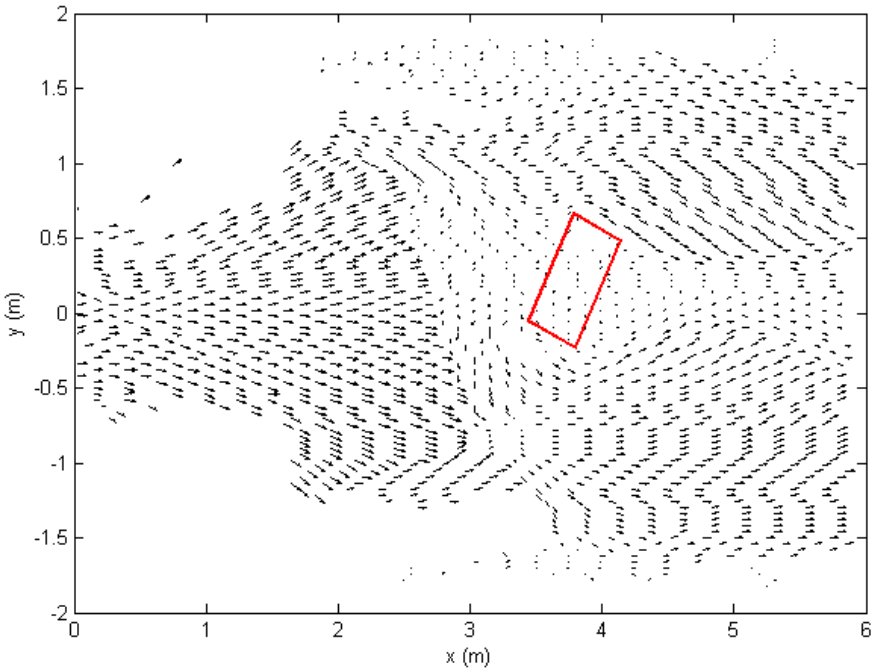

(a) physical model

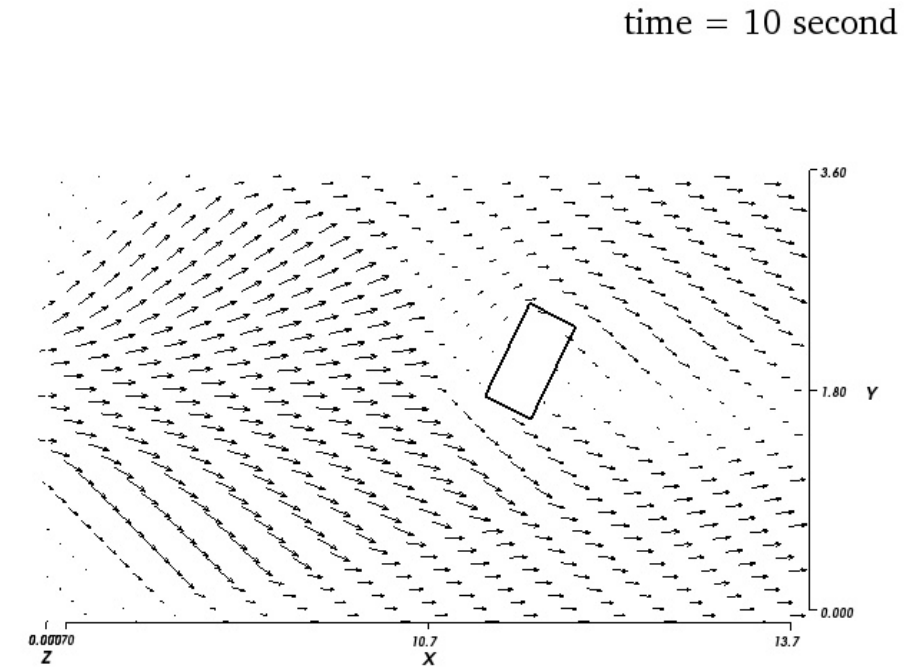

(b) computer model

Figure 4.16: Isolated obstacle experiment. Measured velocity field at t = 10 seconds.

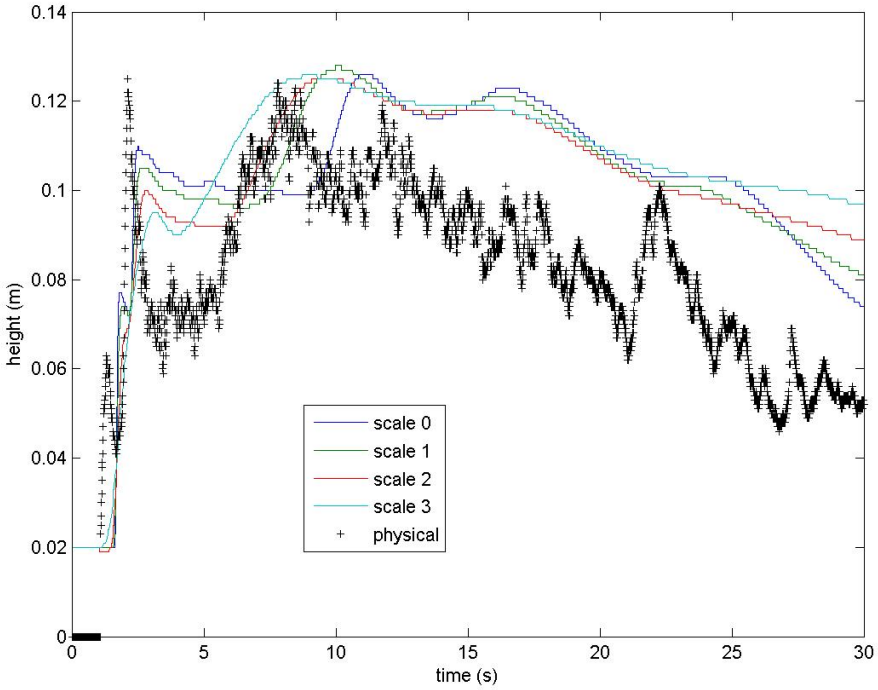

Figure 4.17: Isolated obstacle. Depths at gauge G1.

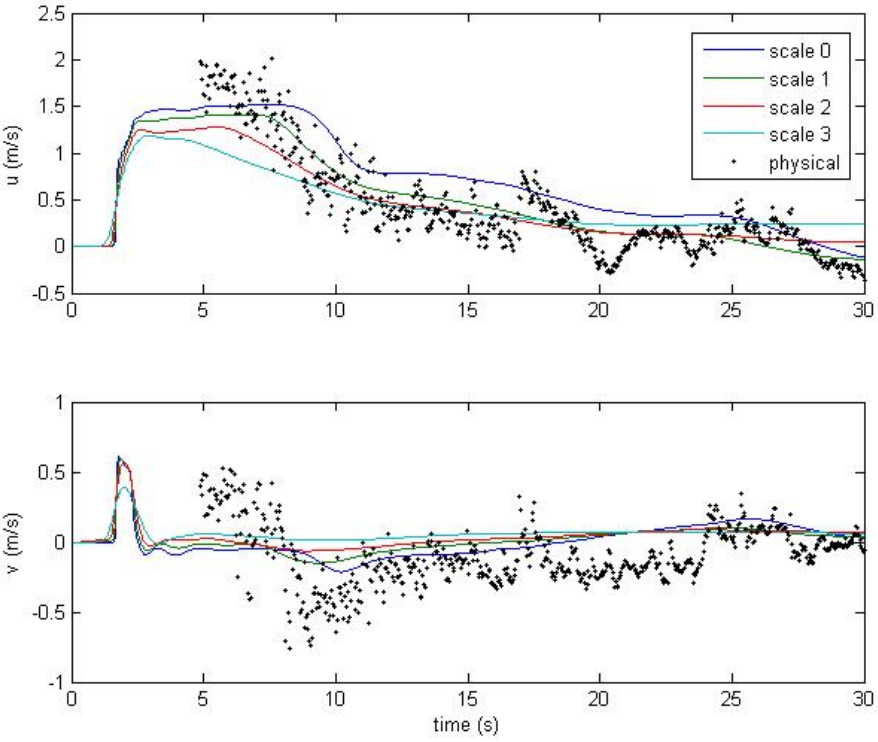

Figure 4.18: Isolated obstacle. Velocity at gauge G1.

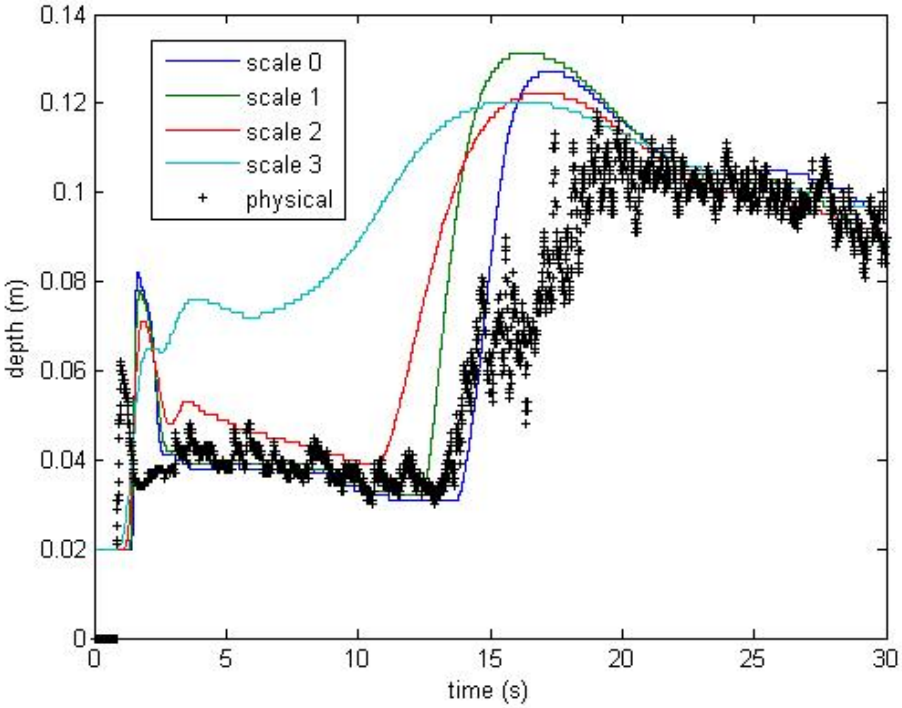

Figure 4.19: Isolated obstacle. Depths at gauge G2.

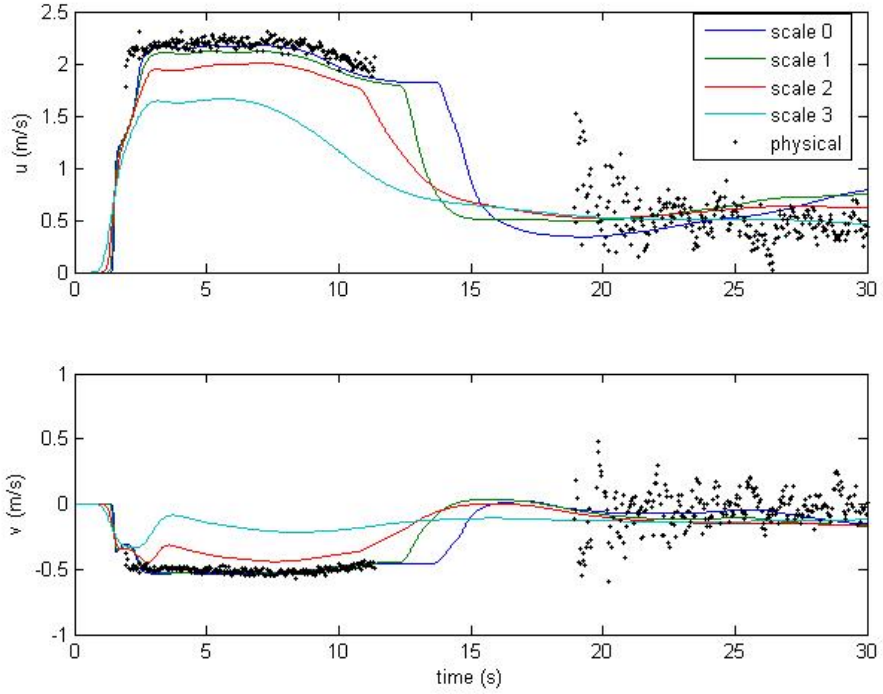

Figure 4.20: Isolated obstacle. Velocity at gauge G2.

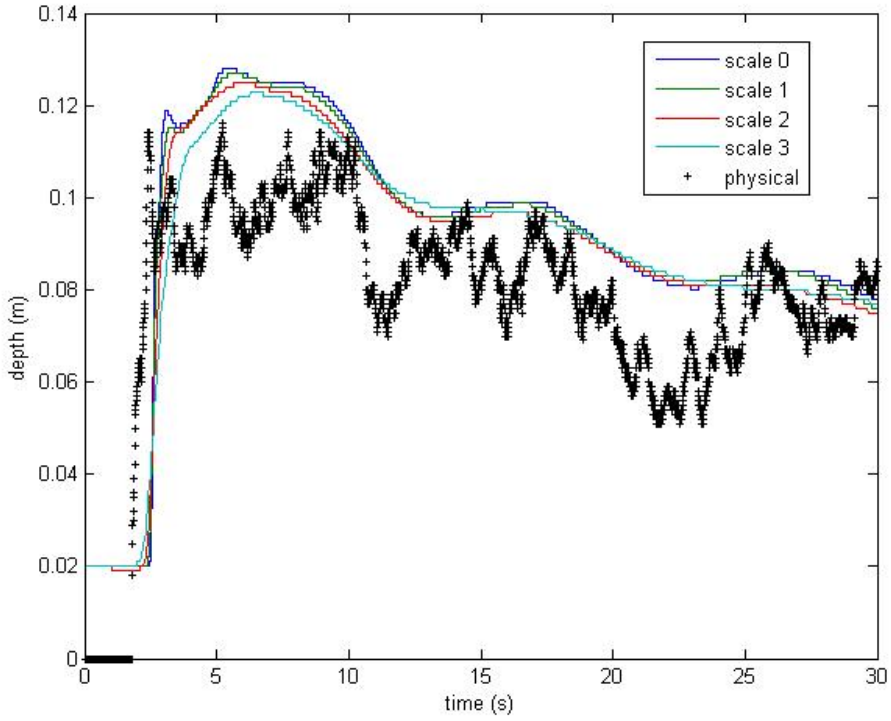

Figure 4.21: Isolated obstacle. Depths at gauge G3.

4.2.5 Critical points

Gauges 3 (figures 4.21,4.22) and 4 (figures 4.23,4.24) are located just downstream of the two most constricted part of the flow. The gauges are also at the lee side of the back flow where the water is accelerating under gravity. There is a second stream at each side of the channel caused by a reflection off the side wall. Each of these streams meets the backflow quite close to gauges 3 and 4. There is a video of the experiment accompanying the dataset on a DVD. This shows the peaks of the backflow and the reflected streams quite strongly because these are all white. The white colour quite clearly indicate vertical recirculation and air entrainment. This recirculation is visible in the lateral velocity components at both gauges for the physical model, whereas there is no trace of this in any of the simulations. Figures 4.13 and 4.14 show the reflected streams are well defined and that they are evolving in a smooth fashion. It is clear that there is turbulent flow present

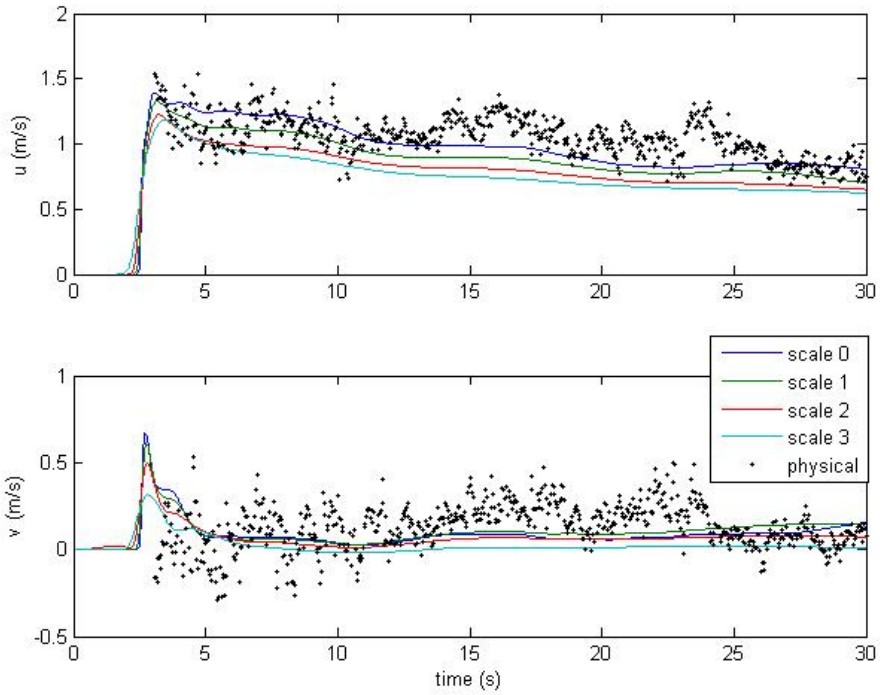

Figure 4.22: Isolated obstacle. Velocity at gauge G3.

in the physical experiment which the hydrostatic shallow water equations are not able to show.

4.2.6 Downstream

Gauge 5 (figures 4.25, 4.26) is located between two competing streams from either side of the obstacle. The experimental results show a strong oscillatory pattern which is likely to be a result of these two streams interacting. This effect is completely absent in the computed results. This is likely due to turbulence, air entrainment or some combination of the two. The presence of hydraulic jumps will introduce some non-hydrostatic effects into the system. (Soares-Frazao and Zech, 2007) describe these as wake eddies.

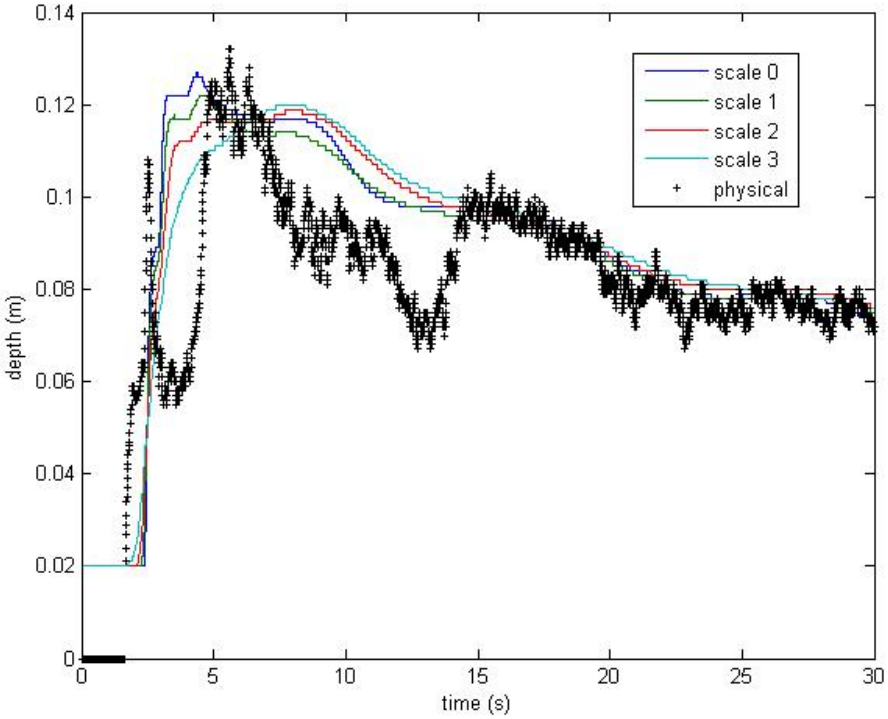

Figure 4.23: Isolated obstacle. Depths at gauge G4.

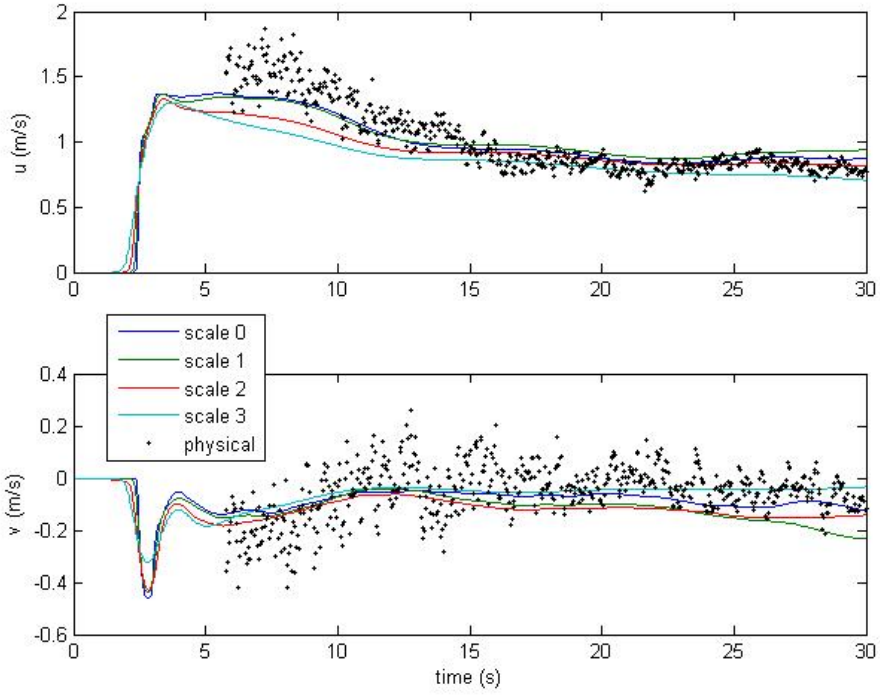

Figure 4.24: Isolated obstacle. Velocity at gauge G4.

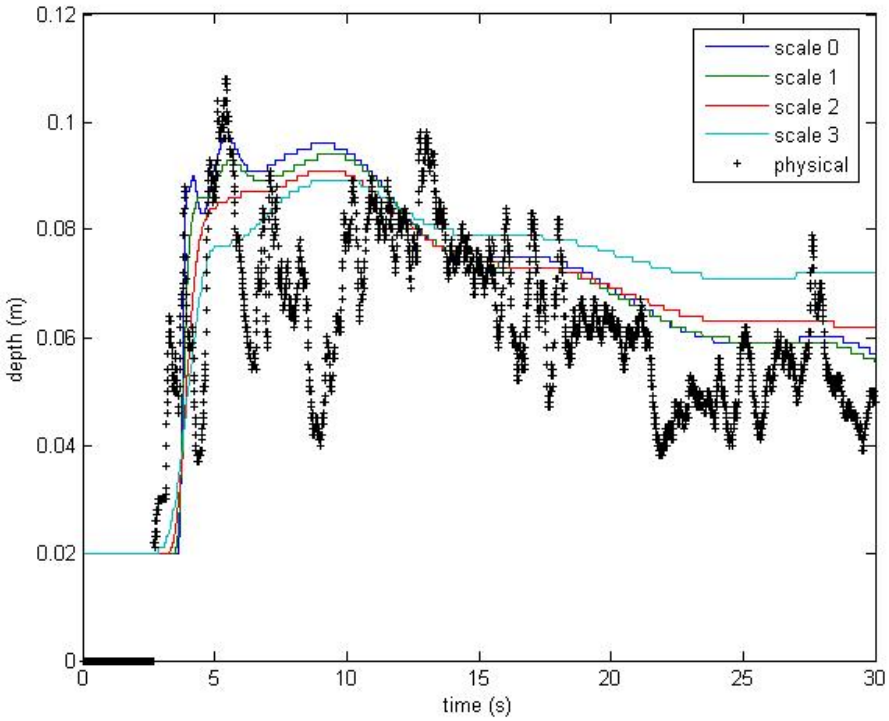

Figure 4.25: Isolated obstacle. Depths at gauge G5.

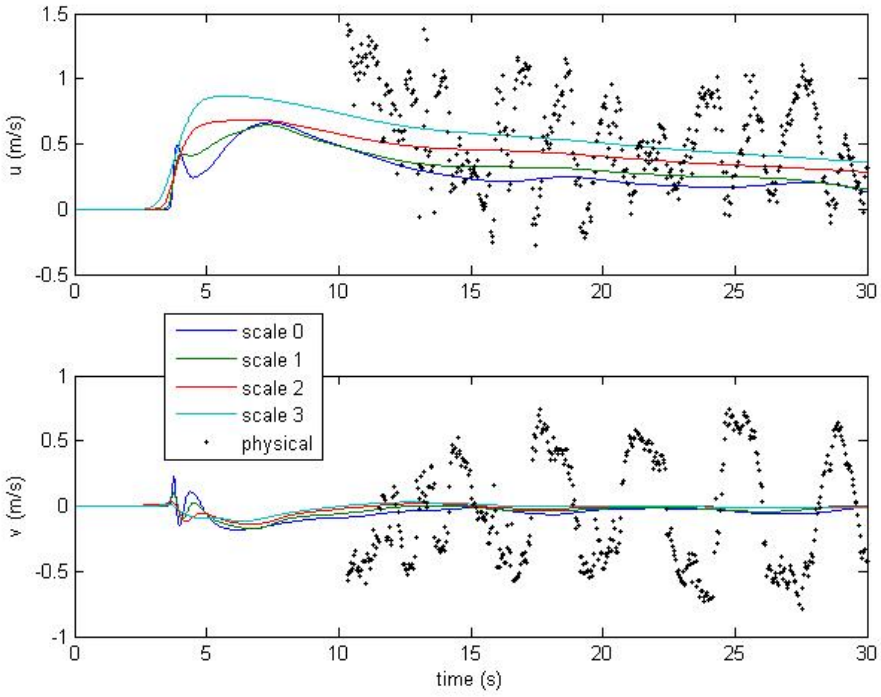

Figure 4.26: Isolated obstacle. Velocity at gauge G5.

4.2.7 Conclusions

Grid convergence showed that the results are strongly dependent on mesh resolution. This behaviour requires caution as it indicates that calibration must be made specific to the mesh resolution. Nonetheless the computations reproduced the general pattern of flow. The turbulant behaviour of the physical experiment was not present in the simulation. While further mesh refinement may improve the accuracy of the simulations it is not possible to reproduce these aspects of the experiment, by solving the shallow water equations.

4.3 Toce River Basin

The Toce river basin experiment was carried out at the Université catholique de Louvain as part of the IMPACT project mentioned above (section 4.2). Results from participants in this project are available (Alcrudo, 2003; Mignot and Paquier, 2003b; Noel *et al.*, 2003). These represented the blocks variously as solid obstacles, raised topography and patches of roughness.

The Civil Engineering Laboratory staged a set of experiments simulating flood flow through an urban district. The bed replicates the topography of the Toce river basin. The Toce river itself is not present in the experiments reproduced here. Two parallel concrete walls guide the water through an arrangement of cuboid blocks downstream. These represent a built up area. Two layouts were used, regular lattice with unblocked lanes in both directions, and a staggered layout. The water enters upstream end from an open rectangular tank. Gauges record water level and velocity in and near the upstream boundary and among the blocks. Three sets of experiments were carried out on each with different peak flows. The simulations presented here reproduce the median set of discharges.

4.3.1 Aligned Grid

Figure 4.27 shows the topography and arrangement of blocks used in the experiment. Figure 4.28 shows the location of depth gauges. Note that the contours in the latter figure indicate the presence of a channel that was filled in for the physical experiment. This simulations used a mesh size of 540 by 268 cells at 0.0125m to a cell. The solid obstacles were placed using Cartesian cut cells. The grid scale is small compared with block sizes of 0.15m square, and seperations of 0.20m. Although the inflow boundary was placed upstream of its real location a reasonable approximation to the flows was still achieved.

A misalignment in the direction of flow is evident in figures 4.29, 4.30 and 4.31.

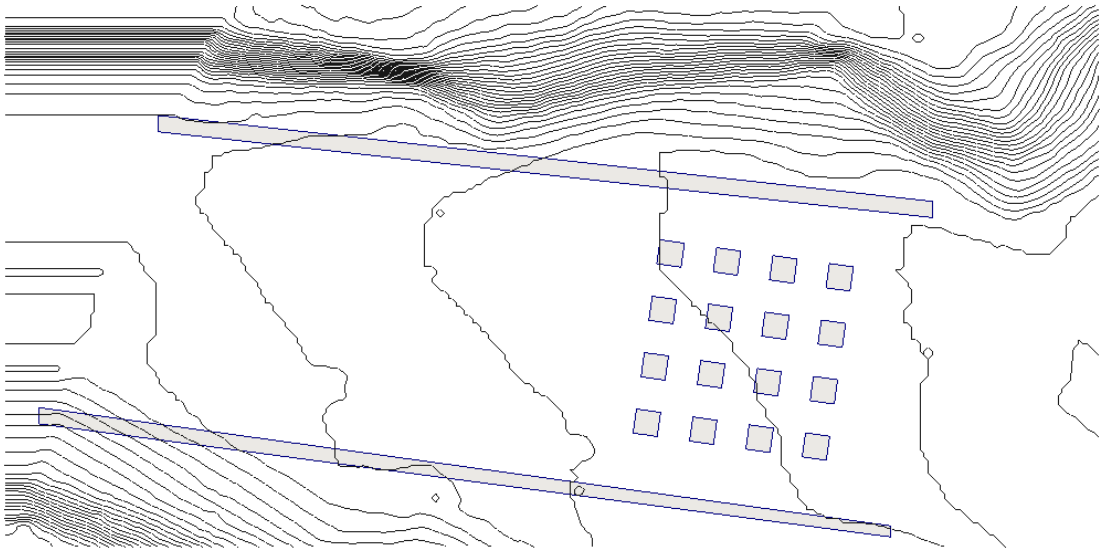

Figure 4.27: Toce basin urban flash-flood experiment with aligned blocks. Basin topography is described by contours at 0.02m intervals. The blocks and side walls are grey with a blue outline.

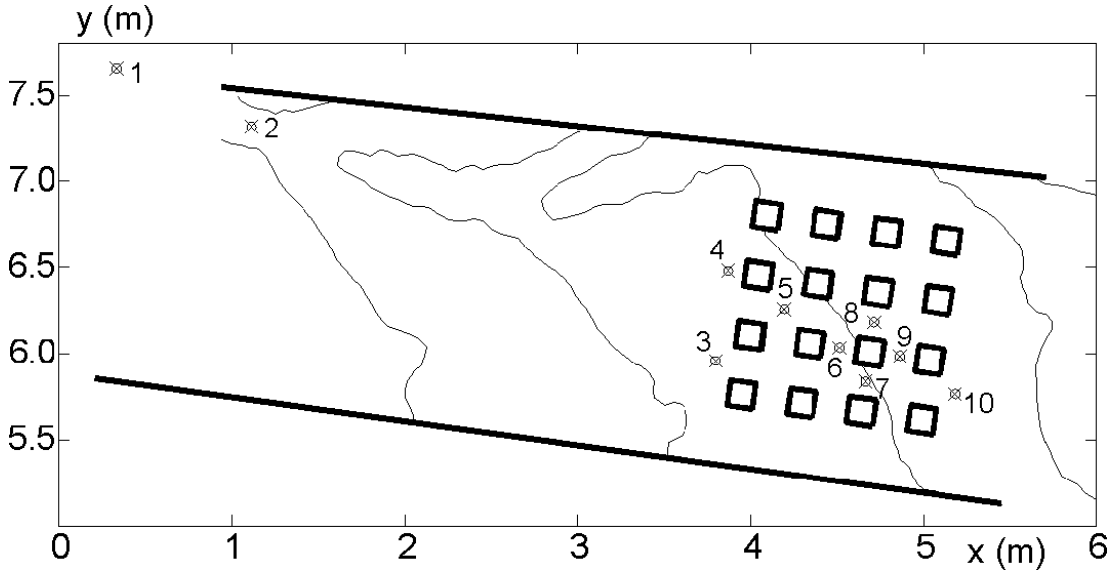

Figure 4.28: Toce basin urban flash-flood experiment with aligned blocks, showing the location of the depth gauges relative to the obstacles. Note the topography here is shown with the river channel. This feature is absent from the experiments reproduced here.

The two upstream gauges 4.32(a) and 4.32(b) illustrate this dramatically, with the levels transposed between the two. The standing wave arising from the interaction with the side wall is notable. This wave expands to reach to opposite wall so close to the upstream side of the array of obstacles. After 10 seconds the water has reached two of the upstream blocks on the left. Backflow rapidly develops and after 12 seconds is uniform along roughly 3/4 of the width channel.

The gauge readings for depth are nearly all reproduced with little error. The one notable exception is gauge 5 which is overestimated. This may be due to the direction of flow being altered in the simulation, or due to anomalies in the cut-cell geometry. Depths at gauge 8 which is one block downstream in the same channel, shows no significant difference between simulation and experiment.

4.3.2 Staggered Grid

Figure 4.34 shows the arrangement of blocks. Figure 4.35 shows the location of gauges. Again the second figure does not represent the topography in this experiment. As before the direction of inflow was not matched. This simulation uses a mesh size of 135 by 67 cells at 0.05m to a cell. The solid obstacles were placed using Cartesian cut cells. The grid scale is large compared with block sizes of 0.15m square, and seperations of 0.20m. Although the inflow boundary was placed upstream of its real location a reasonable approximation to the flows was still achieved.

Figures 4.36,4.37,4.38 show that the progress of the flood wave is much the same as in the previous experiment. The backflow ahead of the blocks is less pronounced, and less uniform. This may be due to greater conveyance to the left. Backflow against the later rows of blocks is evident.

The level gauges (figures 4.3.3,4.3.3) show a very good agreement with the physical model at most points. Gauge 3 upstream of the blocks underpredicts

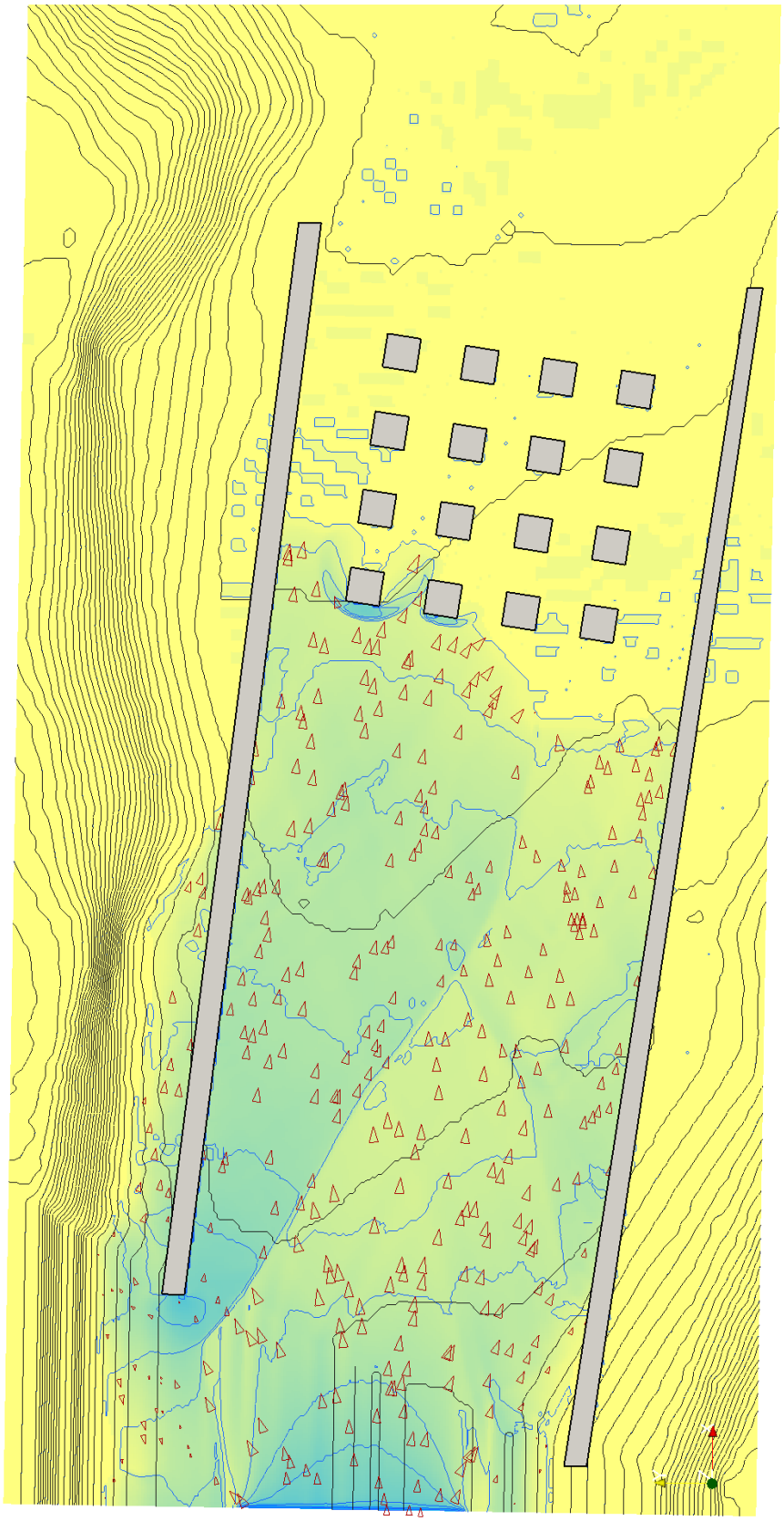

Figure 4.29: Computer simulation of the Toce basin urban flash-flood experiment. Terrain and water surface coordinates are marked at 0.2 meter intervals. Arrows have area proportional to discharge. Medium flow through aligned blocks. t = 10 seconds.

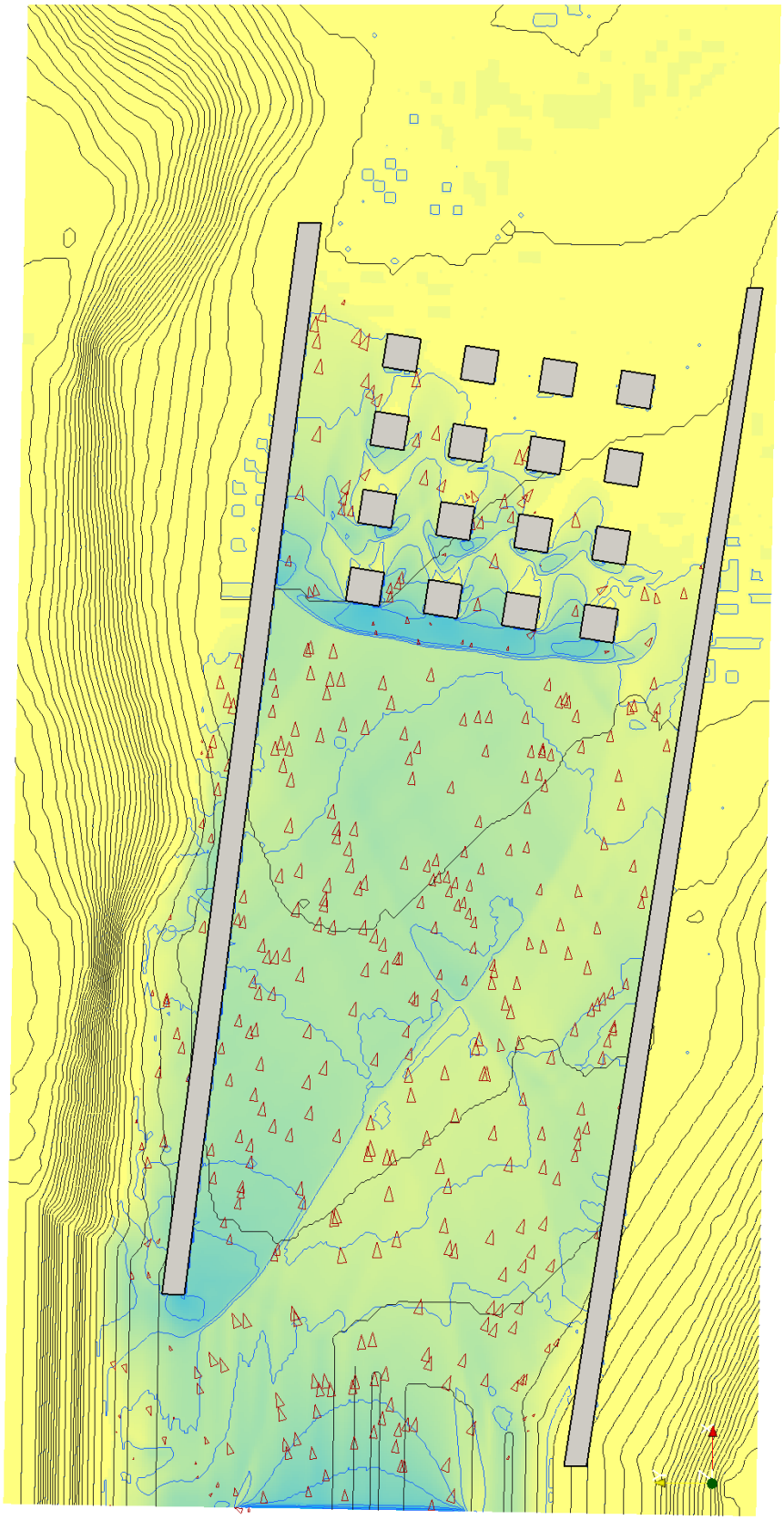

Figure 4.30: Computer simulation of the Toce basin urban flash-flood experiment. Terrain and water surface coordinates are marked at 0.2 meter intervals. Arrows have area proportional to discharge. Medium flow through aligned blocks. t = 11 seconds.

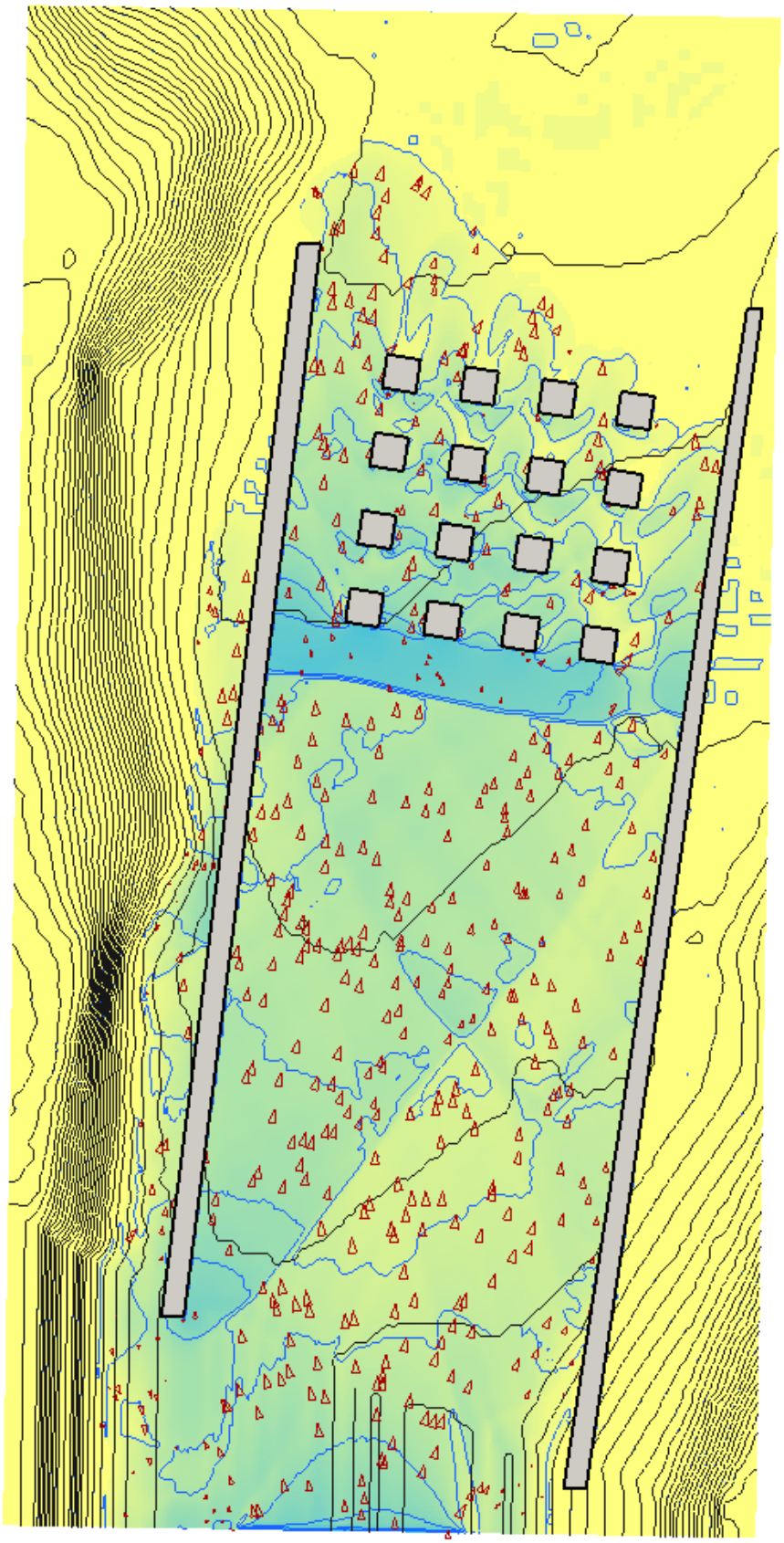

Figure 4.31: Computer simulation of the Toce basin urban flash-flood experiment. Terrain and water surface coordinates are marked at 0.2 meter intervals. Arrows have area proportional to discharge. Medium flow through aligned blocks. t = 12 seconds.

the level more than in the previous experiment. Levels at gauge 9 are similarly overpredicted. The readings at gauge 10 showed oscillations that could not be reproduced here. This is comparable to the results for the isolated obstacle test case (section 4.2). In both cases the gauge is at the confluence of competing streams.

4.3.3 Conclusions

In both experiments the boundary conditions did not match those of the physical experiment. In the original experiment the inflow tank was aligned so as to meet the upstream edges of the side walls. The computer simulation locates the inflow at the edge of the calculated domain which is larger than the physical bed and at an angle of 23.5 degrees. Nonetheless the predicted levels were accurate for most gauges. This is not too surprising as there was a great deal of homogeneity within the arrays of blocks. Gauges 6, 7, 8 and 9 gave similar readings in both the aligned block and staggered block experiments. The cut-cell methodology proved to be effective, even when it was used on a very rough grid compared to the size of the objects represented.

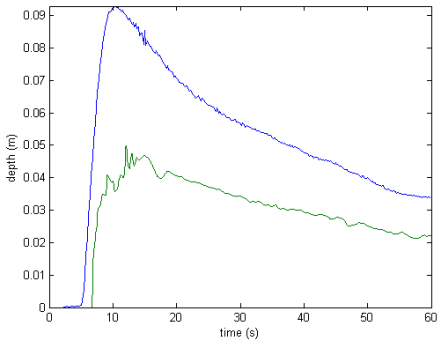

(a) Gauge 1

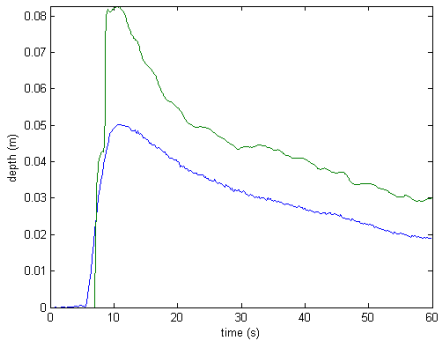

(b) Gauge 2

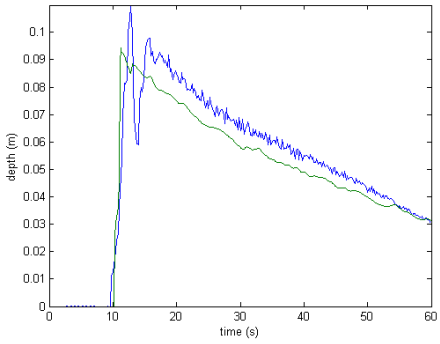

(c) Gauge 3

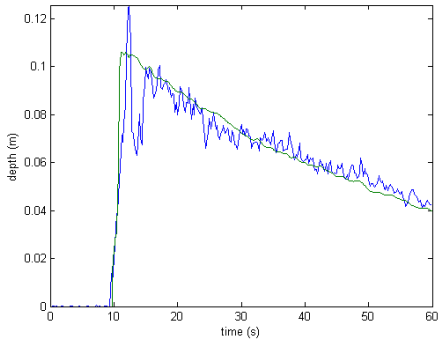

(d) Gauge 4

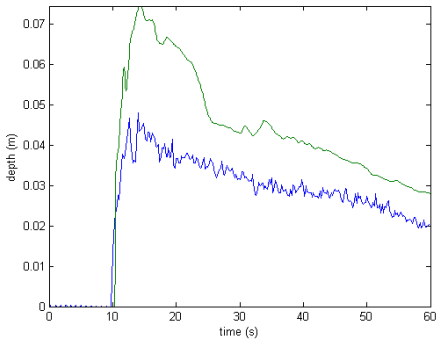

(e) Gauge 5

Figure 4.32: Toce basin urban flash flood experiment. Medium flow through aligned blocks. Comparison of measured (blue) and simulated (green) levels.

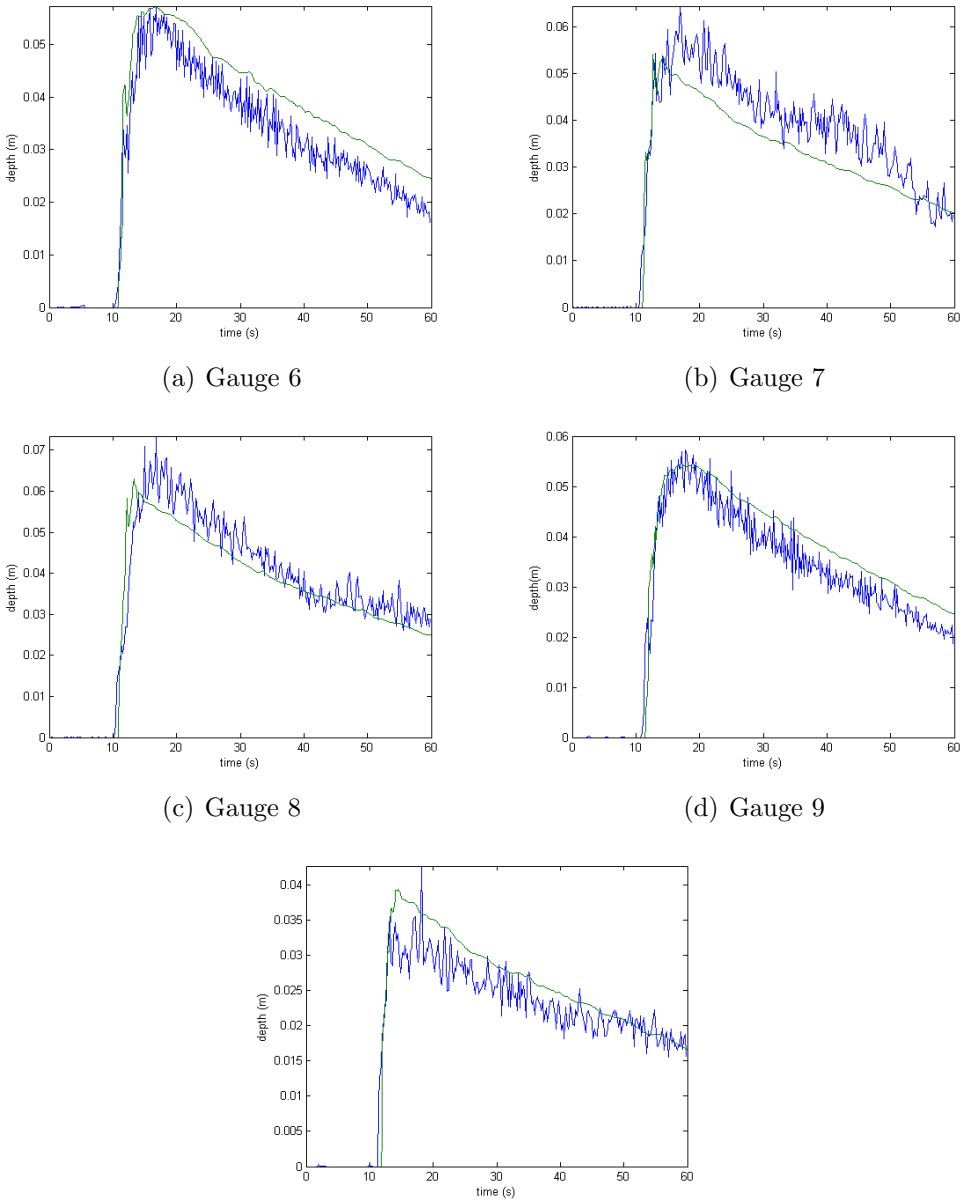

(a) Gauge 6

(b) Gauge 7

(c) Gauge 8

(d) Gauge 9

(e) Gauge 10

Figure 4.33: Toce basin urban flash flood experiment. Medium flow through aligned blocks. Comparison of measured (blue) and simulated (green) levels.

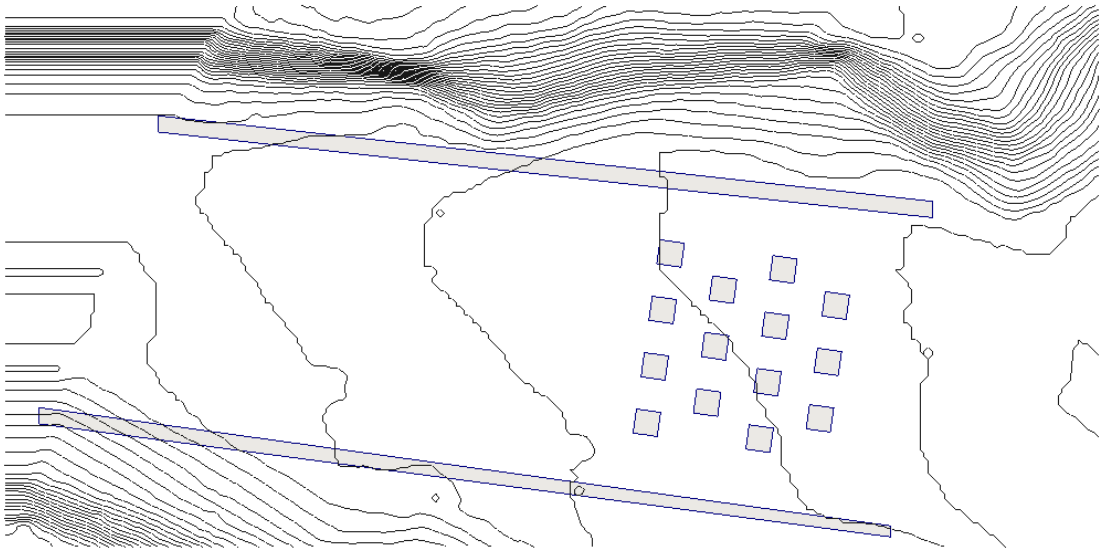

Figure 4.34: Toce basin urban flash-flood experiment with a staggered arrangement of blocks. Basin topography is described by contours at 0.02m intervals. The blocks and side walls are grey with a blue outline.

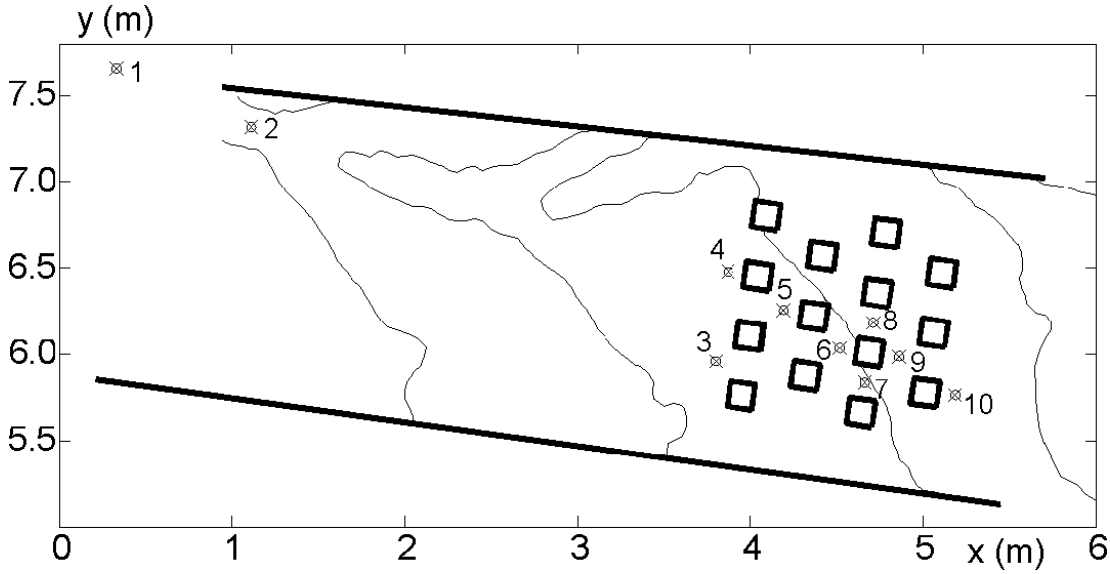

Figure 4.35: Toce basin urban flash-flood experiment with a staggered arrangement of blocks, showing the location of the depth gauges relative to the obstacles. Note the topography here is shown with the river channel. This feature is absent from the experiments reproduced here.

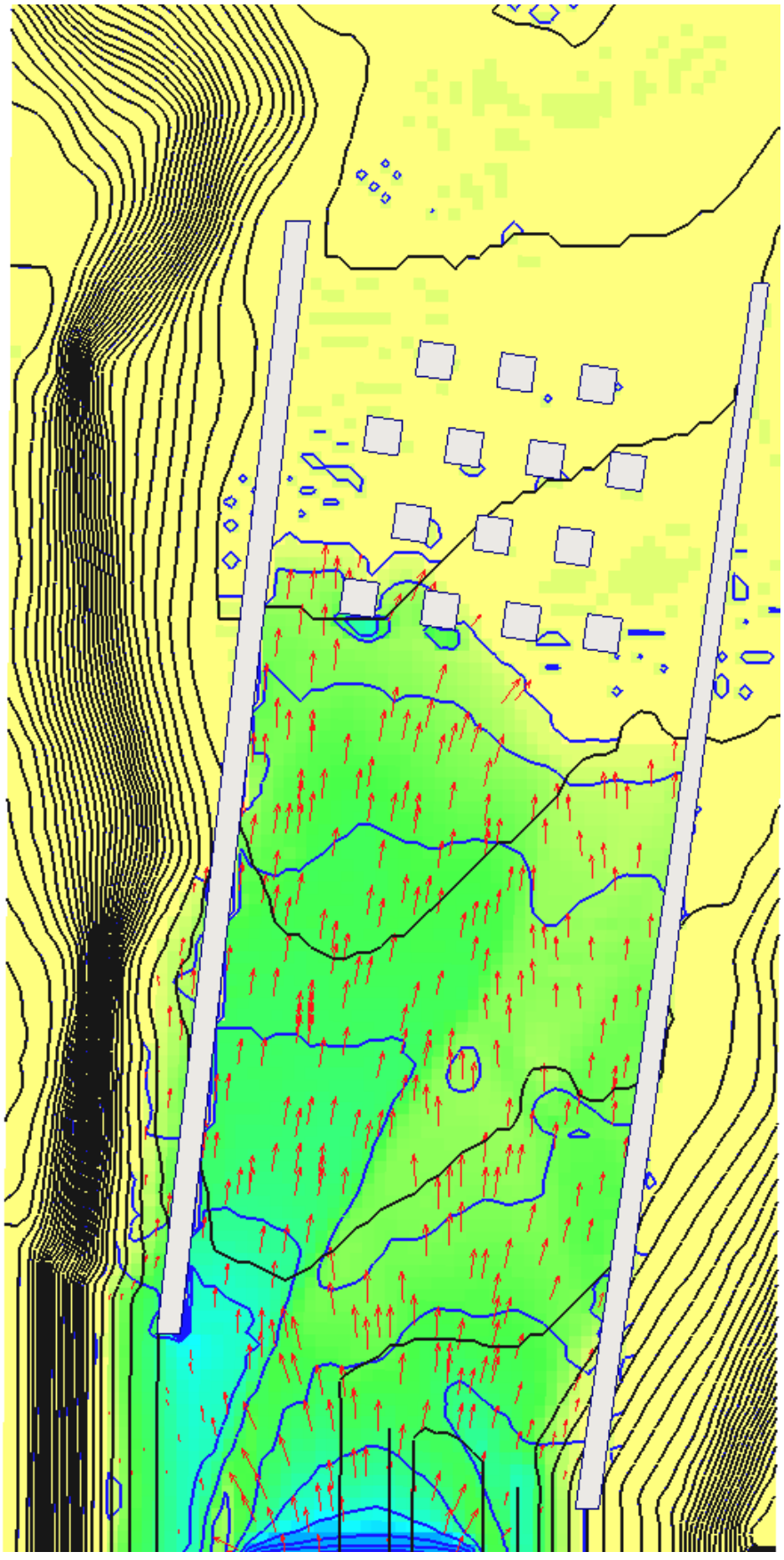

Figure 4.36: Computer simulation of the Toce basin urban flash-flood experiment. Terrain and water surface coordinates are marked at 0.2 meter intervals. Arrows have area proportional to discharge. Medium flow through a staggered arrangement of blocks. t = 10 seconds.

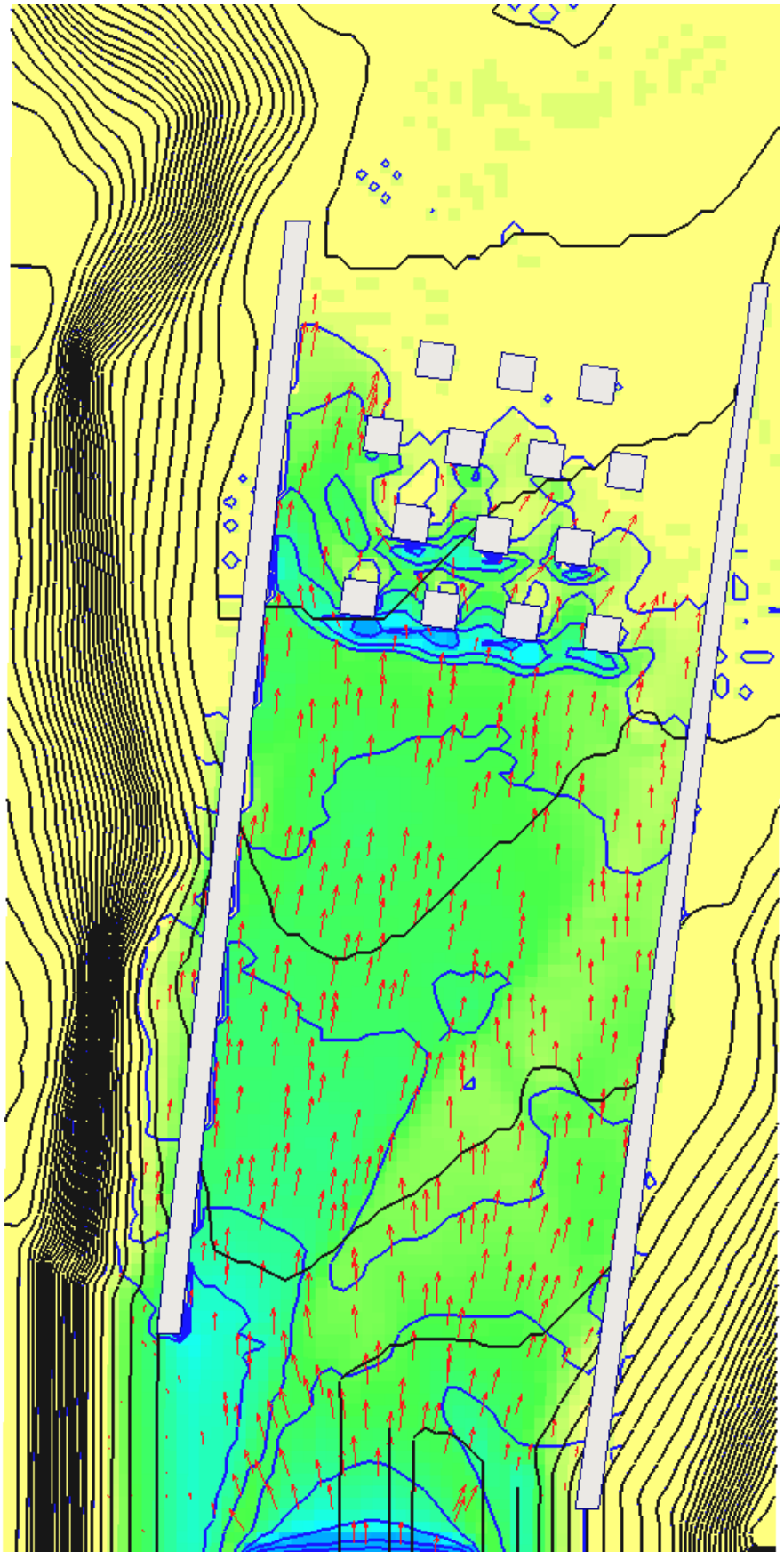

Figure 4.37: Computer simulation of the Toce basin urban flash-flood experiment. Terrain and water surface coordinates are marked at 0.2 meter intervals. Arrows have area proportional to discharge. Medium flow through a staggered arrangement of blocks. t = 11 seconds.

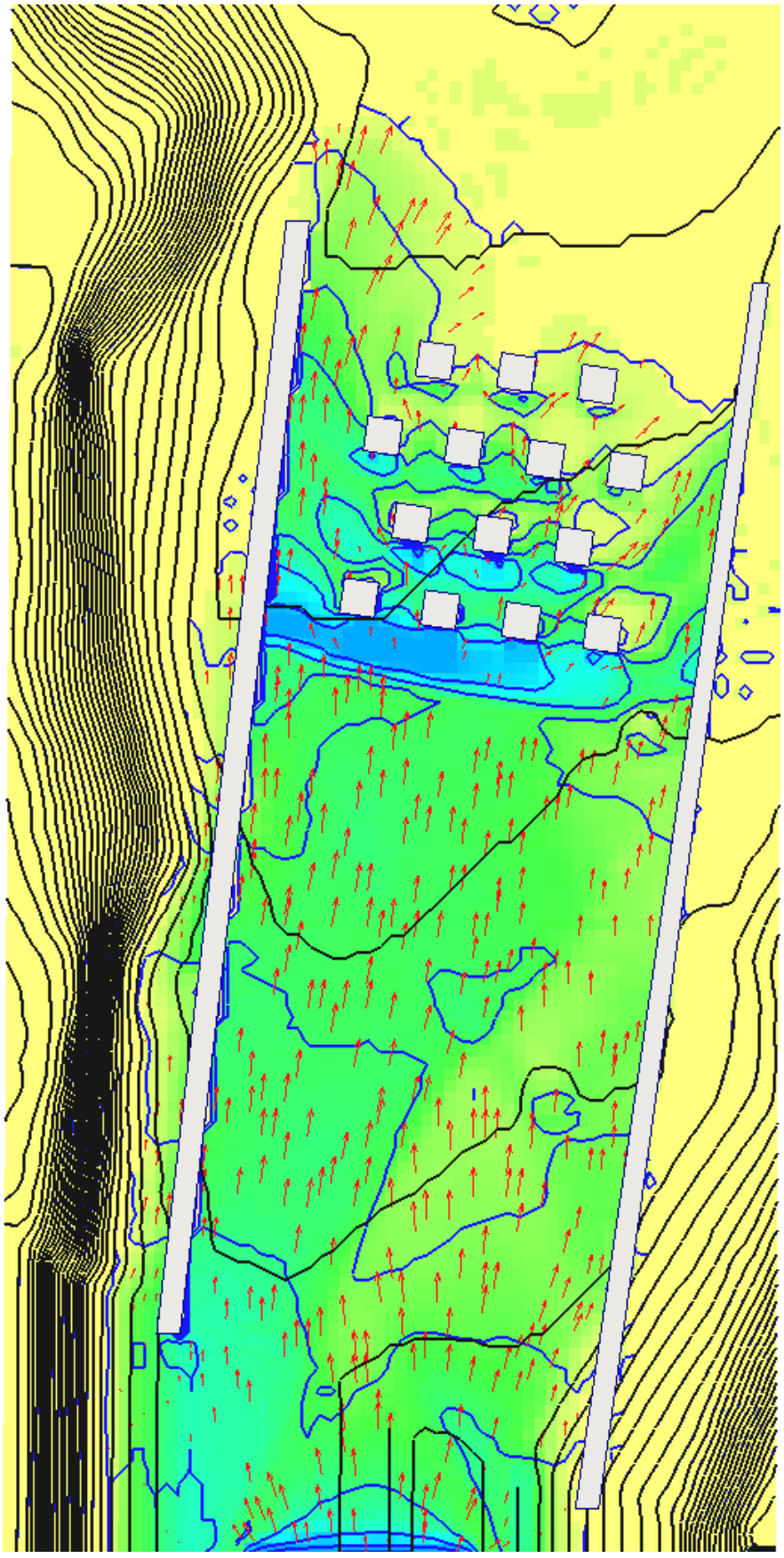

Figure 4.38: Computer simulation of the Toce basin urban flash-flood experiment. Terrain and water surface coordinates are marked at 0.2 meter intervals. Arrows have area proportional to discharge. Medium flow through a staggered arrangement of blocks. t = 12 seconds.

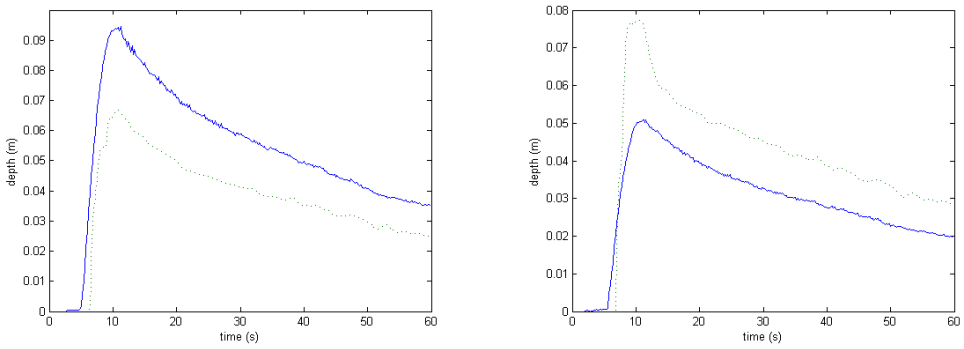

(a) Gauge 1

(b) Gauge 2

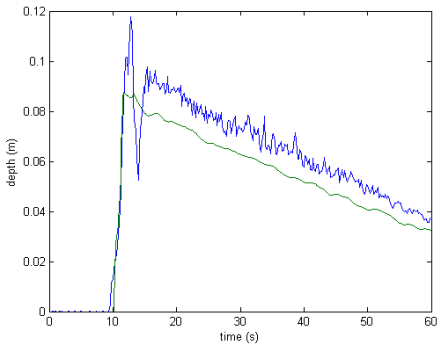

(c) Gauge 3

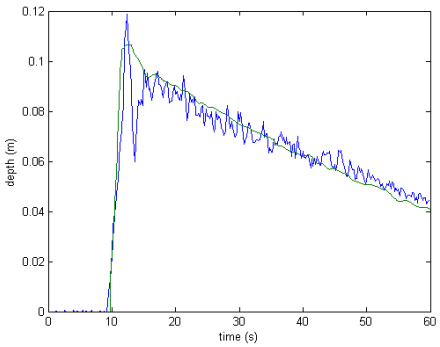

(d) Gauge 4

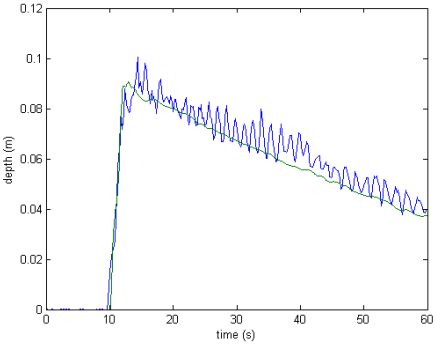

(e) Gauge 5

Figure 4.39: Toce basin urban flash flood experiment. Medium flow through a staggered arrangement of blocks. Comparison of measured (blue) and simulated (green) levels.

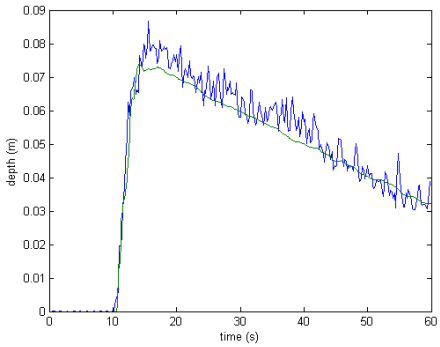

(a) Gauge 6

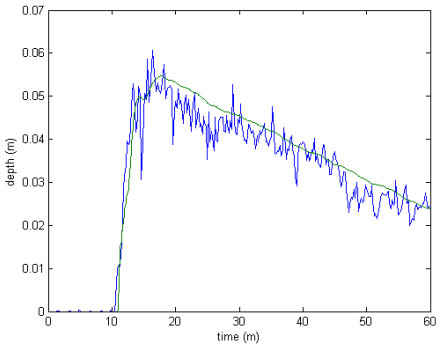

(b) Gauge 7

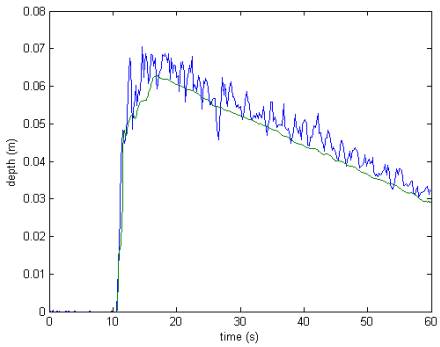

(c) Gauge 8

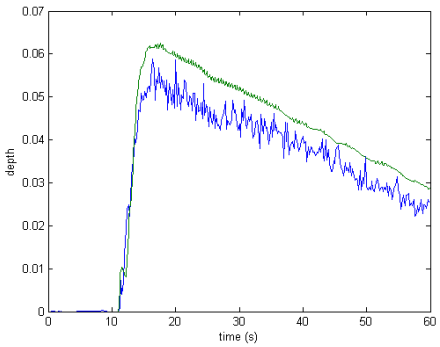

(d) Gauge 9

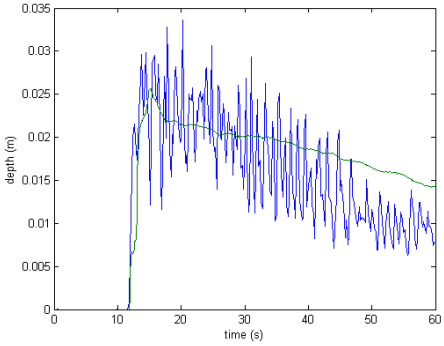

(e) Gauge 10

Figure 4.40: Toce basin urban flash flood experiment. Medium flow through a staggered arrangement of blocks. Comparison of measured (blue) and simulated (green) levels.

4.4 Glasgow Test Case

The Glasgow test case (Hunter *et al.* (2008); Neelz and Pender (2013)) was developed by the Flood Risk Management Consortium in association with the Environment Agency and a number of academic research groups. The intent is to test a model of urban flooding at high resolution. It is distinct from the Toce basin experiment in that it involves a mixture of slow diffusive flow, and fast advective flow conditions. There are differences between versions of this test available. This simulation is more relevant to the results of Hunter. The data set was made available by the Environment Agency.

The domain covers a 400m by 1000m area of Glasgow. This is a residential area containing apartment blocks, plus terraced and individual housing. Gradients are steep in places, with a predominant East-West slope spanned by two main roads which form the main drainage path for the floodwater. The Mannings n roughness parameters for road and rough ground are 0.015 and 0.05 respectively. Flooding comes from an overflowing storm drain. The drain is located within the mapped area, the direction of flow is distinctly Westward. The area East of the drain was excluded and the inflow was positioned at the Eastern wall. Buildings are included as solid obstacles, Roads and pavements are distinguished using the Cartesian cut-cell routines (Chapter 3.3.5.1). The Manning roughness parameters used are 0.05 off-road, 0.015 on-road, in accordance with the EA data. Hunter *et al.* (2008) also adjusts the topography to represent kerbs, although this is not replicated in this case. The vector data for buildings and roads amounted to 12,000 and 20,000 vector points respectively. To cut this down to a manageable size the polygons were pruned using the Douglas-Peucker algorithm Douglas and Peucker (1973). The data was also edited to avoid degenerate cut cell regions. It was possible to retain a great deal of detail from this data with less than 3,000 points for buildings and about 600 points for roads. Some of the smaller buildings

were altered significantly and one was removed. All of the significant changes were made to buildings outside of the wetted region.

There are nine indicated gauge locations in the Environment Agency tests. Of these records for gauges P1,P8,P3 and P4 are recorded by the benchmark.

4.4.1 Results

The computations are executed after the main development phase, and so no modifications to the original program were made in the context of this simulation. Two sets of results are presented. Test A peaking at $10m^3/s$, ran for 30minutes. Test B which ran for 100 minutes, has discharge peaking at $20m^3/s$. Test A ran for 24 hours on a 2.1 GHz, 2GB RAM laptop PC. The second processor was not used. Test B ran for 52 hours on a 2.19 GHz 1.25GB RAM desktop PC.

Runtime failures were difficult to avoid with this case (the authors were only working with a compiled copy of the program). The error was a square root domain error, which should be straight forward to identify in a coding environment. A coding error has been identified which is most likely cause. This relates to the calculation of boundary values for inflow boundary conditions. In order to avoid run-time errors a minimum flow depth of 0.005 meters and momentum-velocity depth of 0.02 meters were used. These are much higher than required to mitigate instabilities arising from wetting and drying, but were necessary to avoid the run-time errors encountered.

4.4.1.1 Test A

The snapshot at 30 minutes (figure 4.43) is similar to the other results from the benchmark tests. One exception is the depth near the inflow boundary. Water also reaches the gauges (figure 4.44) earlier than in the benchmark results. The peak water level at gauge X1 is also marginally higher. Downstream at gauge X2 the

Figure 4.41: Glasgow flood benchmark test initial conditions. Lighter background indicates higher land. Red lines are paved region outlines. The beige outlined figures are buildings. The inflow is marked with an blue diamond. Gauges are marked with yellow crosses, numberings are from the Environment Agency version. Benchmark gauges 1,2,3 and 4 are equivalent to E.A. gauges 1,8,3 and 4.

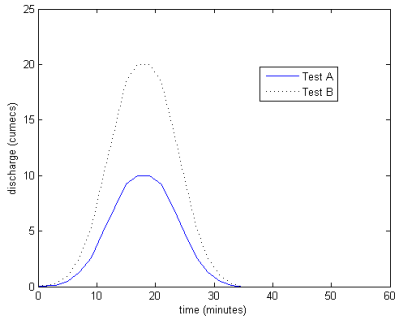

Figure 4.42: Glasgow flood, discharges from the culvert in test cases A (solid line) and B (dotted line).

water level is lower than all but one of the benchmarks. The exception is TRENT, the only other finite volume solver. It is difficult to determine what causes these discrepancies. There is as much variation between the other benchmark tests as there are differences with the results produced here.

4.4.1.2 Test B

The result of this simulation (figure4.46,4.47) are qualitatively very similar to the benchmark tests. The main exception is that final settled pond region has expanded to encompass gauge X4 (figure 4.45(d)). There are significant puddles remaining in the drying regions although depth the at gauge X2 (figure 4.45(b)) is still falling at the end of the simulation.

4.4.2 Conclusions

The Glasgow benchmark test case was simulated using AMAZON-CC. The solid obstacles and roads were successfully represented using the Cartesian cut-cell routines. Difficulties were encountered which are most likely due to a coding error in the inflow boundary routines. Despite this the a significant part of the benchmark test was reproduced convincingly with accurate parameters. A longer simulation with similar boundary conditions ran successfully. This demonstrated that AMAZON can handle both sub-grid domain features and wetting and drying under complex flow conditions. Further simulations need to be run. The runtime errors encountered urgently need to be identified and fixed. A number of tests should be carried out to identify the optimal wetting and drying parameters. It would also be valuable to follow the original benchmark tests more thoroughly with the range of parameters specified. This would require a substantial commitment of processing time or faster computers.

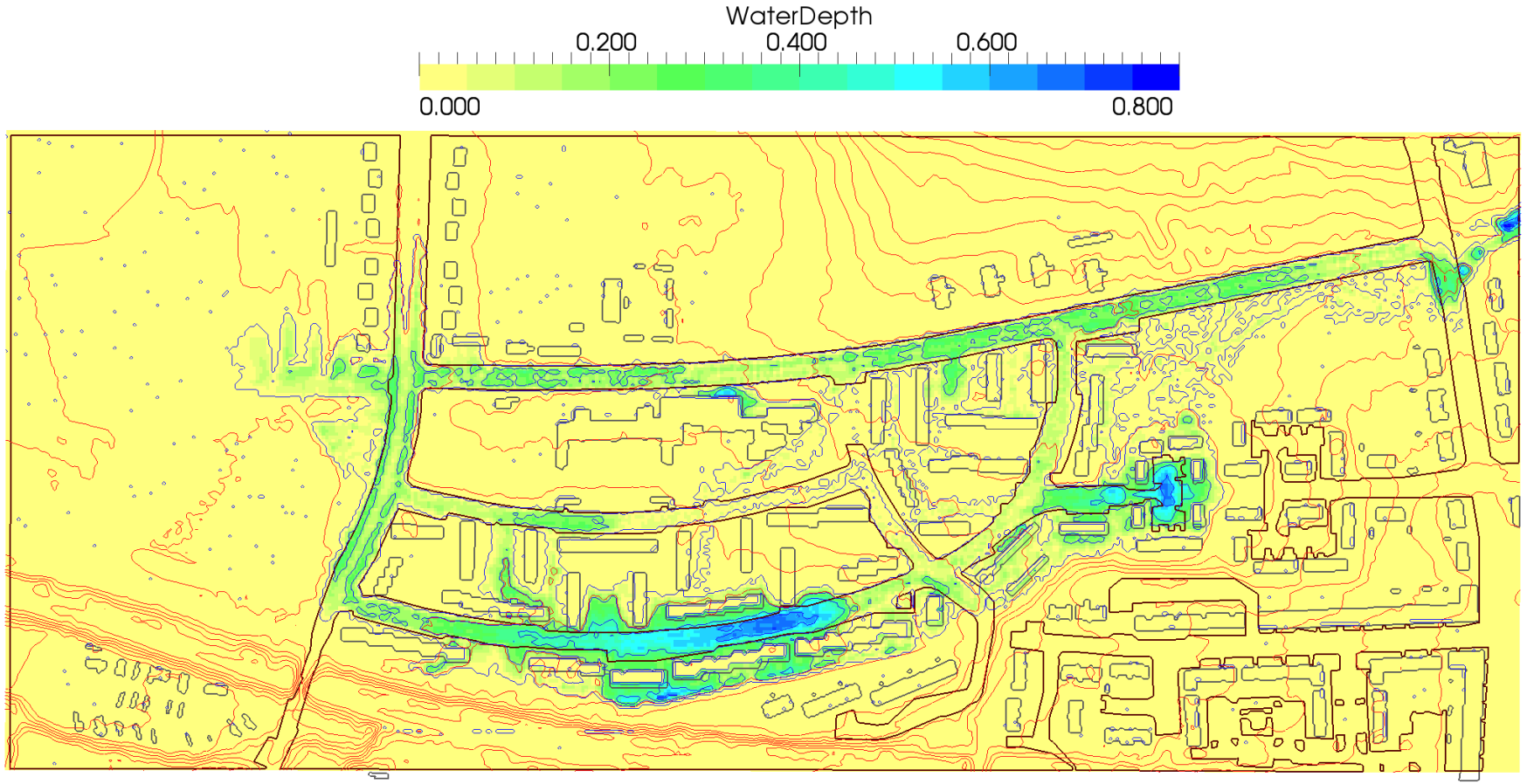

Figure 4.43: Glasgow flood benchmark. Test A, benchmark inflow, snapshot after 30 minutes. Road outlines are brown, building outlines are grey. The red contours mark land height at meter intervals. Blue contours mark water depth at 0.2 meter intervals and include a wet-dry boundary contour.

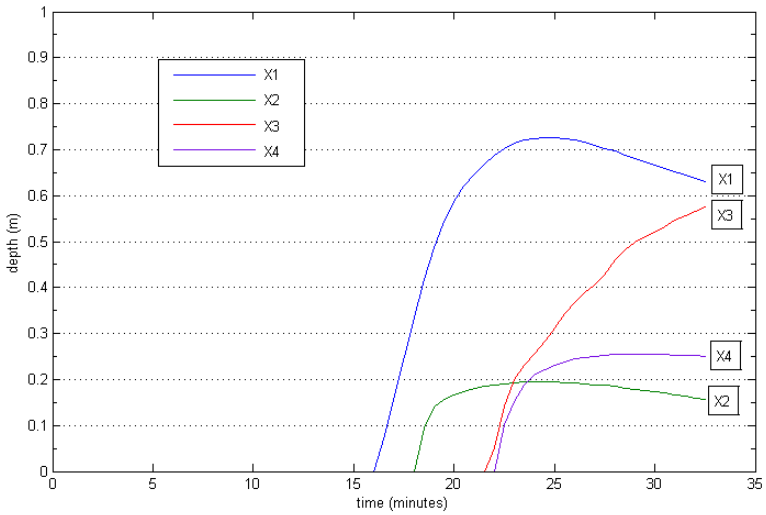

Figure 4.44: Glasgow flood, test A, benchmark inflow. Water depths at gauges X1 to X4.

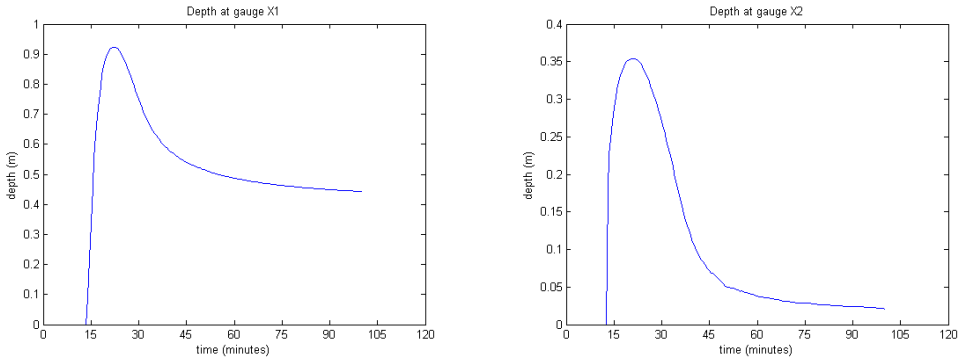

(a) Gauge 1

(b) Gauge 2

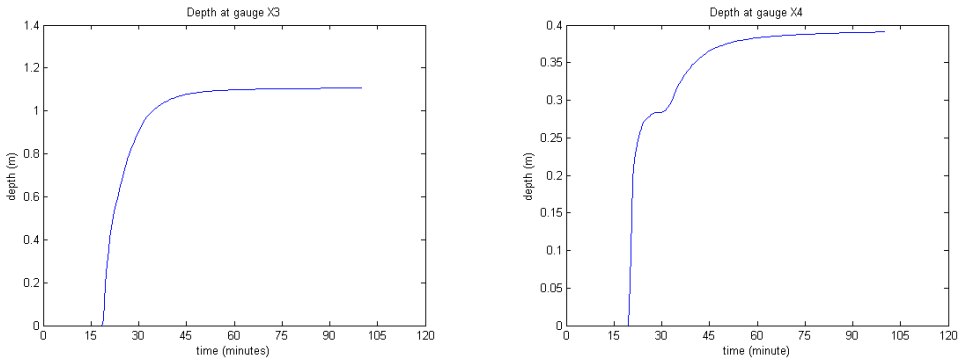

(c) Gauge 3

(d) Gauge 4

Figure 4.45: Glasgow flood benchmark test. Test B high inflow. Depths at gauges X1 to X4

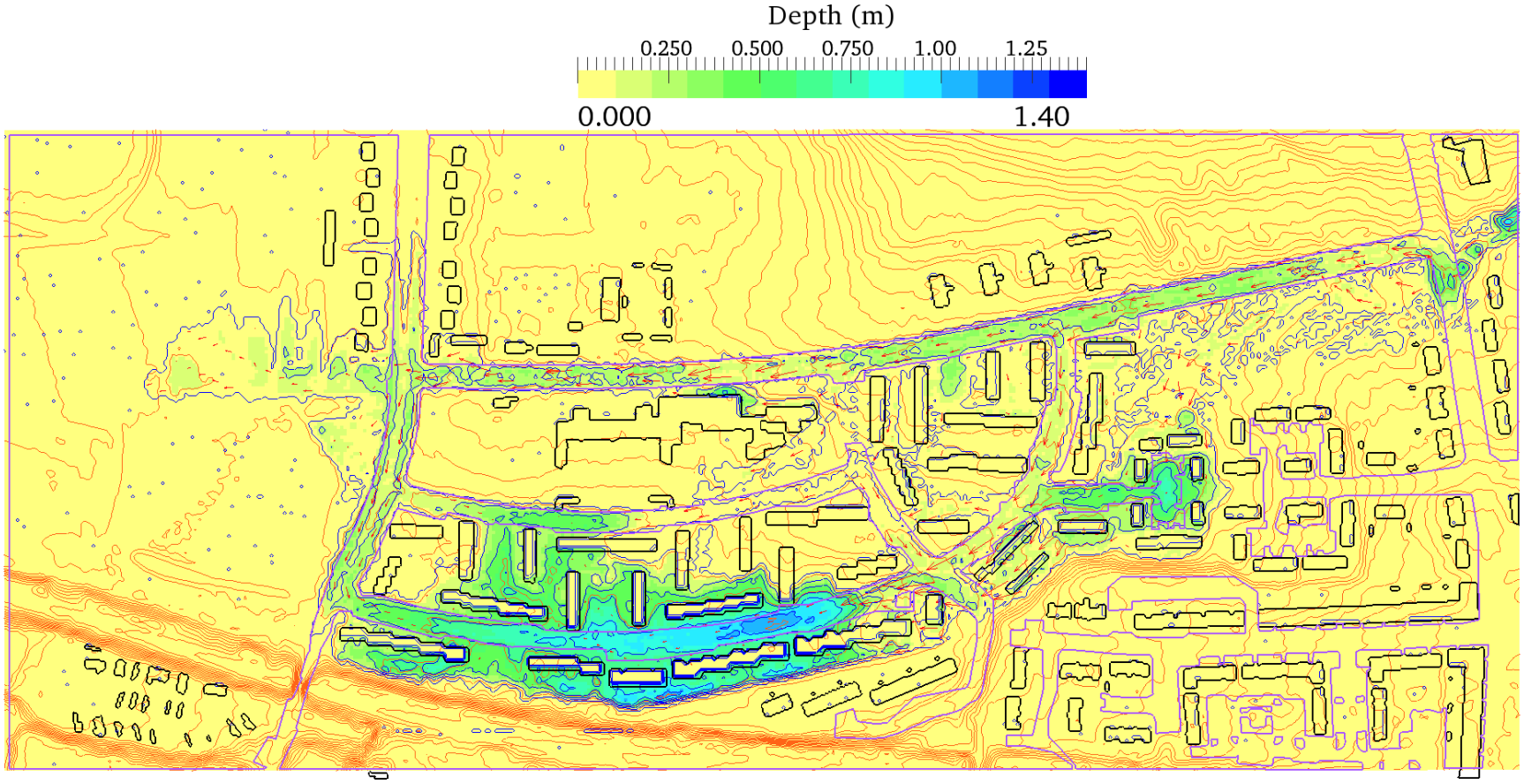

Figure 4.46: Glasgow flood benchmark. Test B, benchmark inflow, snapshot after 30 minutes. Road outlines are brown, building outlines are grey. The red contours mark land height at meter intervals. Blue contours mark water depth at 0.2 meter intervals and include a wet-dry boundary contour. Arrows indicate flow velocity.

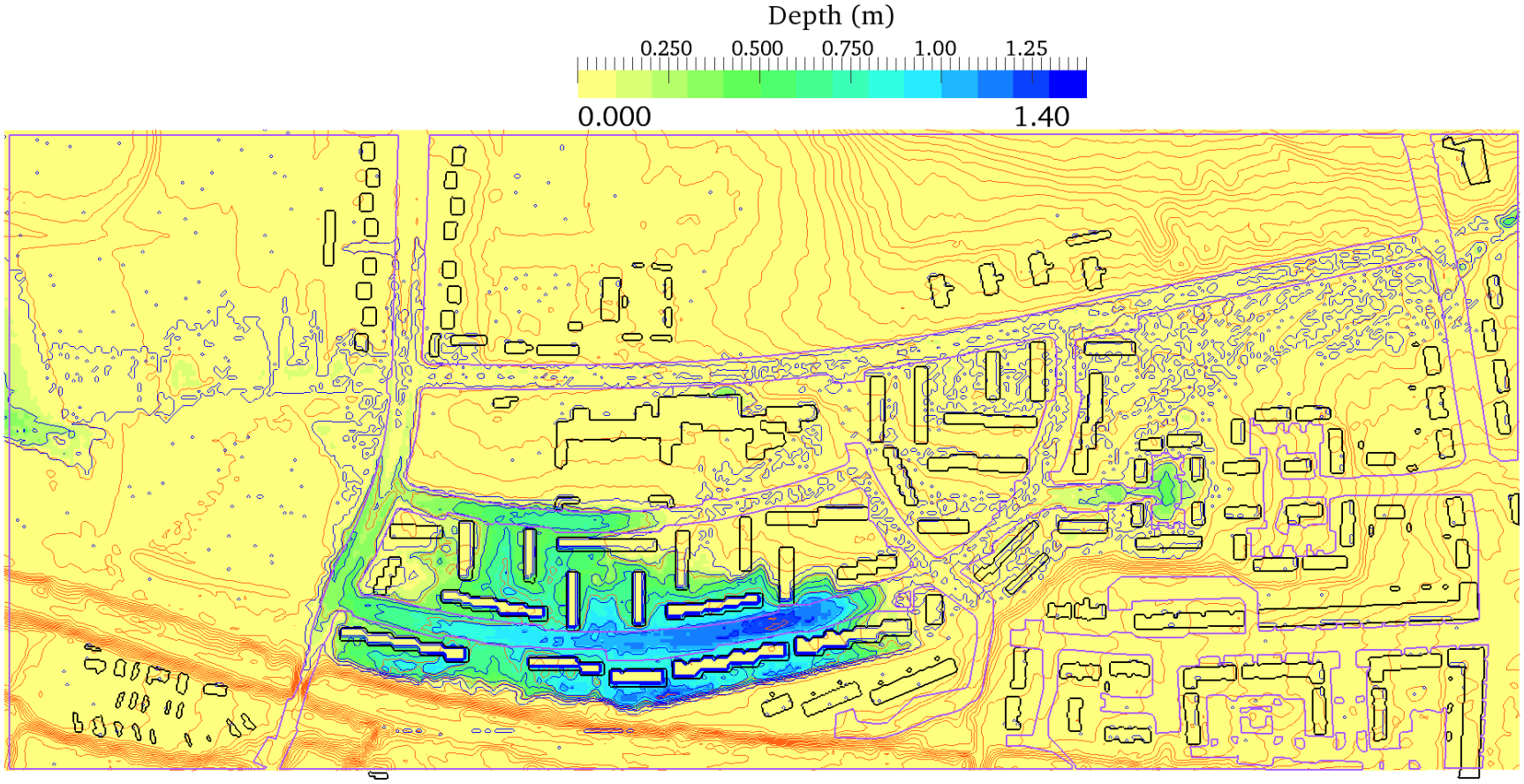

Figure 4.47: Glasgow flood benchmark. Test B, benchmark inflow, snapshot after 60 minutes. Road outlines are brown, building outlines are grey. The red contours mark land height at meter intervals. Blue contours mark water depth at 0.2 meter intervals and include a wet-dry boundary contour.

4.5 Flow through a Semi-Permeable Boundary

Steady state flow through semi-permeable cut cell is analysed here. A 100m long, 1m wide rectangular channel has a semi-permeable boundary across it halfway along. The porosity of the boundary varied from 01% to 90%. The depth at outflow is kept at 1m, while the rate of inflow varies from 0.1 to 5 cumecs. The full set of results are tabulated in 4.4,4.5,4.6,4.7,4.8,4.9,4.10. The obvious outlier in 4.4 can be safely ignored.

The results show that for moderately to highly permeable boundaries the effect is marginal. This is understandable if compared with common obstacles such as railings and fences. In real cases these obstacles can become clogged with debris, during or preceding a flood event, but otherwise have a marginal impact on flow.

Although it was not a goal of this implementation, it would be desirable to reproduce the head loss terms associated with sudden expansions. The Borda equation (Equation 4.2) has a sound theoretical basis and has been shown to give accurate predictions.

$$H_B = \xi \frac{(u^* - u_R)^2}{2g} = \xi \left(\frac{h_R - \psi h^*}{\psi h^*} \right)^2 \frac{u_R^2}{2g} \tag{4.2}$$

To estimate the transitional values h^* and u^* it is assumed that upstream conditions dominate. The tables below show two distinct behaviours.

The head losses are broadly consistent with equation 4.2 for a subcritical flow regime, albeit an order of magnitude greater than might reasonably be expected. The parameter ξ, which should be less than one, varies between 7 and 40.

When there is a hydraulic drop, ξ depends entirely on the porosity of the boundary. This relationship is far from simple however. Other dimensionless measures, such as the Froude number, are also related. The Borda equation does not appear to be a good model for these cases.

Figure (4.48) plots proportionate head loss $\frac{\Delta H}{H_0}$ against $1 - \psi$ when there is a

hydraulic drop. The trend is smooth and monotonic. It is possible to fit a simple function to these values. Equation 4.3 based on porosities 0.01 to 0.2, is one such example. It is a good statistical fit only for porosities 0.01 to 0.2.

$$\frac{\Delta H}{H_0} \approx 0.872\,(1-\psi)^{1.696} \tag{4.3}$$

Table 4.4: Steady flow through a semipermeable boundary with porosity $\psi = 0.01$. Depth h, speed u, Froude number Fr and hydraulic head H upstream and immediately downstream of the boundary. H_B is the head loss derived from the Borda equation 4.2 assuming $\xi = 1$. ΔH is the measured head loss. Derived values are left out in the second column, due to the dubious quality of the data.

Q	0.1	0.2	0.5	1.0	2.0	5.0
h_0	3.7900	0.5156	9.3723	13.900	21.950	40.408
u_0	0.0260	0.3560	0.0526	0.0713	0.0910	0.1220
Fr_0	0.0043	0.1583	0.0055	0.0061	0.0062	0.0061
H_0	3.7900	0.5220	9.3725	13.900	21.950	40.409
h_1	1.0000	1.0000	1.0001	0.1716	0.2684	0.4902
u_1	0.0980	0.1967	0.4937	5.9375	7.4610	10.124
Fr_1	0.0313	0.0628	0.1576	4.5760	4.5982	4.6166
H_1	1.0005	1.0020	1.0125	1.9684	3.1056	5.7137
H_B	0.3154		1.1619	0.0989	0.1408	0.2373
$\frac{\Delta H}{H_B}$	8.8432		7.1954	120.72	133.83	146.22
$\frac{\Delta H}{H_0}$	0.7360		0.8920	0.8584	0.8585	0.8586

Table 4.5: Steady flow through a semipermeable boundary with porosity $\psi = 0.02$. Depth h, speed u, Froude number Fr and hydraulic head H upstream and immediately downstream of the boundary. H_B is the head loss derived from the Borda equation 4.2 assuming $\xi = 1$. ΔH is the difference between upstream H_0 and downstream H_1 heads.

Q	0.1	0.2	0.5	1.0	2.0	5.0
h_0	2.6759	3.7573	6.1662	9.0844	14.029	25.834
u_0	0.0374	0.0533	0.0811	0.1101	0.1426	0.1935
Fr_0	0.0073	0.0088	0.0104	0.0117	0.0122	0.0122
H_0	2.6760	3.7574	6.1665	9.0850	14.030	25.836
h_1	1.0000	1.0000	1.0000	1.0000	0.3347	0.6125
u_1	0.1005	0.2009	0.5024	1.0049	6.0626	8.2270
Fr_1	0.0321	0.0641	0.1604	0.3208	3.3457	3.3562
H_1	1.0005	1.0021	1.0129	1.0515	2.2081	4.0622
H_B	0.1610	0.3116	0.6501	1.0441	0.0697	0.1186
$\frac{\Delta H}{H_B}$	10.406	8.8425	7.9273	7.6944	169.62	183.52
$\frac{\Delta H}{H_0}$	0.6261	0.7333	0.8357	0.8843	0.8426	0.8428

Table 4.6: Steady flow through a semipermeable boundary with porosity $\psi = 0.05$. Depth h, speed u, Froude number Fr and hydraulic head H upstream and immediately downstream of the boundary. H_B is the head loss derived from the Borda equation 4.2 assuming $\xi = 1$. ΔH is the difference between upstream H_0 and downstream H_1 heads.

Q	0.1	0.2	0.5	1.0	2.0	5.0
h_0	1.7753	2.3232	3.5648	5.1134	7.6470	14.081
u_0	0.0565	0.0863	0.1404	0.1958	0.2617	0.3552
Fr_0	0.0135	0.0181	0.0237	0.0276	0.0302	0.0302
H_0	1.7755	2.3236	3.5658	5.1153	7.6504	14.088
h_1	1.0000	1.0000	1.0000	1.0000	0.4317	0.7912
u_1	0.1005	0.2010	0.5025	1.0050	4.6861	6.3592
Fr_1	0.0321	0.0642	0.1604	0.3209	2.2771	2.2825
H_1	1.0005	1.0021	1.0129	1.0515	1.5510	2.8523
H_B	0.0543	0.1192	0.2736	0.4363	0.0186	0.0316
$\frac{\Delta H}{H_B}$	14.285	11.085	9.3321	9.3138	327.12	355.77
$\frac{\Delta H}{H_0}$	0.4365	0.5687	0.7160	0.7944	0.7973	0.7975

Table 4.7: Steady flow through a semipermeable boundary with porosity $\psi = 0.1$. Depth h, speed u, Froude number Fr and hydraulic head H upstream and immediately downstream of the boundary. H_B is the head loss derived from the Borda equation 4.2 assuming $\xi = 1$. ΔH is the difference between upstream H_0 and downstream H_1 heads.

Q	0.1	0.2	0.5	1.0	2.0	5.0
h_0	1.3854	1.6862	2.3959	3.3122	4.8066	8.8502
u_0	0.0724	0.1190	0.2091	0.3024	0.4165	0.5653
Fr_0	0.0196	0.0293	0.0431	0.0530	0.0607	0.0607
H_0	1.3856	1.6869	2.3981	3.3169	4.8154	8.8665
h_1	1.0000	1.0000	1.0000	1.0000	0.5072	0.9303
u_1	0.1005	0.2010	0.5025	1.0050	3.9818	5.4033
Fr_1	0.0321	0.0642	0.1604	0.3209	1.7850	1.7886
H_1	1.0005	1.0021	1.0129	1.0515	1.3153	2.4184
H_B	0.0199	0.0501	0.1296	0.2099	0.0025	0.0039
$\frac{\Delta H}{H_B}$	19.347	13.680	10.685	10.794	1420.7	1655.4
$\frac{\Delta H}{H_0}$	0.2779	0.4060	0.5776	0.6830	0.7269	0.7272

Table 4.8: Steady flow through a semipermeable boundary with porosity $\psi = 0.2$. Depth h, speed u, Froude number Fr and hydraulic head H upstream and immediately downstream of the boundary. H_B is the head loss derived from the Borda equation 4.2 assuming $\xi = 1$. ΔH is the difference between upstream H_0 and downstream H_1 heads.

Q	0.1	0.2	0.5	1.0	2.0	5.0
h_0	1.1559	1.2927	1.6448	2.1380	2.9960	5.4713
u_0	0.0869	0.1553	0.3049	0.4688	0.6687	0.9147
Fr_0	0.0258	0.0436	0.0759	0.1024	0.1233	0.1249
H_0	1.1563	1.2940	1.6495	2.1492	3.0188	5.5139
h_1	1.0000	1.0000	1.0000	1.0000	1.0000	1.0491
u_1	0.1005	0.2010	0.5025	1.0050	2.0100	4.7885
Fr_1	0.0321	0.0642	0.1604	0.3209	0.6417	1.4926
H_1	1.0005	1.0021	1.0129	1.0515	1.2059	2.2178
H_B	0.0057	0.0169	0.0536	0.0922	0.0921	0.0020
$\frac{\Delta H}{H_B}$	27.364	17.235	11.887	11.899	19.677	1655.9
$\frac{\Delta H}{H_0}$	0.1347	0.2256	0.3859	0.5108	0.6005	0.5978

Table 4.9: Steady flow through a semipermeable boundary with porosity $\psi = 0.4$. Depth h, speed u, Froude number Fr and hydraulic head H upstream and immediately downstream of the boundary. H_B is the head loss derived from the Borda equation 4.2 assuming $\xi = 1$. ΔH is the difference between upstream H_0 and downstream H_1 heads.

Q	0.1	0.2	0.5	1.0	2.0	5.0
h_0	1.0401	1.0789	1.1929	1.3874	1.8122	3.2595
u_0	0.0966	0.1862	0.4209	0.7234	1.1067	1.5363
Fr_0	0.0302	0.0572	0.1230	0.1961	0.2625	0.2717
H_0	1.0406	1.0807	1.2019	1.4141	1.8746	3.3798
h_1	1.0000	1.0000	1.0000	1.0000	1.0000	1.1263
u_1	0.1005	0.2010	0.5025	1.0050	2.0100	4.4588
Fr_1	0.0321	0.0642	0.1604	0.3209	0.6417	1.3414
H_1	1.0005	1.0021	1.0129	1.0515	1.2059	2.1397
H_B	0.0010	0.0036	0.0155	0.0331	0.0297	0.0188
$\frac{\Delta H}{H_B}$	39.538	22.001	12.231	10.953	22.544	66.031
$\frac{\Delta H}{H_0}$	0.0385	0.0728	0.1573	0.2564	0.3567	0.3669

Table 4.10: Steady flow through a semipermeable boundary with porosity $\psi = 0.8$. Depth h, speed u, Froude number Fr and hydraulic head H upstream and immediately downstream of the boundary. H_B is the head loss derived from the Borda equation 4.2 assuming $\xi = 1$. ΔH is the difference between upstream H_0 and downstream H_1 heads.

Q	0.1	0.2	0.5	1.0	2.0	5.0
h_0	1.0018	1.0035	1.0093	1.0217	1.0845	1.8294
u_0	0.1004	0.2003	0.4978	0.9834	1.8527	2.7406
Fr_0	0.0320	0.0638	0.1582	0.3106	0.5680	0.6469
H_0	1.0023	1.0056	1.0219	1.0710	1.2594	2.2122
h_1	1.0000	1.0000	1.0000	1.0000	1.0000	1.1977
u_1	0.1006	0.2010	0.5025	1.0051	2.0095	4.1920
Fr_1	0.0321	0.0642	0.1604	0.3209	0.6416	1.2230
H_1	1.0005	1.0020	1.0129	1.0515	1.2058	2.0934
H_B	3×10^{-5}	0.0001	0.0007	0.0026	0.0048	0.0295
$\frac{\Delta H}{H_B}$	56.850	28.974	12.296	7.5849	11.183	4.0206
$\frac{\Delta H}{H_0}$	0.0018	0.0035	0.0089	0.0183	0.0426	0.0537

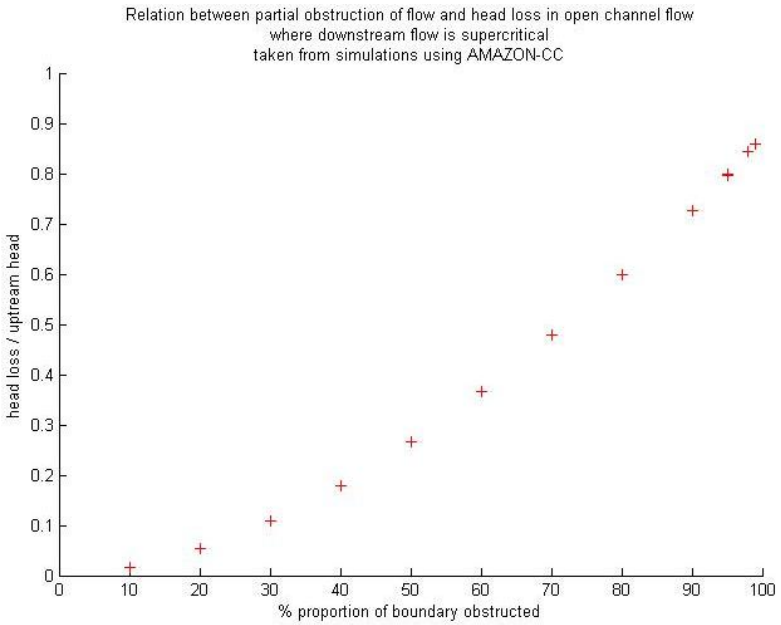

Figure 4.48: The energy loss as a percentage of initial hydraulic head to to the semi-permeable boundary when a transition from subcritical to critical flow is observed. Note that consistency has only been observed for a porosity of 0.1 and below

Chapter 5

Conclusions

5.1 Introduction

The focus of this thesis is on the AMAZON-CC package and its application to river flood simulations. AMAZON uses a particularly efficient formulation of the finite volume techniques.

The Cartesian cut-cell methods have been a focus of this study. The original application, which was to define impermeable regions, has proved to be useful in flood modelling. Other applications, making use of the same code, have been developed. The Glasgow flood test in particular demonstrated the value of these methods.

5.2 Results

5.2.1 Four Mounds

The four mounds test case 4.1 tested several wetting and drying routines in various combinations. The results show that some care must be taken in how the VFR method is implemented. The following compromises are all necessary, but have consistently achieved satisfactory results:

1. Ignoring the momentum flux into partially dry cells. Inertial terms are found by interpolation from the velocities in neighbouring cells.
2. Using velocity gradients in place of momentum gradients.
3. Using either of the VFR formulations is effective. The piecewise level formulatio was used subsequently. It requires fewer run-time calculations, and it avoids the problem with incomplete drainage mentioned by (Begnudelli and Sanders, 2006).

5.2.2 Isolated Obstacle

The grid block illustration (figure 4.11) shows how effective the cut-cell method is in delineating solid obstacles, albeit this example is large relative to the mesh.

There is no sign of asymptotic convergence, even for the simplest metric the gauge in the feed tank. There were features evident in the time series which were still emerging. A finer mesh than this is expected to reveal yet more detail. A significant consequence of this is that the results are grid dependant. This means that parameters calibrated on the model on one mesh resolution cannot be applied on any other mesh.

Although the side walls are defined using a reflective boundary condition, there is a small slope lead up to each wall. the water level was such that these slopes where partially dry during much of simulation, with no obvious artifacts as a consequence. Channel-bank interactions have been a particular problem for FV methods so this result demonstrates the effectiveness of the VFR.

5.2.3 Toce River Basin

The upstream boundary conditions used for the numerical model have errors. The rate of discharge into the system is correct, but located upstream and at an angle to the correct location. Nonetheless measurements taken around the obstacles match

those of the experiment and compare well to similar numerical models published elsewhere. These results show how the arrangement of blocks serve to mitigate these discrepancies.

A methodology has been proposed to treat built up areas as homogenous regions, using a porosity parameter to represent the building density(Guinot and Soares-Frazao, 2006; l'Homme *et al.*, 2006; Sanders *et al.*, 2008; Velickovic *et al.*, 2010). In this context it is useful to compare the two different scenarios. Of the downstream gauges only gauges 3,4,7 and 8 are comparable. The others are effected differently by the location of blocks immediately upstream or downstream. The two upstream gauges (3 and 4) agree markedly, for both the computer and physical simulations. Gauges 7 and 8 are located among the blocks. They give similar readings initially, though the final water level is lower for the aligned grid than for the staggered grid.

5.2.4 Glasgow Flood

The Glasgow experiment was carried out without altering the program in any way. The only one significant alteration to the experiment was to shorten the domain at the Eastern edge.

The processing of data before it could be entered was substantial. Great care was required to ensure that the raster data and the vector data were aligned. The vector data needed to be cleaned up substantially before it was usable. The parser has proved to be a valuable addition to the code despite its flaws.

The problems with the inflow boundary condition are severe and need to be remedied as a matter of urgency. The excessive depths near the culvert may be a function of this, or of attempts to prevent run-time errors at the boundary. A simpler and more likely explanation is that the storage around the culvert was cut in half by the domain boundary. This would also help explain the earlier

responses at the gauges. The depression around the culvert will have filled sooner and discharged sooner. This effect would be quite sensitive because the early discharge is small but increasing.

Despite these issues the simulation was convincing and comparable with the published results. AMAZON is clearly able to simulate the sorts of flows encountered in an urban flood.

The complexities involved however should not be underestimated. This test has highlighted the need for a flexible interface, which is well documented and complies strictly to universal standards when common data formats are used. The variety of scenarios which AMAZON-CC can handle has been greatly expanded. This means that the potential for errors has also increased, and so more work needs to be put into validating every aspect of the code. There is a demand for interfaces with other model components. The Environment Agency versions of this test require rainfall to be included. This is not an urgent requirement for this code.

5.2.5 Semi-permeable boundary results

The semi-permeable boundary methods have great potential, and work done so far is substantial, but as yet they are still in development. The Semi-permeable boundary tests are presented as a proof of concept. An attempt has been made to link them to the real-world problem of localised head loss, although this is not convincing.

The mix of boundary conditions at the same face presents difficulties when determining gradients. The simplest solution is to assume a discontinuity. This assumption is made in the current experiment.

Determining velocities at porous boundary condition presents a dilemma. The velocity normal to a wall must always be zero. For there to be flow through the

open boundary the velocity through it must not be zero. This contradiction also applies to normal cut cell but only in special cases. A natural solution is to look at physical flow through a constriction. The flow is all directed through the aperture at increased speed, and there is a strong pressure differential as the water leaves the aperture.

All results attributable to this method are not physically credible for the above stated reason. They do however allow the algorithms to be tested, and to develop a methodology for assessing future implementations of this technique.

5.3 Further Work

5.3.1 Consolidation

The bug in the code which was identified in the Glasgow test needs to be addressed urgently. The problems caused by this bug highlight the need for more extensive validation tests. The functionality of the code has been expanded greatly with the keyword driven parser. This has also increased the number of things which can go wrong. Additionally the parser does not deal with standard data formats, such as raster files in a standard fashion. This should be corrected, using validated library code as far as this is possible.

AMAZON has been applied to the Glasgow benchmark test successfully with an unusual boundary condition. Aside from simply re-running the test with the benchmark boundary condition, there are several permutations on this case which would be worth running. In particular varying the bed roughness would not only give further points of comparison with peer modelling packages, but it would help validate the use of vector data to outline regions with different roughnesses.

Some of the methods used have not been explicitly tested. The use of ghost boundary values in place of ghost cell values was implemented to address a specific

problem. It was found that using ghost cells introduced a slight delay to periodic boundary conditions. The modification was successful, although the specific test case belongs to a third party. It would be worthwhile devising a test case to demonstrate this phenomenon.

The Berger LP limiter has been applied to a few cases, though not to any case where it had a noticable effect. It was implemented in anticipation of the SPIn boundary techniques. This is not at the stage where modifications to the slope limiter would be relevant. A follow up paper (May and Berger, 2013) has been written which applies these methods specifically to two dimensional schema. The test cases given apply the linear advection equation. These could be adapted to the shallow water equations without much difficulty.

5.3.2 Possible applications for the SPIn boundary method

In principle the range of possible applications is very broad. In the medium term it will be necessary to limit the scope of the method. This means simple testable internal boundary conditions.

The simplest would be a solid wall. A generalised implementation of this would require additional coding. If the wall is to be applied in any meaningful way the water must be able to flow on either side, which means that the wall needs to terminate within the domain. This presents new programming challenges since it requires a free flowing cell to interface with two separate cut cells on the same side. An ad hoc fix would be to ensure the boundary terminates at a grid point.

The treatment of terminal nodes is a peculiar problem which affects many applications of the code. It is reasonable to expect multiple internal boundaries to intersect or meet at a common node. This presents additional non-trivial programming difficulties, although these have been addressed before (Armesto-Álvarez, 2008).

The head loss term applied to flows over steps in bed-level has been shown to be part of a broader family of very similar equations. The bed step algorithms have been shown to be effective across gridded boundaries on a previous version of AMAZON. It would be possible, first to re-code this for the current version, and then to apply it using the cut cell methods.

The domain bounds are currently restricted to a rectangular orthogonal shape. Often the domain of interest is a different shape or at an angle to the raster data set. Implementing other boundary conditions on solid objects would allow any shape of domain to be created. This implementation is anticipated in the way that boundary conditions are parameterised by this solver. It should be possible to apply this simply by modifying the data-entry and preprocessing modules.

5.3.3 Interaction with other models

To provide an interface with other submodels is a natural extension to any modelling package.

One natural extension would be an interface with 1D channel flow submodels. This would allow the correct scale to be used for both parts of the system, the turbulence effect noted in chapter 2.3.1.2 to be modelled explicitly, and avoid a lengthy setup time. This has already been done. Using the cut-cell tools developed for this model can be expected to significantly improve the accuracy with which it can be done. This is a long term aspiration, but one which the author(s) would dearly love to see happen.

Appendix A

Sample control files

A.0.4 Isolated Obstacle

```
Isolated Obstacle Test Case {A.Morris, 24th July 2010 }


********************************************************************************
(The first line is the title of this run (up to 80 characters)

Mandatory parameters come first between      SYSTEM        and  ENDSYSTEM

Optional parameters follow between          SIMULATION    and  ENDSIMULATION

Vector data (ie solid bodies) belong between SOLIDBODIES  and  ENDSOLIDBODIES

Boundary conditions follow between          BOUNDARY      and  ENDBOUNDARY

Output file settings *can* follow between   OUTPUT        and  ENDOUTPUT {under construction}

Keywords commands are read line by line ignoring leading whitespaces.

********************************************************************************

SYSTEM
6000              [  maximum number of time steps
30.0              [  maximum run time (s)
35.8              [  width of domain  (m) (in the x-direction)
3.60              [  length of domain (m) (in the y-direction)
358               [  number of cells in the x direction
72                [  number of cells in the y direction
0.45              [  courant number CFL limiting the time step where (vel*dt < CFL*dx)
0.001             [ Minimum calculated depth of flow
0.005             [ Minimum depth used as a factor in velocity calculations (vel = hv / h)

# keyword list
# STEADY      [ Find steady state solution
#  parameter:   threshold of (the greatest shange in depth in a single time step)
#
# MINMOD      [ Use min-mod slope limiter
# SUPERBEE    [ Use Superbee slope limiter
# VANLEER     [ Use the Van Leer slope limiter    -{default}-
# VANALBADA   [ Use the Van Albada slope limiter
#
# VELGRAD     [ use gradient for velocity instead of momentum
# NOGRADIENT  [ do not calculate gradients (i.e. 1st order accuracy in space)
#
# SIMPLIFIED  [ level/storage relationship is used (work by A.Morris following B. Sanders)
# PD01        [ Partially dry cells are considered still
# PD02        [ Partially dry cells match the neighbour's velocity at each wet face
#
# PARAVIEW    [ output data as a .vtk file
#  parameters: 1) path\name of file (without the extension ".vtk")
#              *2a) TIME -{optional}- put out timed sequence of files
#              *2b) the period between records
#
# SOLID BODY  [ define regions with polygons. These may be solid regions or
#             [ areas where a parameter is given the same value
#  parameters: 1) number of polygons (for array allocation)
#              2) maximum number of intersections
#              3) number of vertices (for array allocation)
#              4) max error in finding cutting points (relative to cell size)


SOLID
4
200
5
0.001

GAUGES
6
10.35 2.95
```

```
 70: 10.35 1.20
 71: 11.70 2.95
 72: 11.70 1.00
 73: 12.90 2.10
 74: 05.83 2.90
 75:
 76: PARAVIEW
 77: IsolObstacle
 78: TIMESTEP
 79: 1.0
 80:
 81: VELGRAD
 82:
 83: SIMPLIFIED
 84:
 85: PDO2
 86:
 87: MANNING
 88:
 89: ENDSYSTEM
 90:
 91: ********************************************************************************
     **
 92:
 93: SIMULATION
 94:
 95: # Default values are zero for these parameters.
 96: # (not both depth and surface level can be consistently defined on the same domain)
 97: #
 98: # keyword list
 99: # TOPOGRAPHY or BATHYMETRY  [  bed elevation (array dimensions nX+1 by nY+1)
100: # XVELOCITY                 [  initial velocity in the x-direction (m/s)
101: # YVELOCITY                 [  initial velocity in the y-direction (m/s)
102: # LEVEL                     [  initial water surface level above a datum (m)
103: # DEPTH                     [  initial water depth (m)
104: # CHEZY                     [  bed resistance using Chezy value
105:
106: # data entry methods
107: #
108: # include an '=' sign with the keyword and put the value on the next line
109: #
110: # include a '+' sign with the keyword to enter data in a rectangular sub-area
111: #  the following parameters go *before* any other data or keywords
112: #  Parameters: 1) two i-indices, the first and last cells
113: #              2) two j-indices, the first and last cells
114: #
115: # use HERE and follow with text data
116: # e.g.
117: # LEVEL
118: # HERE
119: # 0.1 0.2 0.3 ...
120: # 0.3 0.4 0.5 ...
121: # ... and so on ...
122: #
123: # use FILE and follow with the name and path of a file containing binary data
124: # e.g.
125: # LEVEL
126: # FILE
127: # c:\AMAZON\dambreak\wetbed_dam_40.dat
128: #
129: # use RASTER to read data from a raster text file
130: # keywords:
131: #           FILE  mandatory penultimate line, used as above
132: #           ADJUST subtract a constant (put on following line) from the values read
133: #           TIMES multiply the values by a constant (after applying adjust)
134: #           FROM identify an origin, relative to the coordinates used by the raster
        file
135: #                these coordinates are given on the next line
136: #           SCALE follows with the ratio of the solver cell size, to the raster
        cell size
137: #           NODATAValue indicates the NullDataValue header line is used
138:
139:
140: ROUGHNESS=      Manning's value for roughness
141: 0.01
```

```
142:
143: LEVEL=          Initial water level in the channel
144: 0.02
145:
146: LEVEL+=         Initial water level in the reservoire
147: 1 77
148: 1 72
149: 0.4
150:
151: BATHYMETRY+^    Sloping bed on right bank
152: 1 359
153: 1 7
154: 0.155
155: 0.155
156: 0.0182
157:
158: BATHYMETRY+^     Sloping bed on left bank
159: 1 359
160: 67 73
161: 0.0182
162: 0.0182
163: 0.155
164:
165:
166: ENDSIMULATION
167:
168:
169: ********************************************************************************
     ****
170:
171: SOLIDBODIES
172:
173: # keywords
174: # SOLID indicates a solid immobile body
175: #  Parameters: 1) number of vertices on body (n)
176: #              2) OPEN   :: if the first and last vertices do not join, forming a
     line
177: #              or CLOSED :: if the last vertex is joined to the first forming a
     polygon
178: #       3 to 2+n) x, y   :: coodinates on solid body (in sequence counterclockwise)
179: #
180: # POLYGON indicates a region over which parameters are specified
181: #  Parameters: 1) number of vertices on polygon (n)
182: #              2) OPEN   :: if the first and last vertices do not join, forming a
     line
183: #              or CLOSED :: if the last vertex is joined to the first forming a
     polygon
184: #       3 to 2+n) x, y   :: coodinates of vertices (in sequence counterclockwise)
185: #      n+1 + 2*p) Keywords follow to name a parameter to be set
186: #   Keywords:
187: #    XVELOCITY             [  initial velocity in the x-direction (m/s)
188: #    YVELOCITY             [  initial velocity in the y-direction (m/s)
189: #    DEPTH                 [  initial water depth (m)
190: #    LEVEL                 [  initial water level (m)
191: #    CHEZY                 [  bed resistance using Chezy value
192: #      n+2 + 2*p) The value is put on the following line
193: #      n+3 + 2*P) DONE indicates no more parameters are to be listed
194:
195:
196: SOLID Left Dam Wall
197: 4
198: CLOSED
199: 7.7 0.0
200: 7.7 1.3
201: 6.9 1.3
202: 6.9 0.0
203:
204: SOLID Right dam wall
205: 4
206: CLOSED
207: 6.9 3.6
208: 6.9 2.3
209: 7.7 2.3
210: 7.7 3.6
211:
```

```
SOLID Isolated Obstacle
4
CLOSED
11.14 1.75
11.50 1.57
11.85 2.29
11.49 2.47


ENDSOLIDBODIES

************************************************************************************
********

BOUNDARY

# for each boundary condition
# 1) indicate which side of the domain the condition is specified on:
#       NORTH
#    or SOUTH
#    or EAST
#    or WEST
#
# 2) give the extent (nearest and furthest distances along that side (m)
#
# 3) indicate the type
#
# keyword list
# SOLID             [  no parameter   -{default}-
# TRANSMISIVE       [  no parameter
#                     -{the solid boundary condition is changed to transmissive}-
# DISCHARGE         [  inflow per unit lenght of the boundary in cumecs/m (m^2 /s)
# DEPTH or HEIGHT   [  height above bed (m)
# LEVEL             [  height above datum (m)
#
# 4+) enter the parameters using one of the following formats
#
#  a) for a constant parameter include an '=' sign with the keyword and put the
    value on the next line
#
#  b) for a time variable parameter, put the length of the record on the next line.
#     then follow with text data (time in the first column)
#    {The first time given must be 0. AMAZON linearly interpolates between the
    times,
#     and keeps the final value constant}
#
#  c) for a periodic boundary condition, include the '~' symbol with the type
    keyword.
#     The period is put on the following line, with the length of record following
    on a seperate line

EAST
0.0 3.6
TRANSMISSIVE   The far end of the channel. All other boundaries are solid by
    default.

ENDBOUNDARY

************************************************************************************
****
```

A.0.5 Urban Flash Flood

```
Urban flash flood [main template] {Andrew Morris 13:48 15/10/2008}

*******************************************************************************
(The first line is the title of this run (up to 80 characters)

Mandatory parameters come first between      SYSTEM        and  ENDSYSTEM

Optional parameters follow between          SIMULATION    and  ENDSIMULATION

Boundary conditions follow between          BOUNDARY      and  ENDBOUNDARY

Keywords commands are read line by line ignoring leading whitespaces.

*******************************************************************************

SYSTEM
100000     [  maximum number of time steps
60.0       [  maximum run time (s)
6.75       [  width of domain  (m) (in the x-direction)
3.35       [  length of domain (m) (in the y-direction)
540        [  number of cells in the x direction
268        [  number of cells in the y direction
0.45       [  courant number CFL limiting the time step where (vel*dt < CFL*dx)
0.001      [ Minimum calculated depth of flow
0.01       [ Minimum depth d used as a factor in velocity calculations (v=hv/d)

# keyword list
# STEADY       [ Find steady state solution
#  parameter:    threshold of (the greatest shange in depth in a single time step)
#
# MINMOD       [ Use min-mod slope limiter
# SUPERBEE     [ Use Superbee slope limiter
# VANLEER      [ Use the Van Leer slope limiter    -{default}-
# VANALBADA    [ Use the Van Albada slope limiter
#
# VELGRAD      [ use gradient for velocity instead of momentum
# NOGRADIENT   [ do not calculate gradients (i.e. 1st order accuracy in space)
#
# SIMPLIFIED   [ level/storage relationship is used (work by A.Morris following B.
    Sanders)
# PD01         [ Partially dry cells are considered still
# PD02         [ Partially dry cells match the neighbour's velocity at each wet face
#
# PARAVIEW     [ output data as a .vtk file
#  parameters: 1) path\name of file (without the extension ".vtk")
#              *2a) TIME -{optional}- put out timed sequence of files
#              *2b) the period between records
#
# SOLID BODY   [ define regions with polygons. These may be solid regions or
#              [ areas where a parameter is given the same value
#  parameters: 1) number of polygons (for array allocation)
#              2) maximum number of intersections
#              3) number of vertices (for array allocation)
#              4) max error in finding cutting points (relative to cell size)

SOLID
18
1200
5
0.001

GAUGES
0.1
10
0.331 2.655
1.111 2.317
3.797 0.959
3.870 1.479
4.192 1.257
4.514 1.035
4.663 0.837
4.712 1.184
4.861 0.986
5.183 0.764

```

```
 75: PARAVIEW
 76: UrbFlash
 77: TIMESTEP
 78: 1.0
 79:
 80: VELGRAD
 81:
 82: SIMPLIFIED
 83:
 84: PDO2
 85:
 86: MANNING
 87:
 88: ENDSYSTEM
 89:
 90: ****************************************************
 91:
 92: SIMULATION
 93:
 94: # Default values are zero for these parameters.
 95: # (both depth and level can be consistently defined on the same domain)
 96: #
 97: # keyword list
 98: # TOPOGRAPHY or BATHYMETRY  [  bed elevation (array dimensions nX+1 by nY+1)
 99: # XVELOCITY                 [  initial velocity in the x-direction (m/s)
100: # YVELOCITY                 [  initial velocity in the y-direction (m/s)
101: # LEVEL                     [  initial water surface level above a datum (m)
102: # DEPTH                     [  initial water depth (m)
103: # CHEZY                     [  bed resistance using Chezy value
104:
105: # data entry methods
106: #
107: # include an '=' sign with the keyword and put the value on the next line
108: #
109: # include a '+' sign with the keyword to enter data in a rectangular sub-area
110: #  the following parameters go *before* any other data or keywords
111: #  Parameters: 1) two i-indices, the first and last cells
112: #              2) two j-indices, the first and last cells
113: #
114: # use HERE and follow with text data
115: # e.g.
116: # LEVEL
117: # HERE
118: # 0.1 0.2 0.3 ...
119: # 0.3 0.4 0.5 ...
120: # ... and so on ...
121: #
122: # use FILE and follow with the name and path of a file containing binary data
123: # e.g.
124: # LEVEL
125: # FILE
126: # c:\AMAZON\dambreak\wetbed_dam_40.dat
127: #
128: # use RASTER to read data from a raster text file
129: # keywords:
130: #           FILE  mandatory penultimate line, used as above
131: #           ADJUST subtract a constant (on following line) from the values read
132: #           TIMES multiply the values by a constant (after applying adjust)
133: #           FROM identify an origin, relative to the coordinates used by the
134: #                raster file these coordinates are given on the next line
135: #           SCALE follows with the ratio of the solver and raster cell sizes
136: #           NODATAValue indicates the NullDataValue header line is used
137:
138: ROUGHNESS=
139: 0.0162
140:
141: DEPTH=
142: 0.00
143:
144: BATHYMETRY
145: ASCII
146: ShortTopMod3.DEM
147:
148: ENDSIMULATION
149:
```

```
150: ********************************************************************************
151:
152: SOLIDBODIES
153:
154: # keywords
155: # SOLID indicates a solid immobile body
156: #  Parameters: 1) number of vertices on body (n)
157: #              2) OPEN   :: if the first and last vertices do not join
158: #              or CLOSED :: if the last vertex is joined to the first
159: #       3 to 2+n) x, y   :: coodinates on solid body (counterclockwise)
160: #
161: # POLYGON indicates a region over which parameters are specified
162: #  Parameters: 1) number of vertices on polygon (n)
163: #              2) OPEN   :: if the first and last vertices do not join
164: #              or CLOSED :: if the last vertex is joined to the first
165: #       3 to 2+n) x, y   :: coodinates of vertices (counterclockwise)
166: #      n+1 + 2*p) Keywords follow to name a parameter to be set
167: #   Keywords:
168: #    XVELOCITY             [  initial velocity in the x-direction (m/s)
169: #    YVELOCITY             [  initial velocity in the y-direction (m/s)
170: #    DEPTH                 [  initial water depth (m)
171: #    LEVEL                 [  initial water level (m)
172: #    CHEZY                 [  bed resistance using Chezy value
173: #      n+2 + 2*p) The value is put on the following line
174: #      n+3 + 2*P) DONE indicates no more parameters are to be listed
175:
176: SOLID Left Wall
177: 4
178: CLOSED
179: 0.941 2.65
180: 0.941 2.55
181: 5.701 2.022
182: 5.701 2.122
183:
184: SOLID Right wall
185: 4
186: CLOSED
187: 5.445 0.06
188: 5.445 0.128
189: 0.208 0.855
190: 0.208 0.755
191:
192: SOLID Building
193: 4
194: CLOSED
195: 4.0100    0.6770
196: 4.0300    0.8250
197: 3.8820    0.8460
198: 3.8610    0.6980
199:
200: SOLID Building
201: 4
202: CLOSED
203: 4.0580    1.0230
204: 4.0790    1.1720
205: 3.9310    1.1930
206: 3.9100    1.0440
207:
208: #--------------------------------
209: # 14 blocks omited from sample
210: #--------------------------------
211:
212: ENDSOLIDBODIES
213:
214: ********************************************************************
215:
216:
217:
218:
219:
220:
221:
222:
223:
224:
```

```
225: BOUNDARY
226:
227: # for each boundary condition
228: # 1) indicate which side of the domain the condition is specified on:
229: #       NORTH
230: #    or SOUTH
231: #    or EAST
232: #    or WEST
233: #
234: # 2) give the extent (nearest and furthest distances along that side (m)
235: #
236: # 3) indicate the type
237: #
238: # keyword list
239: # SOLID             [  no parameter   -{default}-
240: # TRANSMISIVE       [  no parameter
241: #                     -{the solid boundary condition is changed to transmissive}-
242: # DISCHARGE         [  inflow per unit lenght of the boundary in cumecs/m (m^2/s)
243: # DEPTH or HEIGHT   [  height above bed (m)
244: # LEVEL             [  height above datum (m)
245: #
246: # 4+) enter the parameters using one of the following formats
247: #
248: #  a) for a constant parameter include an '=' sign with the keyword and
249: #                                 put the value on the next line
250: #  b) for a time variable parameter, put the record length on the next line.
251: #     then follow with text data (time in the first column)
252: #    {The first time given must be 0. AMAZON linearly interpolates between
253: #     the times, and keeps the final value constant}
254: #
255: #  c) for a periodic boundary condition, include the '~' symbol with the keyword.
256: #     The period is put on the following line, then record length on the next.
257:
258: WEST
259: 1.3 2.3
260: DISCHARGE
261: 301
262: 0.0 0.00025
263: #-------------------
264: # 299 lines omited
265: #-------------------
266: 60.2    0.01038
267:
268: EAST
269: 0.0 3.35
270: TRANSMISSIVE
271:
272: ENDBOUNDARY
273:
274: ****************************************************
```

Appendix B

Conference Paper

7th International Conference on Hydroinformatics
HIC 2006, Nice, FRANCE

TWO DIMENSIONAL FLOOD SIMULATION USING THE CARTESIAN CUT-CELL METHOD

A. G. MORRIS,
D.M. INGRAM,
C.G. MINGHAM
Department of Computing and Mathematics, Manchester Metropolitan University, Manchester, M1 5GD, England

Two dimensional dynamic models have been increasingly used for river flood simulation. This commonly uses satellite remote sensor data, recorded on a rectangular (Raster) grid. There are many important features on a flood plain, such as hedges or buildings, which do not follow the grid lines. Irregular meshes can be used to follow these features, but converting Raster data to this format involves a loss of detail. The Cartesian cut-cell (CC) method uses a rectangular mesh. The edges of irregular *solid* bodies are located precisely with sequences of vertex coordinates. Cut-cells, which lie on an edge, are given special treatment. This allows straightforward integration of grid and vector data, potentially within a GIS based framework. This paper introduces the semi-permeable internal (SPIn) boundary cut-cell method. This allows the integration of permeable boundaries, such as hedges, into the model. To explore the impacts of these features, a small scale river flood event, over a field featuring a hedgerow, is simulated.

INTRODUCTION

In mapping flood risk 2-dimensional hydraulic models are coming to be valued increasingly as a tool, to account for spatial variations in out of channel flows. Advances in computer power have made these techniques feasible, but it is the ever increasing store of high quality geographical data which makes them so broadly applicable. Satellite remote sensors provide detailed data on the surface elevation, land use and water coverage (Cobby *et al* [4], Townsend & Walsh [10]). The method of data collection yields a regular orthogonal raster grid of point values. The level of detail provided is particularly valuable for floodplains where small changes in elevation can easily be missed by standard techniques.

Information on land use and other features is also valuable, but using this data effectively can be problematic. Extensive empirical studies have been conducted into the relation between vegetation and effective bed roughness (Werner [11]). However, the effective roughness can vary considerably within a site, seasonally, and even during a single flood event. The heterogeneity of land use has been of particular interest to those modelling floodplain flows in two dimensions (Cobby [5], Romanovicz [9]).

Calibration of roughness parameters has historically relied on relatively few measurements of flood events, such as river level gauges which can be unreliable at high flows (Pappenberger *et al* [8]), and post event observations of flood damage or debris.

This has led to simplifying the classification of land use (Aronica *et al* [1] Grayson *et al* [6]). Satellite images showing water surfaces during flood events, have so had limited value in enabling a more spatially diverse model of land features (Bates *et al* [2], Werner *et al* [11]). Where sensitivity to distributed sets of roughness parameters has been shown, floodplain flow has formed a significant component in overall conveyance. It is expected that flow routing has a major influence on such events, and that linear land features, as well as topography, can have a profound impact on this.

Two dimensional hydraulic models often use an irregular mesh. These have been adapted to better represent particular manmade features, such as hedgerows or roads, and to pick out important aspects of topography. (Cobby *et al* [5]) In representing raster data, individual grid points may be selected. This involves discarding valuable data on the discarded grid points, and may still fail to accurately place features which do not lie neatly on the grid. Alternatively, levels may be interpolated at any point, which necessarily involves loss of definition through smoothing.

Orthogonal meshes are simpler to implement and allow the use of certain numerical techniques not possible otherwise. It also allows the mesh to be fitted to the raster grid, allowing direct use of this data. However, accuracy in the placement of features is almost always compromised.

Cartesian cut-cell methods (Causon *et al* [3]) define irregular solid bodies on a rectangular mesh. Special treatment is given to the cut-cells on the edge of a solid body. This paper presents an extension of the cut-cell method to encompass permeable (Pin), and semi-permeable (SPIn) internal boundaries. This would allow accurate placement of a range of features regardless of where they lie relative to the grid. It is also a methodology which can be readily integrated with established GIS protocols.

A test case demonstrates the use of cut-cells and polygon defined regions, illustrating the impact of hedgerows on floodplain flows. AMAZON-CC (Zhou *et al* [14]), an explicit Godunov type, finite-volume, approximate Riemann solver, which is 2^{nd} order accurate in time and space is used.

THE CARTESIAN CUT-CELL METHOD DEVELOPMENT AND CONTEXT

The Cartesian cut-cell (CC) method was developed for use with finite volume methods. It accurately describes the boundary of a solid body within a regular Cartesian grid as an irregular polygon with a sequence of vertices within the domain (Figure 1.). Those *cut* cells which are crossed by the boundary, are classified according to their shape and the orientation of solid wall. To preserve the time step without compromising stability, smaller cells are merged with larger neighbouring cells.

Finite volume methods find the flux across the interface between two cells based on an estimation of the variables on either side. Excepting where discontinuities occur, for normal cells in the CC mesh it is possible to accurately reconstruct local gradients, based on neighbouring cell values, to achieve a second order accurate estimate of these fluxes.

The Surface Gradient Method (Zhou *et al* [12]) is applied to ensure the bed slope balances the flux gradient. A slope limiting function (for example van Leer [7]) ensures that where a discontinuity does occur, this does not lead to unwanted non-physical solutions. While only first order accuracy in space can be achieved for cut cells, the number of such cells is not proportionate to the grid resolution. Thus, while there is some compromise in accuracy, the sum of errors from these cells will be roughly proportionate with that from the remainder of the domain.

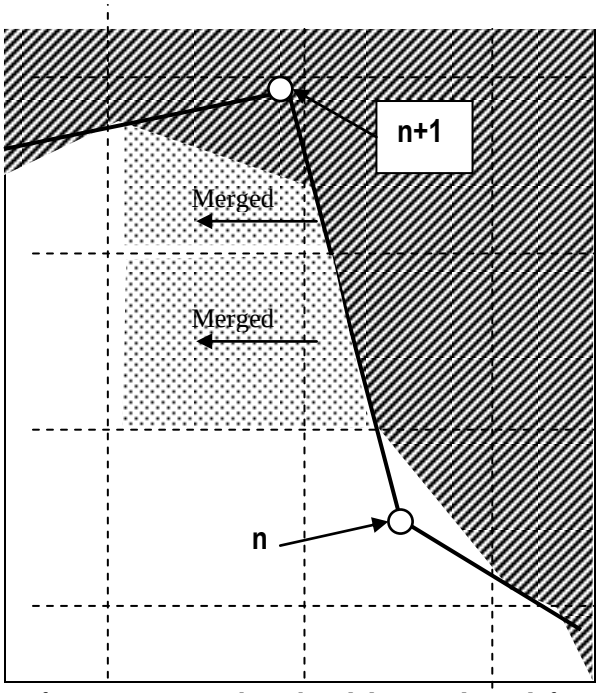

Figure 1. Section of a Cartesian mesh with solid areas derived from the intersection points between polygon edges and grid lines. Solid cells and solid areas of cut-cells are shaded. Vertices are listed anti-clockwise around the body. Smaller cells are merged with their neighbour across the longest edge.

It is a natural extension to these techniques, to have regions defined in the same way as solid bodies, with a permeable internal boundary. The method for calculating the flux across a solid boundary uses ghost point values, so using actual values on either side of a PIn boundary is feasible. Also, the numerical methods used here have been applied successfully on irregular meshes, although without the same spatial accuracy. Since the CC mesh can be considered a special case of the irregular mesh, similar success can be expected.

Zhou *et al* [13] applied AMAZON to flow over a step change in bed level. The effect is treated as a local head loss, comparable with the effect of a sudden constriction in channel width. This head loss h_ξ can be found from downstream velocity u, and an empirical parameter ξ Eq. (1).

$$h_\xi = \xi \frac{u^2}{2g} \tag{1}$$

This is implemented as effective pressure acting on the lower side of the step. Eq. (2)

$$\begin{aligned} \tau(\xi) &= \rho g h_\xi \\ &= \rho \xi u^2 \end{aligned} \tag{2}$$

This method ensures that still water has a level surface. It has been successfully applied to channel and dam break test cases. (Zhou *et al* [13]). This approach should be readily applicable to other changes in hydraulic head across a border. Thus *semi*-permeable internal (SPIn) boundaries may be included in the flow domain.

AN EXPLORATION OF THE EFFECTS OF SEMI PERMEABLE BOUNDARIES ON FLOODPLAIN FLOW

It is too early in the development of the methods described above, for validation. Instead, a simple case of overbank flows on a small scale is used to show that the finite volume methods used can give realistic results. It also explores the impact that the flow resistance and placement of hedges can have on floodplain flows.

The domain (Figure 2.) consists of a rectangular channel 10m long by 1m wide, with a 1:100 slope descending from West to East in the direction of flow. The south side has a solid wall, with a solid trapezoid obstacle projecting 0.3m into the stream halfway along. The North side has a slope leading up to a floodplain, which is separated into Eastern and Western regions by a hedge.

The Chezy roughness parameter for the channel is 100, West of the hedge is 40, East of the Hedge is 20, and the hedge has a value of 2. Strict inflow and outflow conditions (Table1.) are enforced to ensure the same overall mass balance.

Table 1. Default discharge at entry to and exit from the channel. Discharge changes linearly between stages.

Time (inflow)	Time (outflow)	Discharge (cumecs)
0 -120 seconds	0-480 seconds	0.03
120 – 420 seconds	480 – 780 seconds	increasing
420 – 900 seconds	780 – 1260 seconds	0.04
900 – 1200 seconds	1260 – 1560 seconds	decreasing
1200+ seconds	1560+ seconds	0.03

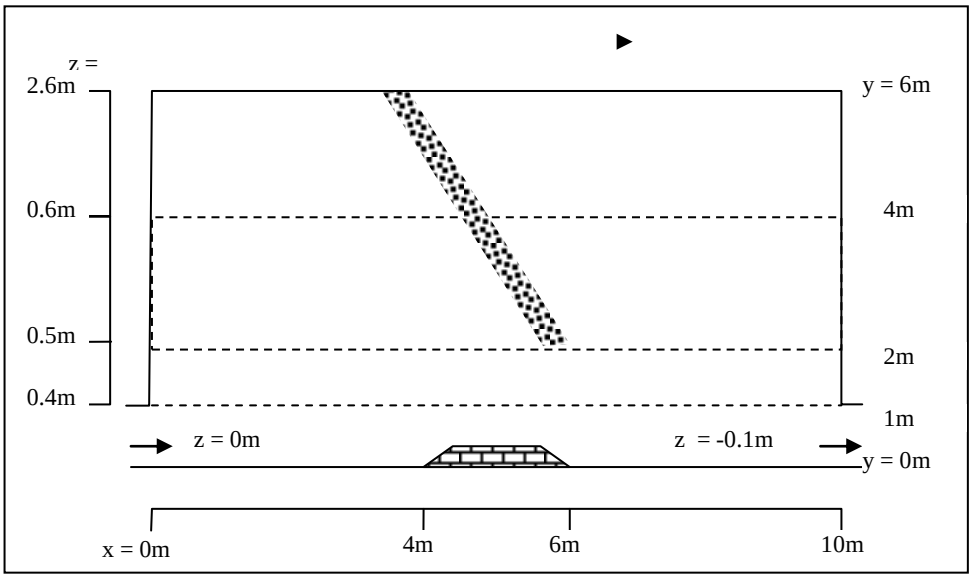

Figure 2. A map of the test case. Flow travels from bottom left to bottom right. Solid lines are impermeable. Dashed lines indicate a change in bed level or gradient. The hedge is shown as a mottled region its default position.

Sensitivity analysis was carried out for roughness parameters and the location of the hedge. The roughness parameters were changed by 20%. The ends of the hedge were moved 2 metres either East or West. This should be taken into account when evaluating this impact. The volume of water out of the channel is used for comparison. Root mean square (RMS) difference between time series and the difference between maximum volumes of the control and test cases are given below (Table 2). The maximum volume of inundation was 1.186 cubic meters after approximately 11 minutes from the start of the simulation. This varied by less than 0.4% in all the tests. The RMS difference was more significant, the interaction between floodplain and channel being greater during inundation than recession. Figures 3 and 4 show the peak flood flows.

The hedge appears to influence flows in two distinct ways. Locally it retards the flow, but it can also help to channel these flows. This flow routing effect is particularly

strong when the lower end of the hedge is close to the bay window, as these both serve to constrict the flow. The degree to which this flow is diverted away from the channel does not only depend on the location of the hedge. Both increasing and decreasing the Chezy value of the hedge increased maximum inundation. This may indicate that this value influences both the retarding, and the routing effects. The degree to which flow was constrained by the solid barrier, and constricted discharge at the Eastern end of the domain, probably also contribute to these phenomena.

Table 2. test cases. The first two columns show the parameter altered and its new value. The last two columns give measures of difference between the test results and the results from the default case.

region	**Chezy value for roughness**	**RMS difference in floodplain storage (cc)**	**Difference in maximum floodplain storage (cc)**
Channel	120	0.37	-0.32
	80	0.41	-0.48
West end	50	1.11	-0.68
	30	1.71	-0.08
East end	25	1.17	0.24
	15	1.50	-0.08
Hedge	2.5	3.83	1.92
	1.5	2.84	2.56
South end of hedge	**North end of hedge**		
7.6 - 8 m	3.6 - 4 m	14.54	0.12
3.6 – 4 m	3.6 – 4 m	2.81	-4.20
5.6 - 6 m	5.6 – 6 m	3.80	3.63
5.6 – 6 m	1.6 – 2 m	1.64	1.00
7.6 – 8 m	5.6 – 6 m	3.29	-2.32
3.6 – 4 m	1.6 – 2 m	2.62	-3.92

CONCLUSIONS

The methods used give a reasonably convincing simulation of flood flows, though without comparison with a real event, no definite evaluation can be made. The strong influence of the hedgerows on the direction of flow indicates that the accurate placement of such features may well be significant. Since a major motivation behind the use of 2-dimensional simulations is to deal with the spatially diverse flow fields that have been observed on floodplains, accuracy in placing features which influence these must be important. PIn and SPIn boundaries are potentially a useful tool for achieving this.

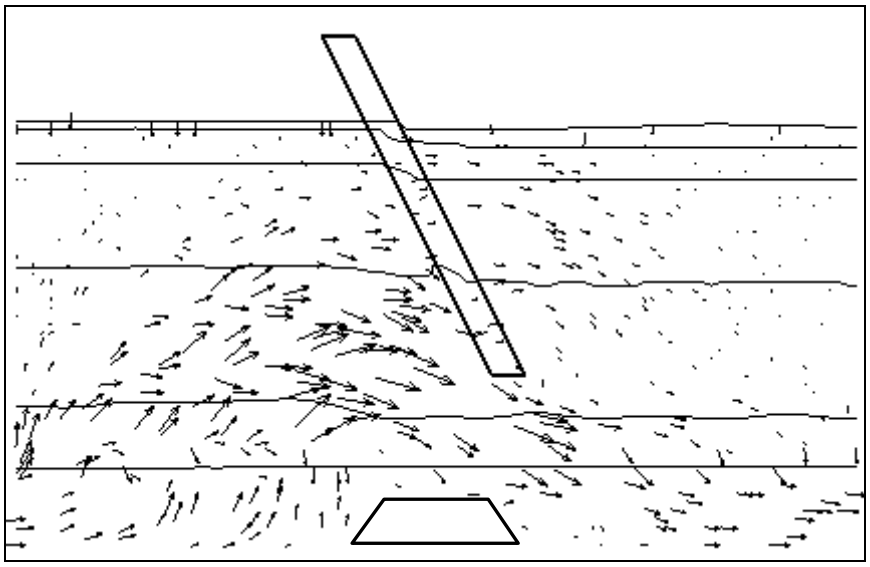

Figure3 Default case at maximum inundation. Flow field with arrow length proportional to velocity. The hedge and channel obstacle are shown in outline. Contours indicate depths of 0m, 0.01m, 0.02m, 0.05m, 0.1m, 0.2m.

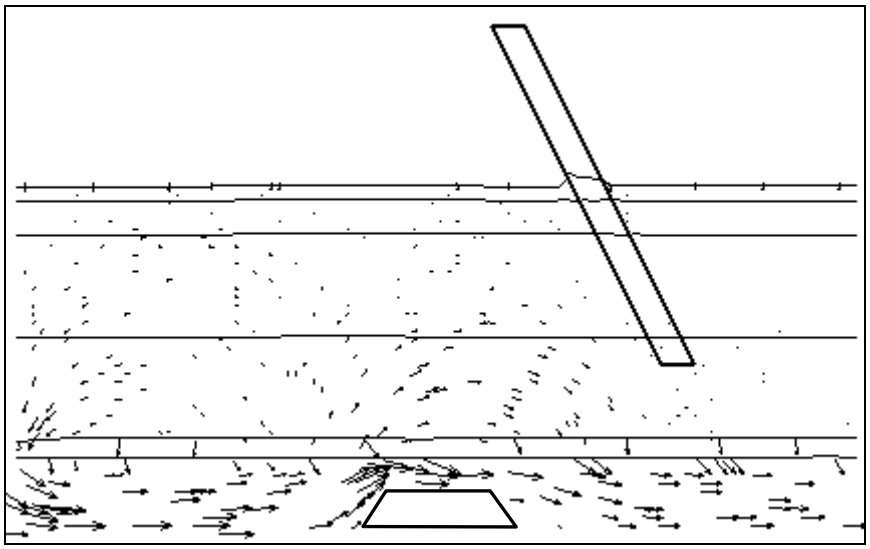

Figure4. Test case with hedge moved 2 meters East, at maximum inundation. Flow field with arrow length proportional to velocity. The hedge and channel obstacle are shown in outline. Contours indicate depths of 0m, 0.01m, 0.02m, 0.05m, 0.1m and 0.2m.

ACKNOWLEDGEMENT

The authors would like to thank F. Pappenberger for his timely advice and help.

Bibliography

[1] Aronica G., Hankin B. and Beven K., "Uncertainty and equifinality in calibrating distributed roughness coefficients in a flood propogation model with limited data", *Advances in Water Resources*, Vol. 22, No. 4, (1998), pp 249-365

[2] Bates P.D., Horritt M.S., Aronica G. and Beven K., "Bayesian updating of flood inundation likelihoods conditioned on flood extent data", *Hydrol. Process.* Vol. 18, No. 17, (2005) pp921-936.

[3] Causon, D. M., Ingram D.M. and Mingham C.G., "A Cartesian cut cell method for shallow water flows with moving boundaries.", *Advances in Water Resources*, Vol. 24, No. 8, (2001) pp 899-911.

[4] Cobby D.M., Mason D.C. and Davenport I.J., "Image processing of airborne scanning laser altimetry for improved river flood modelling", *ISPRS Journal of Photogrammetry & Remote Sensing* Vol. 56, (2001), pp 121-138.

[5] Cobby D. M., Mason D.C., Horritt, M.S. and Bates, P.D., "Two-dimensional hydraulic flood modelling using a finite-element mesh decomposed according to vegetation and topographic features derived from airborne scanning laser altimetry." *Hydrological Processes* Vol. 17, No. 10, (2003), pp 1979-2000.

[6] Grayson R.B., Blöschl G., Western A.W., McMahon T.A., "Advances in the use of observed spatial patterns of catchment hydrological response", *Advances in Water Resources*, Vol. 25, (2002), pp 1313-1334.

[7] van Leer B. "Towards the ultimate conservative difference scheme V: A second order sequel to Godunov's method" *J. Comput. Phys.* Vol. 32, (1979) pp101-136.

[8] Pappenberger F., Matgen P., Beven K.J., Henry J.-B., Pfister L. and deFraipont P.,"The influence of rating curve uncertainty on flood inundation predictions", Flood Risk Assessment, University of Bath, U.K. , (2004), pp107-116.

[9] Romanovicz R. and Beven K., "Estimation of flood inundation probabilities as conditioned on event inundation maps.",*Water Resources Research*, Vol. 39, No. 3, (2003), pp1073

[10] Townsend P.A., and Walsh S.J., "Modelling floodplain inundation using an integrated GIS with radar and optical remote sensing", *Geomorphology*, Vol. 21, (1998), pp 295-312

[11] Werner M.G.F., Hunter N.M. and Bates P.D., "Identifiability of distributed floodplain roughness values in flood extent estimation", *Journal of Hydrology*, Vol. 314, (2005), pp 139-157.

[12] Zhou J.G., D. M. Causon, C. G. Mingham, and D. M. Ingram "The surface gradient method for the treatment of source terms in the shallow-water equations", *Journal of Computational Physics* Vol. 168**,** (2001), pp 1-25.

[13] Zhou J.G., et at, "Numerical solutions of the shallow water equations with discontinuous bed topography", *Int. J. Numer. Meth. Fluids* Vol. 38, (2002), pp 769-788.

[14] Zhou J.G., Causon D.M., Ingram D.M. and Mingham C.G., "Numerical Prediction of Dam-Break Flows in General Geometries with Complex Bed Topography", *Journal of Hydraulic Engineering - ASCE* Vol. 130, No. 4 (2004) pp 332-340.

Bibliography

Alcrudo, F. (2003). Mathematical modelling techniques for flood propogation in urban areas. In *EC Contract EVG1-CT-2001-00037 IMPACT Investigation of Extreme Flood Processes and Uncertainty, Proceedings 3rd Project Workshop*.

Armesto-Álvarez, J. A. (2008). *Towards the Numerical Simulation of Ship Generated Waves Using a Cartesian Cut Cell Based Free Surface Solver*. Ph.D. thesis, Manchester Metropolitan University.

Aureli, F., Maranzoni, A., and Mignosa, P. (2003). Parma university simulations of the isolated building test case. In *EC Contract EVG1-CT-2001-00037 IMPACT Investigation of Extreme Flood Processes and Uncertainty, Proceedings 3rd Project Workshop*.

Bates, P. D. (2000). Development and testing of a subgrid-scale model for moving-boundary hydrodynamic problems in shallow water. *Hydrological Processes*, **14**(11-12), 2073–2088.

Bates, P. D. (2012). Integrating remote sensing data with flood inundation models: how far have we got? *Hydrological Processes*, **26**(16), 2515–2521.

Bates, P. D., Horritt, M., Smith, C., and Mason, D. C. (1997). Integrating remote sensing observations of flood hydrology and hydraulic modelling. *Hydrological Processes*, **11**, 1777–1795.

Beffa, C. and Connell, R. (2001). Two-dimensional flood plain flow. i: Model description. *Journal of Hydraulic Engineering*, **6**(5), 397–405.

Begnudelli, L. and Sanders, B. (2006). Unstructured grid finite volume algorithm for shallow-water flow and transport with wetting and drying. *ASCE Journal of Hydraulic Engineering*, **132**(4), 371–384.

Begnudelli, L. and Sanders, B. (2007). Conservative wetting and drying methodology for quadrilateral grid finite volume models. *ASCE Journal of Hydraulic Engineering*, **133**(3), 312–322.

Berger, M., Aftosmis, M., and Murman, S. (2005). Analysis of slope limiters on irregular grid. In *43rd AIAA Aerospace Sciences Meeting and Exhibit*, volume AIAA-2005-490, Reno, NV. AIAA.

Brufau, P., Garcia-Navarro, P., and Vazquez-Cendon, M. E. (2004). Zero mass error using unsteady wetting-drying conditions in shallow flows over dry irregular topography. *International Journal for Numerical Methods in Fluids*, **45**(10), 1047–1082. 842VB INT J NUMER METHOD FLUID.

Capart, H. (2003). Dam-break flow past an oblique building on a square grid: rigid and erodible building simulations. In *EC Contract EVG1-CT-2001-00037 IMPACT Investigation of Extreme Flood Processes and Uncertainty, Proceedings 3rd Project Workshop*.

Causon, D. M., Mingham, C. G., and Ingram, D. R. (1999). Advances in calculation methods for supercritical flow in spillway channels. *Journal Of Hydraulic Engineering-Asce*, **125**(10), 1039–1050.

Cea, L., Puertas, J., and Vazquez-Cendon, M. (2007). Depth averaged modelling of turbulent shallow water flow with wet-dry fronts. *ARCHIVES OF COMPUTATIONAL METHODS IN ENGINEERING*, **14**(3), 303–341.

Cioffi, F. and Gallerano, F. (2003). A two-dimensional self-adaptive hydrodynamic scheme for the assessment of the effects of structures on flooding phenomena in river baisins. *River Research and Applications*, **19**, 1–26.

Cobby, D. M., Mason, D. C., Horritt, M. S., and Bates, P. D. (2003). Two-dimensional hydraulic flood modelling using a finite-element mesh decomposed according to vegetation and topographic features derived from airborne scanning laser altimetry. *Hydrological Processes*, **17**(10), 1979–2000.

Connell, R., Painter, D., and Beffa, C. (2001). Two-dimensional flood plain flow. ii: Model validation. *Journal of Hydraulic Engineering*, **6**(5), 406–415.

Douglas, D. H. and Peucker, T. K. (1973). Algorithms for the reduction of the number of points required to represent a digitized line or its caricature. *The Canadian Cartographer*, **10**(2), 112–122.

Fowler, A. (2000). The low down on lidar. *Earth Observation Magazine*, **7**(227).

Fraccarollo, L. and Toro, E. (1995). Experimental and numerical assessment of the shallow water model for two-dimansional dam-break type problems. *Journal of Hydraulic Research*, **33**(6), 843 – 864.

Guinot, V. and Soares-Frazao, S. (2006). Flux and source term discretization in two-dimensional shallow water models with porosity on unstructured grids. *International Journal for Numerical Methods in Fluids*, **50**, 309–345.

Harten, A., Lax, P., and van Leer B. (1983). On upstream differencing and godunov-type schemes for hyperbolic conservation laws. *SIAM Review*, **25**(1), 35–61.

Hodgeson, M. (2004). Accuracy of airborne lidar-derived elevation: empirical assessment and error budget. *Photogrammetric Engineering and Remote Sensing*, **70**(3), 331–339.

Horritt, M. (2004). Development and testing of a simple 2d finite volume model of sub-critical shallow water flow. *International Journal for Numerical Methods in Fluids*, **44**(11), 1231–1255. 810WJ INT J NUMER METHOD FLUID.

Horritt, M. S. and Bates, P. D. (2002). Evaluation of 1d and 2d numerical models for predicting river flood inundation. *Journal of Hydrology*, **268**(1-4), 87–99.

Hunter, N., Bates, P., Neelz, S., Pender, G., Villanueva, I., Wright, N., Liang, D., Falconer, R., Lin, B., Waller, S., Crossley, A., and Mason, D. (2008). Benchmarking 2d hydraulic models for urban flooding. *Proceedings of the Institute of Civil Engineers-Water Management*, **161**(1), 13–30.

Ingram, D. M., Causon, D. M., and Mingham, C. G. (2003). Developments in cartesian cut cell methods. *Mathematics and Computers in Simulation*, **61**(3-6), 561–572.

Jain, M., Kothyari, U. C., and Ranga Raju, K. G. (2004). A GIS based distributed rainfall-runoff model. *Journal of Hydrology*, **299**(1-2), 107.

Knight, D. W. and Shiono, K. (1996). River channel and floodplain hydraulics. In D. E. W. Malcolm G Anderson and P. D. Bates, editors, *Floodplain Processes*, pages 139–182. John Wiley & Sons Ltd.

Kouwen, N. (1988). Field estimation of the biomechanical properties of grass. *Journal of Hydraulic Research*, **26**(5), 559–568.

Kundzewicz, Z. W. and Dobrzynski, D. (2000). Book reviews: Flood estimation handbook (procedures for flood frequency estimation). *Hydrological Sciences Journal*, **45**(6), 929–930.

Lane, S. and Richards, K. (2001). High resolution, two-dimensional spatial modelling of flow processes in a multi-thread channel. In B. PD and S. N. Lane, editors, *High Resolution Flow Modelling in Hydrology and Geomorphology*, pages 105–124. John Wiley & sons Ltd.

Leandro, J., Chen, A., Djordjevîc, S., and Dragan, A. (2009). Comparison of 1D/1D and 1D/2D coupled (sewer//surface) hydraulic models of urban flood simulation. *Journal of Hydraulic Engineering*, **135**(6), 495–504.

l'Homme, J., Soares-Frazao, S., Guinot, V., and Zech, Y. (2006). Large-scale urban flood modellling and two-dimensional shallow water models with porosity. In *7th International Conference on Hydroinformatics*.

Mason, D. C., Cobby, D. M., Horrit, M. S., and Bates, P. B. (2003). Floodplain friction parameterization in two-dimensional river flood models using vegetation heights derived from airborne scanning laser altimetry. *Hydrological Processes*, **17**, 1711–1732.

May, S. and Berger, M. (2013). Two-dimensional slope limiters for finite volume schemes on non-coordinate-aligned meshes. *SIAM Journal for Scientific Computing*, **35**(5), A2163–A2187.

Mignot, E. and Paquier, A. (2003a). Impact flood propagation: The isolated building test case: Cemagref's modelling. In *EC Contract EVG1-CT-2001-00037 IMPACT Investigation of Extreme Flood Processes and Uncertainty, Proceedings 3rd Project Workshop*.

Mignot, E. and Paquier, A. (2003b). Impact flood propagation: The model city flooding experiment: Cemagref's modelling. In *EC Contract EVG1-CT-2001-00037 IMPACT Investigation of Extreme Flood Processes and Uncertainty, Proceedings 3rd Project Workshop*.

Mingham, C. and Causon, D. (1998). High-resolution finite-volume method for shallow water flows. *Journal of Hydraulic Engineering*, **124**(6), 605–614.

Morris, A. (2002). *Modelling Urban Inundation on the River Sow*. Master's thesis, Lancaster University.

Morris, A., Ingram, D., and C.G., M. (2006). Two dimensional flood simulation using the cartesian cut-cell method. In *7th International Conference on Hydroinformatics*.

Mortimer, K. and Mayers, D. (1994). *Numerical Solution of Partial Differential Equations*. Cambridge University Press, 1 edition.

Musleh, F. A. and Cruise, J. (2006). Functional relationships of resistance in wide flood plains with rigid unsubmerged vegetation. *Journal of Hydraulic Engineering*, **132**(2), 163–171.

Neelz, S. and Pender, G. (2009). Desktop review of 2d hydraulic modelling packages. Technical Report SC080035, Environment Agency.

Neelz, S. and Pender, G. (2013). Benchmarking the latest generation of 2d hydraulic modelling packages. Technical Report SC120002, Environment Agency.

Noel, B., Soares Frazao, S., and Zech, Y. (2003). Impact wp3 : Flood propagation - computation on the isolated building test case and the model city flooding experiment. In *EC Contract EVG1-CT-2001-00037 IMPACT Investigation of Extreme Flood Processes and Uncertainty, Proceedings 3rd Project Workshop*.

Paquier, A., Farissier, P., Ramez, P., Haider, S., and Maurel, P. (2001). Simulating floods in complex situations using 2-d model. In *Forecasting and Mitigation of Water-Related Disasters, Theme C, Proceedings - 21st Century: The New Era for Hydraulic Research and Its Applications*, pages 130–135. Tsinghua University Press. BU24C.

Pennington, E. C. and Tunstall, S. M. (1996). Risks and resources: Defining and managing the floodplain. In M. G. Anderson, D. E. Walling, and P. D. Bates, editors, *Floodplain Processes*, pages 493–533. John Wiley & Sons Ltd.

Petaccia, G. and Savi, F. (2003). Two dimensionnal simulation of a dam-break wave propagation for the isolated building test case. In *EC Contract EVG1-CT-2001-00037 IMPACT Investigation of Extreme Flood Processes and Uncertainty, Proceedings 3rd Project Workshop*.

Pitt, M. (2008). The Pitt Review: lessons learned from the 2007 flood. Technical report, The Cabinet Office.

Quecedo, M. and Pastor, M. (2002). A reappraisal of taylor-galerkin algorithm for drying-wetting areas in shallow water computations. *International Journal for Numerical Methods in Fluids*, **38**(6), 515–531.

Roache, P. (1997). Quantification of uncertainty in computational fluid dynamics. *Annual Review of Fluid Mechanics*, **29**, 123–160.

Roe, P. (1986). Characteristic-based schemes for the euler equations. *Annual Review of Fluid Mechanics*, **18**, 337–365.

Sanders, B. F., Schubert, J. E., and Gallegos, H. A. (2008). Integral formulation of shallow-water equations with anisotropic porosity for urban flood modeling. *JOURNAL OF HYDROLOGY*, **362**(1-2), 19–38.

Sauvaget, P., David, E., Demmerle, D., and Lefort, P. (2000). Optimum design of a flood relief culvert under the a89 motorway on the dordogne-isle confluence plain. *Hydrological Processes*, **14**, 2311–2329.

Schubert, J., Sanders, B., Smith, M., and Wright, N. (2008). Unstructured mesh generation and landcover-based resistance for hydrodynamic modeling of urban flooding. *Advances in Water Resources*, **31**, 1603–1621.

Sellin, R. H. J., Bryant, T. B., and Loveless, J. H. (2003). An improved method for roughening floodplains on physical river models. *Journal of Hydraulic Research*, **41**(1), 3–14. 650DH J HYDRAUL RES.

Soares-Frazao, S. and Zech, Y. (2007). Experimental study of dam-break flow against an isolated obstacle. *Journal of Hydraulic Research*, **45**(Extra Issue), 27–36.

Sweby, P. (1984). High resolution schemes using flux limiters for hyperbolic conservation laws. *SIAM Journal on Numerical Analysis*, **21**(5), 995–1011.

Tchamen, G. and Kawahita, R. (2001). Modelling wetting and drying effects over complex topography. In B. PD and S. N. Lane, editors, *High Resolution Flow Modelling in Hydrology and Geomorphology*, pages 35–66. John Wiley & sons Ltd.

Toro, E. (1992). Riemann problems and the waf method for solving the two-dimensional shallow water equations. *Phil. Trans. R. Soc. Lond.*, **A338**, 43–68.

Townsend, P. A. and Walsh, S. J. (1998). Modeling floodplain inundation using an integrated gis with radar and optical remote sensing. *Geomorphology*, **21**(3-4), 295–312.

Velickovic, M., van Emelen, S., Zech, Y., and Soares-Frazao, S. (2010). Shallow-water model with porosity: sensetivity analysis to head losses and porosity distribution. In A. Dittrich, K. Koll, J. Aberle, and P. Geisenhainer, editors, *River Flow 2010*, pages 613–620.

Villanueva, I. (2006). Linking riemann and storage cell models. *Water Management: proceedings of the Innstitude of Civil Engineers.*, **159**(1), 27–34.

Werner, M. G. F., Hunter, N. M., and Bates, P. D. (2005). Identifiability of distributed floodplain roughness values in flood extent estimation. *Journal of Hydrology*, **314**(1-4), 139.

Yang, G., Causon, D., Ingram, D., Saunders, R., and Batten, P. (1997). A cartesian cut cell method for compressible flows part a: static body problems. *The Aeronautical Journal*, **101**(994), 47–56.

Yasuda, T., Konishi, H., Mase, H., Mori, N., and Mingham, C. G. (2011). Tsunami propagation by cartesian cut cell method. *Journal of Japan Society of Civil Engineers, Ser. B2 (Coastal Engineering)*, **67**(1), 92–105.

Yu, D. and Lane, S. (2006). Urban fluvial flood modelling using a two dimensional diffusion-wave treatment, part2: development of a sub-grid-scale treatment. *Hydrological Processes*, **20**, 1567–1583.

Zhou, J. G., Causon, D. M., Mingham, C. G., and Ingram, D. M. (2001). The surface gradient method for the treatment of source terms in the shallow-water equations. *Journal of Computational Physics*, **168**(1), 1–25.

Zhou, J. G., Causon, D. M., Ingram, D. M., and Mingham, C. G. (2002). Numerical solutions of the shallow water equations with discontinuous bed topography. *International Journal for Numerical Methods in Fluids*, **38**(8), 769–788. 528QJ INT J NUMER METHOD FLUID.